

PROCESSING AND CHARACTERIZATION OF  
INTERPENETRATING Ni-ZrO<sub>2</sub> COMPOSITES

PROCESSING AND CHARACTERIZATION OF  
INTERPENETRATING Ni-ZrO<sub>2</sub> COMPOSITES

By

DERRICK CHARLES SARAFINCHAN, B.Sc.

A Thesis

Submitted to the School of Graduate Studies

In Partial Fulfilment of the Requirements

for the Degree

Masters of Engineering

McMaster University

(c) Copyright by Derrick Charles Sarafinchan, 1995



## ABSTRACT

This thesis describes the processing and characterization of uniform, interpenetrating, nickel-cubic stabilized zirconia composites. This work was performed in support of future development in the study and modelling of Metal-Ceramic (M/C) Functionally Graded Materials. Since it is of fundamental interest to understand the relationship between microstructure and behaviour in these materials, the characterization has focused on uniform composites.

To minimize experimentation while maximizing productivity, the material grades selected for this study include M:C ratios by volume of 25:75, 50:50, and 75:25, along with the elemental materials (i.e. 100% nickel and 100% cubic zirconia). Solid state powder processing was developed including the steps: colloidal processing (by tape casting), lamination, organic burnout, hydrogen reduction of metal oxides, and hot press consolidation. These techniques support the even distribution of phases and yield high density composites (>98% of theoretical).

Unfortunately the nickel powder used in this study produced atypical properties which complicated the analysis of mechanical behaviour. Composite thermal dilation, elastic, and mechanical properties were determined. Through analysis of residual stresses and fracture behaviour ideas regarding the modelling of M/C composites and FGMs are addressed. Continuum modelling approaches seem appropriate.

## ACKNOWLEDGEMENTS

I would like to express my appreciation to all those who made my time at McMaster educationally stimulating and enjoyable.

Thanks goes to my supervisor, Dr. D.S. Wilkinson, for offering an interesting research project, for providing a relaxed working atmosphere, and for his advice and encouragement. My appreciation goes to Dr. J.D. Embury for informative discussions in which he freely supplied knowledge and advice regarding academic and career related issues.

I send my acknowledgements to the post docs, namely Dr. S. Tuffe, Dr. X. Ning, and Dr. W. Yang, and to members of the McMaster technical staff, namely Jim Garrett, Chris Butcher, and Martin Van Oosten, for their invaluable efforts in support of my research.

A sincere appreciation goes to my fellow colleagues, especially those from the A206 clan, for their friendship and kindness and for their advice and assistance with my work.

A special thanks goes to my family and friends, but most importantly to my parents, for their encouragement and support through all the years of my education.

Most importantly, I thank my wife and soul mate, Lisa, for her love, support and patience. Without her, the completion of this degree would have been a great challenge.

## TABLE OF CONTENTS

Abstract . . . . .	(iii)
Acknowledgements . . . . .	(iv)
Table of Contents . . . . .	(v)
List of Tables . . . . .	(viii)
List of Figures . . . . .	(ix)
<b>CHAPTER 1: INTRODUCTION . . . . .</b>	<b>1</b>
<b>CHAPTER 2: BACKGROUND INFORMATION . . . . .</b>	<b>4</b>
2.1 FGM History . . . . .	4
2.2 M/C FGM Microstructural Distributions . . . . .	6
2.3 Tape Cast Processing . . . . .	11
2.4 Powder Consolidation . . . . .	19
2.4.1 Theory of Sintering . . . . .	19
2.4.2 Theory of Hot Pressing . . . . .	20
2.5 Mechanical Behaviour of Metal/Ceramic Composites . . . . .	21
2.5.1 Mechanical Characteristics of Metals and Ceramics . . . . .	23
2.5.2 Behaviour of Metals and Ceramics within M/C Composites. . . . .	24
2.5.3 Metal/Ceramic Bonding Characteristics . . . . .	27
2.5.4 Behaviour of M/C Composites . . . . .	29
2.5.4.1 Micromechanics vs. Macromechanics . . . . .	30
2.5.4.2 Structure Insensitive Properties in M/C FGMs . . . . .	34
2.5.4.3 Mechanical Interactions in M/C FGMs . . . . .	34
2.6 Summary . . . . .	36

<b>CHAPTER 3: MATERIAL SELECTION AND PROCESSING</b> .....	<b>37</b>
3.1 Model-System Materials Selection for M/C FGM Study .....	37
3.1.1 Material Selection Criteria .....	37
3.1.2 Materials Selected .....	38
3.2 Composite Fabrication .....	44
3.2.1 Tape Casting Development .....	44
3.2.1.1 TZ8Y-Zirconia Slurry Development .....	46
3.2.1.2 ONF Nickel Slurry Development .....	49
3.2.1.3 Tape Casting Procedure .....	51
3.2.1.4 Tape Characteristics .....	55
3.2.1.5 Tape Lamination .....	57
3.2.2 Organic Burnout .....	58
3.2.2.1 Burnout in Argon .....	58
3.2.2.2 Burnout in Air .....	62
3.2.3 Laminate Consolidation .....	69
3.4 Summary .....	71
<b>CHAPTER 4: EXPERIMENTAL PROCEDURE</b> .....	<b>74</b>
4.1 Specimen Heat Treatments .....	74
4.2 Specimen Microstructure Evaluation .....	75
4.2.1 Optical Microscopy .....	75
4.2.2 Scanning Electron Microscopy .....	76
4.2.3 Transmission Electron Microscopy .....	76
4.3 Elastic Property Assessment .....	76
4.4 Thermal Dilatometry .....	77
4.5 Mechanical Testing .....	77
4.5.1 Flexure Test .....	77
4.5.2 Tensile Test .....	81
4.5.3 Hardness Test .....	82
<b>CHAPTER 5: RESULTS</b> .....	<b>83</b>
5.1 Microstructural Observations .....	83

(CHAPTER 5 continued)

5.1.1	General Phase Morphology	83
5.1.2	TEM Characterization of TZ8Y, Ni and Ni/TZ8Y Composites	93
5.1.3	Fractography	99
5.2	Material Properties	103
5.2.1	Elastic Properties	103
5.2.2	Thermal Dilation Response	108
5.2.3	Mechanical Behaviour of Processed Nickel	108
5.2.4	Mechanical Properties of Composites	115
<b>CHAPTER 6:</b>	<b>DISCUSSION</b>	<b>118</b>
6.1	Microstructural Characterization of Composites	118
6.1.1	Powder Dispersion Characteristics	119
6.1.2	Composite Phase Morphology	119
6.1.2.1	Phase Scale and Dispersion	120
6.1.2.2	Phase Connectivity	120
6.1.2.3	Composite Phase Grain Size	121
6.1.2.4	Microstructural Anisotropy	121
6.2	Composite Processing Assessment	123
6.2.1	Evaluation of Material Processing	123
6.2.2	Composite Grade Selection	125
6.3	Evaluation of Elemental Materials for Composite Development	125
6.3.1	Nickel-TZ8Y Interfaces	126
6.3.2	ONF Nickel Evaluation	127
6.3.3	Cubic phase stability in TZ8Y	130
6.3.4	Nickel and TZ8Y as a Model System	131
6.4	Composite Properties and Behaviour	133
6.4.1	Thermal/Elastic Properties	133
6.4.2	Composite Residual Strain/Stress Assessment	134
6.4.3	Composite Mechanical Behaviour	140
<b>CHAPTER 7:</b>	<b>SUMMARY AND CONCLUSIONS</b>	<b>144</b>
<b>REFERENCES</b>		<b>147</b>

## LIST OF TABLES

<b>Table 2.1:</b> FGM synthesis methods and systems (Sasaki and Hirai, 1991). . . . .	7
<b>Table 2.2:</b> Slurry formulation for tape casting of alumina substrates (Williams, 1976). . . . .	13
<b>Table 2.3:</b> Average and typical characteristics of dispersion strengthened alloys and particulate composites. . . . .	32
<b>Table 3.1:</b> Potential M/C "model system" components for FGM characterization. Properties taken from CRC Handbook 1985-1986. . . . .	39
<b>Table 3.2:</b> Powder composition analysis for ONF-nickel and TZ8Y-zirconia. . . . .	43
<b>Table 3.3:</b> Physical/elastic properties of commercial nickel and cubic stabilized zirconia. . . . .	45
<b>Table 3.4:</b> Room temperature mechanical properties of annealed Nickel 200 and cubic stabilized zirconia (TZ8Y). . . . .	45
<b>Table 3.5:</b> Slurry formulations developed for TZ8Y-zirconia and ONF-nickel powders. . . . .	50
<b>Table 3.6:</b> Characteristics of tapes and laminates. . . . .	54
<b>Table 3.7:</b> Carbon, oxygen and sulfur levels in nickel at various stages of processing. . . . .	63
<b>Table 3.8:</b> Oxidation, dilation, and density data of nickel laminates following burnout and reduction. . . . .	67
<b>Table 5.1:</b> Morphology of second phase in 25% Ni and 25% TZ8Y composites. . . . .	91
<b>Table 5.2:</b> Phase intercept length (L) in 50%Ni:50%TZ8Y composite. . . . .	91
<b>Table 5.3:</b> Hot pressed densities measured using the fluid displacement technique. . . . .	92

## LIST OF FIGURES

<b>Figure 2.1:</b> Examples of FGM microstructure profiles (a) continuous Ni/ZrO <sub>2</sub> (Kuroda et al., 1993), (b) discontinuous Ni/Al <sub>2</sub> O <sub>3</sub> (Rabin and Heaps, 1993). . . . .	8
<b>Figure 2.2:</b> Schematic microstructure of two-phase heterogeneous materials (Nan, 1993). (a) randomly dispersed grain structure, (b) uniformly dispersed grain structure, (c) aggregated grain structure, (d) percolation-like cluster structure. . . . .	10
<b>Figure 2.3:</b> Effect of phosphate ester-dispersant on alumina slurry viscosity for two different solvents (Plucknett et al., 1994). . . . .	15
<b>Figure 2.4:</b> (a) Ceramic processing flowsheet (Roosen, 1988), (b) doctor blade apparatus. . . . .	18
<b>Figure 2.5:</b> Atomic flux during sintering under an applied stress. From models of (a) Nabarro-Herring creep, (b) Coble creep. . . . .	22
<b>Figure 3.1:</b> Pressureless sintering dilation for powder compacts of (a) ONF-nickel, (b) TZ0-zirconia. . . . .	41
<b>Figure 3.2:</b> The shear viscosity-dispersant dependence obtained for slurries containing zirconia powder (TZ0), phosphate ester and trichloroethylene. . . . .	48
<b>Figure 3.3:</b> Green tapes from slurries milled for 24 hours and mixed with organics for: (a) 1 hour, (b) 4 hours, and (c) 16 hours. Images from constrained surface. . . . .	53
<b>Figure 3.4:</b> Thermal gravimetric analysis of (a) nickel, (b) TZ8Y tapes treated in flowing argon. Heating rate of 5°C/minute. . . . .	59
<b>Figure 3.5:</b> Laminate burnout treatments in flowing argon gas. . . . .	61
<b>Figure 3.6:</b> Thermal gravimetric analysis of (a) nickel, (b) TZ8Y tapes during treatments in flowing air. . . . .	64

<b>Figure 3.7:</b> Burnout treatment of large geometry, nickel laminates in air. . . .	66
<b>Figure 3.8:</b> Reduction of oxidized nickel laminates via thermal treatment in Ar-5% $H_2$ gas. Heating rate of 10°C/minute. . . . .	68
<b>Figure 3.9:</b> Effect of hot pressing parameters on the consolidated density of TZ8Y laminates. . . . .	72
<b>Figure 4.1:</b> Fully articulated four point 1/4 point flexure test rig. . . . .	79
<b>Figure 4.2:</b> System compliance of the Lloyd's materials testing system. . . . .	80
<b>Figure 5.1:</b> 50%Ni:50%TZ8Y composite green tapes revealing dispersive characteristics, (a) unconstrained surface (top of tape), (b) constrained surface (dried in contact with glass substrate). . . . .	85
<b>Figure 5.2:</b> Optical images of 25%Ni:75%TZ8Y in (a) transverse section (i.e. hot pressing plane, (b) axial section (i.e. perpendicular to hot pressing plane). . . . .	86
<b>Figure 5.3:</b> Optical images of 50%Ni:50%TZ8Y in (a) transverse section (i.e. hot pressing plane, (b) axial section (i.e. perpendicular to hot pressing plane). . . . .	87
<b>Figure 5.4:</b> Optical images of 75%Ni:25%TZ8Y in (a) transverse section (i.e. hot pressing plane, (b) axial section (i.e. perpendicular to hot pressing plane). . . . .	88
<b>Figure 5.5:</b> Schematic of section and direction nomenclature used to characterize composite micrographs. . . . .	89
<b>Figure 5.6:</b> Schematic representation of ferets (i.e. straight line measurements made between tangents at various angles) shown in three feret angles. (From Leco <sup>®</sup> 2001 Reference Manual) . . . . .	90
<b>Figure 5.7:</b> Grain structure developed in TZ8Y (consolidated at 1250°C for 3 hours and thermally etched at 1200°C for 5 minutes). . . . .	94
<b>Figure 5.8:</b> TEM images of 100% TZ8Y. . . . .	95

<b>Figure 5.9:</b> TEM images of 50%Ni:50%TZ8Y composite revealing two phase ceramic. . . . .	96
<b>Figure 5.10:</b> TEM images of composite interfaces, (a) Ni-ZrO <sub>2</sub> , (b) Ni-Y <sub>2</sub> O <sub>3</sub> . . .	97
<b>Figure 5.11:</b> TEM image of ZrO <sub>2</sub> -Y <sub>2</sub> O <sub>3</sub> interface in ceramic phase of 50%Ni:50%TZ8Y composite. . . . .	98
<b>Figure 5.12:</b> Fracture surfaces of ONF-nickel processed at 950°C by (a) pressureless sintering in flowing Ar-5%H <sub>2</sub> , (b) hot pressing in vacuum. . . .	100
<b>Figure 5.13:</b> Fracture surfaces of ONF-nickel after heat treating (950°C for 5 hours in flowing argon) for (a) initially pressureless sintered, (b) initially hot pressed. . . . .	101
<b>Figure 5.14:</b> Fracture surfaces of ONF-nickel after heat treating (1250°C for 1 hours in flowing argon) for (a) initially pressureless sintered, (b) initially hot pressed. . . . .	102
<b>Figure 5.15:</b> Fracture appearances of (a) 100% TZ8Y, fracture origin identified by arrow, (b) 25%Ni:75%TZ8Y composite, tensile surface at top of image. . .	104
<b>Figure 5.16:</b> Fracture images of (a) 100% TZ8Y, including origin of fracture, (b) 25%Ni:75%TZ8Y (brighter phase is nickel). . . . .	105
<b>Figure 5.17:</b> Fracture images of (a) 50%Ni:50%TZ8Y, (b) 75%Ni:25%TZ8Y. Brighter phase is nickel. . . . .	106
<b>Figure 5.18:</b> Elastic Properties of Ni:TZ8Y composites, (a) Young's Modulus, (b) Poisson's ratio. . . . .	107
<b>Figure 5.19:</b> Thermal expansion response for the composites shown via (a) dilation-temperature dependence, (b) coefficient of thermal expansion-temperature dependence. . . . .	109
<b>Figure 5.20:</b> Flexure response of ONF-nickel in (a) as processed condition, (b) heat treated condition. . . . .	110
<b>Figure 5.21:</b> Tensile profile for ONF-nickel hot pressed at 950°C in vacuum. 0.1% offset yield point indicated. . . . .	111

<b>Figure 5.22:</b> (a) yield stress (flexural) versus hardness for ONF-nickel, (b) hardness-grain size dependence for heat treated ONF-nickel. . . . .	113
<b>Figure 5.23:</b> The effects of processing and subsequent heat treatment on the hardness of ONF-nickel. . . . .	114
<b>Figure 5.24:</b> Evaluation of composite macrohardness (using 500g load) and nickel phase microhardness (using 15g load) as a function of composite grade. .	116
<b>Figure 5.25:</b> Flexure test results for Ni:TZ8Y composites, (a) flexure stress-strain profiles, (b) failure strength summary. . . . .	117
<b>Figure 6.1:</b> ZrO <sub>2</sub> -Y <sub>2</sub> O <sub>3</sub> phase diagram (from Roth, Dennis and McMurdie, 1987). . . . .	132
<b>Figure 6.2:</b> Residual stress dependence in Ni:TZ8Y composites calculated via continuum mechanics. . . . .	136
<b>Figure 6.3:</b> Comparison of various models to predict nickel phase flow stress within Ni:TZ8Y composites. . . . .	139
<b>Figure 6.4:</b> Schematic of proposed flow and fracture response of Ni:TZ8Y composites. . . . .	143

## CHAPTER 1

### INTRODUCTION

A Functionally Graded Material (FGM) is composed of different material components such as ceramics and metals having varying mixture ratios and microstructures (Niino and Maeda, 1990). Continuous changes in composite composition and microstructure result in the gradient property profile inherent in FGMs. The FGM concept was originally developed in 1984 in Japan as thermal barrier materials for use in the propulsion system and airframe of spaceplanes (Holt et al., 1993). Other structural applications soon followed such as thermal barrier coatings and ceramic-ceramic and metal-ceramic joints. In addition, FGM technology has broadened into various fields such as electronic, chemical, optical, nuclear, and biological (FGM Forum, 1991).

A project has recently developed in the group (1993) with the objective being to develop an improved fundamental understanding of the structural behaviour of metal-ceramic (M/C) FGMs. M/C FGMs offer an intriguing compromise of properties from tough, thermally conductive behaviour at the metal extreme to high strength, brittle, low conductive behaviour at the ceramic side. Property gradation depends on microstructural characteristics which are influenced by the characteristics of starting materials and

material processing technique. It is of fundamental interest to understand the relationship between microstructure and behaviour in these materials.

The contribution of this thesis is to provide a preliminary investigation of solid state powder processed M/C FGMs via the fabrication and characterization of uniform interpenetrating M/C composites. Specific objectives include the selection of a "model system" for FGM study; development of techniques to fabricate uniform M/C composites; characterization of composite materials, examining both microstructures and properties; and a comprehensive evaluation of composite processing.

Nickel and cubic-stabilized zirconia were selected as the constituents of the model M/C composite system. Along with the elemental materials (i.e. 100% nickel and 100% cubic zirconia) three composite grades were selected (M:C ratio of 25:75, 50:50, and 75:25 by volume). The grades were selected to minimize the processing required while attempting to provide microstructural features characteristic of those encountered across a continuously graded profile. The materials were fabricated using tape casting and hot pressing techniques. The thermal dilation, elastic, and mechanical properties of the composites were determined. These properties, along with composite fractography, aid in the understanding of residual stress development and mechanical behaviour of uniform M/C composites and FGMs.

Unexpected problems concerning this material system and its processing were realized during material characterization. These findings suggest that alternative elemental materials, along with careful control of processing, are necessary to conceive an effective model system. Nevertheless, this study provides insightful information

regarding the microstructural development in powder processed M/C FGMs; identifies processing challenges for the realization of FGM fabrication; and provides an understanding of the mechanical behaviour expected along an M/C FGM profile.

This thesis is divided into several chapters. An initial background chapter reviews FGM technology and current research interests, FGM microstructural characteristics, important variables governing tape casting and densification, and the mechanics of M/C composites. A separate chapter is devoted to material processing as the bulk of the initial work in this project involved the successful fabrication of composite materials. The experimental procedures chapter covers specimen preparation and evaluation techniques. The results chapter describes the composite microstructures (from both optical and electron microscopy evaluation) and summarizes the properties measured from the composites and elemental materials. The discussion chapter provides a detailed assessment of the results with the incorporation of ideas from previous chapters.

## CHAPTER 2

### BACKGROUND INFORMATION

This chapter begins with a review of the important aspects driving FGM research. The microstructural variations anticipated in M/C FGMs developed via powder processing are described through the use of percolation theory. The important features of tape casting and porous body consolidation are also addressed. The remainder of the chapter describes the mechanical characteristics of metals, ceramics, M/C composites, and M/C FGMs. The applicability of atomistic and continuum based models in describing FGM mechanical behaviour are addressed.

#### 2.1 FGM History

The modern development of a Functionally Graded Material (FGM) originated in 1984 by Niino at the National Aerospace Laboratory of Japan and his colleagues in Sendai (Koizumi, 1992). The concept was developed as a solution to the need for thermal barrier materials in such applications as space structures and fusion reactors. More specifically, materials which could endure great temperature gradients, long exposure to high temperature, and oxidation (i.e. demands unattainable from conventional materials) were in demand (Niino and Maeda, 1990). In response, in 1987, the National

Project for the research and development of FGMs for high temperature structural applications was initiated by the Space and Technology Agency (STA) of Japan (Koizumi 1993). A five year objective was established to investigate the effectiveness of FGMs in applications requiring the relaxation of thermal stress. Phase 1 (1987-89) involved producing small FGM specimens, 1-10 mm thicknesses and 30 mm diameter, for endurance testing at a maximum temperature of 2000 K with a temperature gradient of 1000 K (Koizumi, 1993). Positive results from phase 1 encouraged phase 2 studies (1990-91), in which large FGM pieces were successfully developed and tested (specifically a SiC/C FGM, 300 mm square by 1-10 mm thick, designed for the fuselage of space planes and semi-spherical SiC/C FGM bowls, 50 mm in diameter, for space craft nose cones).

In 1988 a Japanese forum was established to promote FGM research nationally as well as to seek out potential FGM applications other than those aimed at relaxation of thermal stress. About 200 potential FGM uses were suggested ranging from structural to electronic, chemical, optical, nuclear, and biological (FGM Forum, 1991). In 1990 a committee was established to promote FGM R&D internationally. Currently, work in Japan has focused on new FGM applications and development (Koizumi, 1993). FGM research activities in Europe (Kaysser and Ilschner, 1995) and North America are not coordinated by national programs but instead by individual institutions and universities. These efforts range from FGM fabrication development, FGM profile design (stress reduction or other functional gradient), and FGM component testing.

There are various techniques available to fabricate FGMs (Sasaki and Hirai,

1991). Examples of some synthesis methods along with appropriate material systems are listed in Table 2.1. The appropriate choice depends on material system selection, specimen geometry, and application (e.g. coating or through thickness transition). Depending on design requirements and fabrication complexity, FGMs can be created with continuous or discontinuous microstructural profiles as shown in Figure 2.1.

Reviews have been conducted of the various modelling approaches developed to predict FGM properties (Markworth and Saunders, 1995; Markworth et al., 1995). Numerous investigations have focused on thermophysical properties to optimize thermal stress relaxation. Attempts at modelling the mechanical response of FGMs have not, in general, incorporated sufficient fundamental science. In addition, little work has been done to characterize the microstructure-property relationship for these materials. In general, the properties of select composite grades are measured or estimated for a given system and then implemented into an FGM design model. The predictive accuracy of these models for mechanical response is thus speculative.

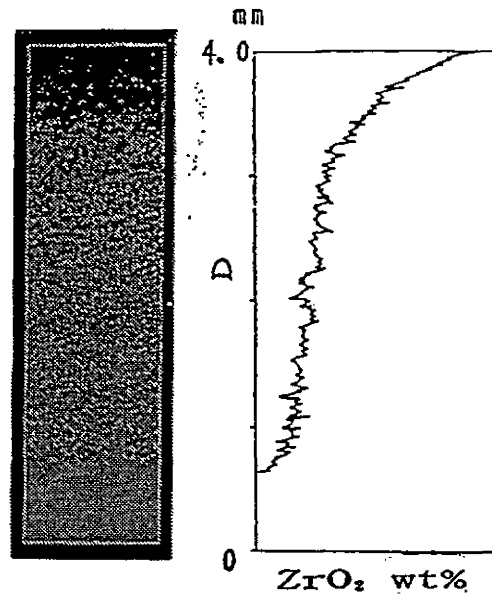
The design, fabrication, testing and modelling of FGMs are still in the initial stages of development. Many research opportunities exist in each category. A research contribution of specific interest involves developing an improved understanding of the relationship between microstructure and mechanical behaviour in M/C FGMs produced via solid state powder processing.

## **2.2 M/C FGM Microstructural Distributions**

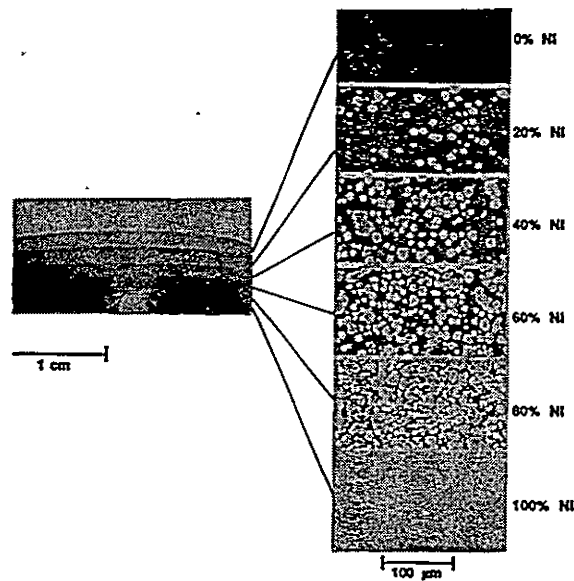
The microstructure of an FGM changes as the volume ratio of the constituent

**Table 2.1:** FGM synthesis methods and systems (Sasaki and Hirai, 1991).

Phase	Method	Examples of FGMs
Gas	CVD	SiC/C, SiC/TiC, TiC/C, C/C-C
	Ion Plating	TiN/Ti, TiC/Ti, ZrO <sub>2</sub> /Cu, C/Cr
	Plasma Spraying	YSZ/NiCrAlY, YSZ/NiCr
Liquid (Melt)	Electrodeposition	Ni/Cu
	Plasma Spraying	YSZ/NiCrAlY, YSZ/NiCr
	Eutectic Reaction	Si/ZrSi <sub>2</sub>
Solid	Self-Heating System	TiB <sub>2</sub> /Cu, TiB <sub>2</sub> /Ni, TiC/Ni
	Smearing	ZrO <sub>2</sub> /Ni, PZT/Ni, PZT/Nb
	Sintering	YSZ/SUS, YSZ/Mo, Si <sub>3</sub> N <sub>4</sub> /Ni
	Diffusion	Ni/Al



(a)



(b)

**Figure 2.1:** Examples of FGM microstructure profiles (a) continuous Ni/ZrO<sub>2</sub> (Kuroda et al., 1993), (b) discontinuous Ni/Al<sub>2</sub>O<sub>3</sub> (Rabin and Heaps, 1993).

phases changes (see Fig. 2.1). For this FGM study, powder processing techniques have been implemented to fabricate uniform M/C composites. The morphological changes anticipated across a continuous FGM profile can be described using percolation theory (Nan et al., 1993).

Phase distribution refers to the general arrangement of one phase with respects to another. The microstructural distribution of a two phase mixture changes with a change in phase ratio resulting in three types of geometric morphologies (Nan, 1993). Such understanding can be applied to an FGM profile as follows. Choosing the ceramic side of an FGM as a reference, a microstructural profile exists whereby the fraction of metal phase (in the form of dispersed particles) gradually increases toward the metal side (Fig. 2.2a,b). With an increase in metal phase fraction the metal particles aggregate to form large clusters (Fig. 2.2c). At the percolation threshold, the metal clusters interconnect forming a three dimensional continuous percolation network (i.e. the threshold identifies the geometric connectivity transition, Fig. 2.2d). In a two phase mixture this percolation represents the onset of the co-continuous phase regime of the microstructure. Similarly, a microstructural transition of ceramic particles occurs from the metal-rich side.

Percolation theory can be applied to continuum problems such as that describing the phase percolation in a two phase microstructure. The threshold volume fraction for percolation ( $v_c$ ) in a random three dimensional mixture of approximately equal sized spheres is 0.15 (Sher and Zallen, 1970). In practice, most two phase mixtures closely abiding by these requirements do in fact exhibit a percolation threshold in the range of

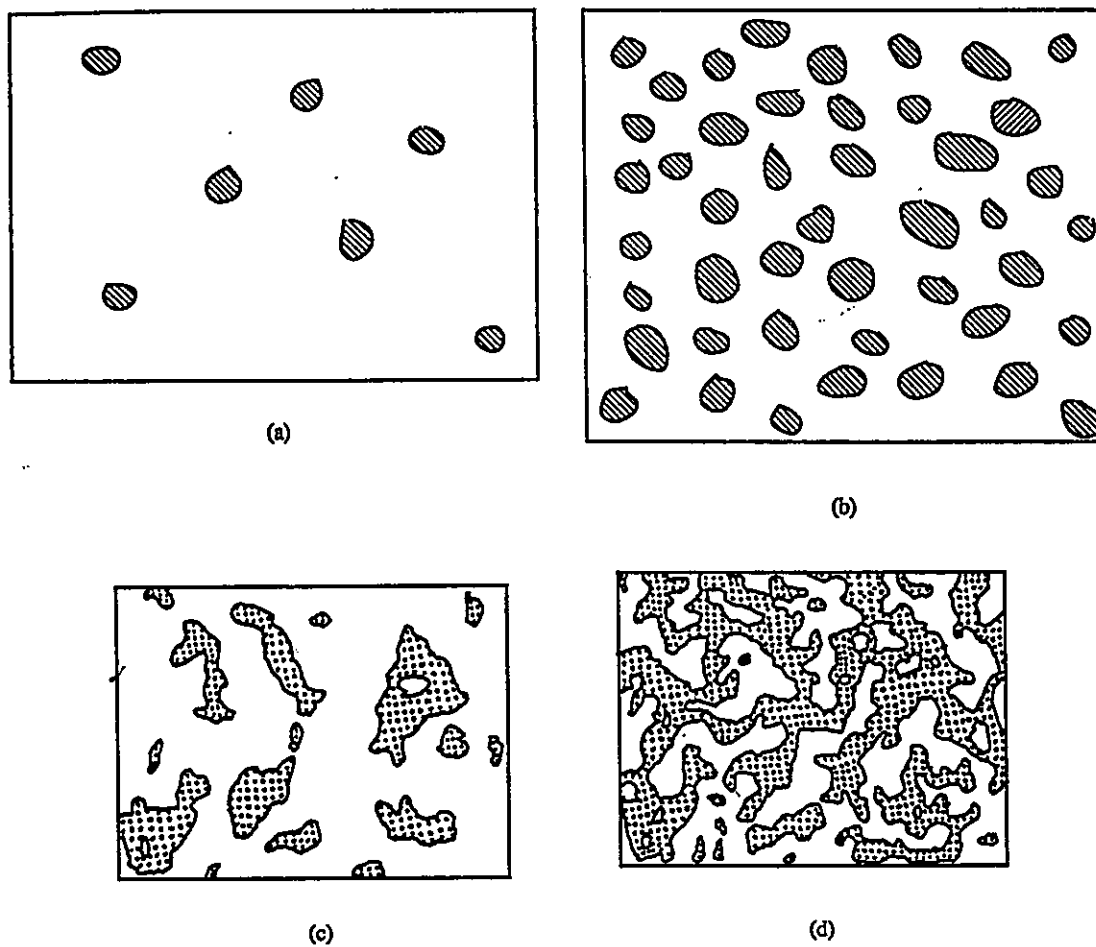


**Figure 2.2:** Schematic microstructure of two-phase heterogeneous materials (Nan, 1993). (a) randomly dispersed grain structure, (b) uniformly dispersed grain structure, (c) aggregated grain structure, (d) percolation-like cluster structure.

0.14 and 0.16 (Nan, 1993). For general composite media, percolation thresholds vary from less than 0.01 to greater than 0.5, depending on structural parameters such as particle size ratio, shape and distribution of the two phases.

### 2.3 Tape Cast Processing

Of the various techniques of producing FGMs, solid state powder processing was selected for the current study. Such methods involve powder blending, blend compaction, and sintering steps. Creating homogeneously dispersed powder mixtures can be a problem via direct mixing of powders but can be achieved by using colloidal processing. One such method is tape casting.

The tape casting process consists of suspending finely divided inorganic powders in liquid systems (aqueous or nonaqueous) comprised of solvents, plasticizers, and binders to form a slurry that is cast onto a carrier substrate (Williams, 1976). Upon solvent evaporation a thin sheet with well dispersed, homogeneous powder characteristics is achieved. The dried tapes are uniform with high green density and exhibit properties of strength and flexibility which enables cutting, laminating and forming operations prior to burnout and subsequent sintering. The tape casting process was first applied to the fabrication of ceramic powders in 1947 (Howatt et al., 1947). Many reviews of the tape casting processes have been published (Roosen, 1988; Williams, 1976; Mistler et al., 1978). Along with a brief review of organic tape casting, this section describes the important parameters regarding slurry development.

It is desirable in tape casting to produce uniform high density green bodies as this

will provide improved densification and reduce specimen shrinkage. Nonuniformity can result from agglomeration, particle segregation (due to sedimentation in the slurry and cast tape) and gas entrapment within a tape or laminate. Developing tape casting strategies which maximize the solids loading while minimizing the solvent and organic content, and controlling particle dispersion and slurry viscosity is thus crucial. A pseudoplastic slurry behaviour is desirable for tape casting. A characteristic of this behaviour is that the local slurry viscosity decreases due to the shear forces between the blade and slurry; yet upon passing the blade no shear forces are operative; hence increased viscosity resumes. The slurry viscosity prior to casting must be low enough to enable the casting operation, while high enough to prevent sedimentation in the slurry and later in the drying tape. Prior to casting, the solvent level should be sufficient so that the consistency of the slurry is comparable to heavy cream. Typical slurry viscosities prior to casting are between 5 and 25 Pa s for casting shear rates up to 1000  $s^{-1}$ .

Typical casting slurries contain inorganic powder, solvent, dispersant, binder and plasticizer. The composition of a typical slurry for tape casting alumina is given in Table 2.2 (Williams, 1976). First the selected starting powders must be characterized in terms of particle size, distribution, and surface area. In general, relatively fine powders in the order of 1 to 4  $\mu m$  (Roosen, 1988) are used since fine powder aids in dense particle packing in the slurry. The increased specific surface area resulting from fine powders increases the amount of shrinkage during drying and sintering. Powder characteristics however also influence the quantities of slurry ingredients required. For example, finer

**Table 2.2:** Slurry formulation for tape casting of alumina substrates (Williams, 1976).

Material	Function	Wt. %
Alumina	Ceramic Matrix	59.5
MgO	Grain Growth Inhibitor	0.5
Trichloroethylene	Solvent	23.0
Ethanol	Solvent	8.9
Menhaden Fishoil	Dispersant	1.0
Poly(vinyl butryal)	Binder	2.5
Poly(ethylene glycol)	Plasticizer	2.1
Diocyl Phthalate	Plasticizer	2.5

particle sizes and higher surface area require reduced solids loading and higher dispersant and organic levels (Plucknett et al., 1994).

To promote efficient evaporation, the solvent should have a low viscosity, a low boiling point and a high vapour pressure. A combination of solvents in azeotropic proportions are advantageous in providing a low viscosity. The solvent system should dissolve the binder, plasticizers, and dispersant, but should not react with the inorganic powders. Mixtures of trichloroethylene (TCE) and ethanol are commonly used.

A dispersant is essential for stabilizing a powder dispersion in the slurry. A well dispersed stable system supports the development of uniform dense particle packing, whereas an unstable system tends to agglomerate, which results in a porous matrix of low density. Dispersants provide repulsive forces between particles by electrostatic and/or steric stabilization. A review by Moreno (1992) discusses the role and mechanisms of different dispersants. Dispersants are typically added in concentrations of 0.5 to 2 wt% (Roosen, 1988). The optimum dispersant concentration typically corresponds to a minimum in slurry viscosity as shown in Figure 2.3. Optimizing the dispersant concentration in this way supports a high solids loading in the slurry. The addition of binder and plasticizer does not affect the location of the minimum in the viscosity vs. dispersant concentration curve, but the viscosity assumes a value about sixty times higher due to the binder (Braun et al., 1985).

Phosphate esters (PE) have been reported as very effective dispersants for slurries of alumina (Chartier et al., 1987), alumina/zirconia (Boch et al., 1986), and barium titanate (Morris and Cannon, 1986). However, PE does not pyrolyze until  $\approx 800^{\circ}\text{C}$  and

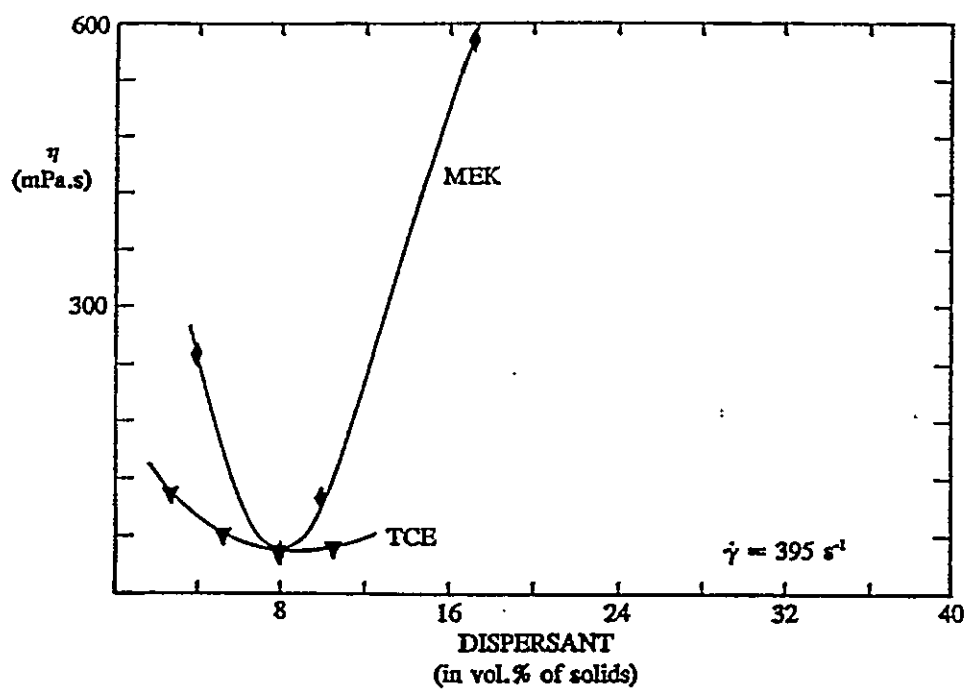


**Figure 2.3:** Effect of phosphate ester-dispersant on alumina slurry viscosity for two different solvents (Plucknett et al., 1994).

may leave some phosphorus, typically <100 ppm (Cannon et al., 1989). Although uncertainties exist regarding the mechanism of PE deflocculation, it has been reported that PE acts as steric dispersants in TCE-ethanol solvent by anchoring the long chain molecules to the particle surfaces (Mikeska and Cannon, 1964; Morris, 1967) and electrostatic stabilization predominates in methylethyl ketone-ethanol mixtures (Plucknett et al., 1994). While others (Cannon et al., 1989) claim that, due to strong short range Van der Waals forces, steric stabilization is not effective unless a polymer has a molecular weight >10000, and dispersants like PE have molecular weights below 1000.

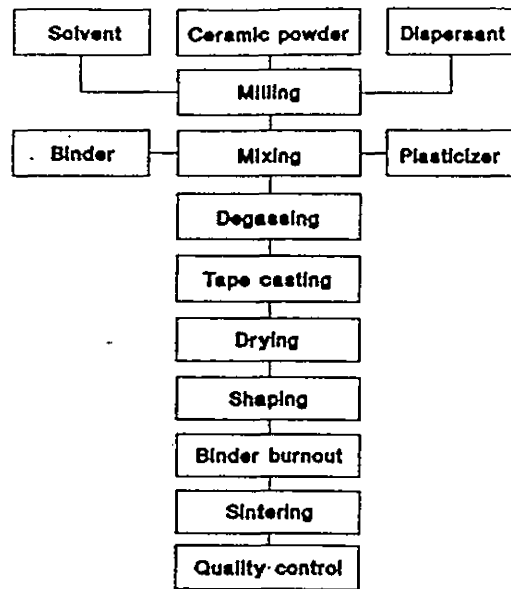
Binders are polymeric molecules that adsorb onto the particle surface forming organic bridges between them. The binder provides the tape its strength while the plasticizers provide its flexibility. The binder-plasticizer system should meet the following criteria: (1) be present in low concentrations, well under 10 wt%; (2) support stabilization of the system against flocculation; (3) exhibit a low glass transition temperature so that a sufficient mobility is ensured for diffusion, and for flexibility after solvent removal; (4) not retard solvent evaporation; (5) volatilize to a gas leaving no residual carbon or ash during firing; and (6) remain stable at ambient conditions during storing. Plasticizers have a lower molecular weight which contributes to a lower glass transition temperature but also to reduced strength. An optimized binder-plasticizer system ensures a close spacing of particles while filling all pores between them. A commonly used binder-plasticizer system is poly(vinyl butryal) and poly(ethylene glycol), (Moreno, 1992). PVB has a molecular weight of about 32 000. Often the use of two plasticizers is synergistic; for example, the combination of PEG and dioctyl-phthalate,

which have molecular weights of 400 and 390 respectively.

In order to achieve a binder system that offers clean burnout characteristics, the burnout environment is crucial. Burnout in reducing or nonreactive gases cause the polymers to pyrolyze resulting in their decomposition and removal; while, oxidizing environments facilitates combustion and more effectively removes the organic material. Reducing atmospheres are frequently used to prevent oxidation of tape cast refractory metals. Thermal decomposition of PVB in such atmospheres produces an organic residue which can be the origin of some defects after sintering (Cima and Lewis, 1988).

The typical procedure used for tape casting is shown in Figure 2.4a. The sequence of slurry preparation is of great importance. First, a mixture containing the starting powder, solvent and dispersant is ball milled for period of about 24 hours during which soft agglomerates are broken down and dispersant adsorbs on the particle surfaces. The binder and plasticizer ingredients are subsequently added and the slurry is mixed for a duration of up to 24 hours. If milling is performed for an insufficient or an excessive duration in the presence of binder poor green densities result (Mistler et al., 1978). The slurry is then degassed to remove dissolved gases resulting from the mixing operation. The slurry is then poured into the reservoir of the doctor blade unit (see Figure 2.4b) and cast on to a substrate. Following solvent evaporation, the tape can be removed from the substrate and cut to the desired shape. Solvent evaporation and subsequent organic removal yields a porous green part. Binder burnout removes the organic materials through open porosity channels and provides the point contacts between particles which provides green part strength and facilitates subsequent sintering transport.

(a)



(b)

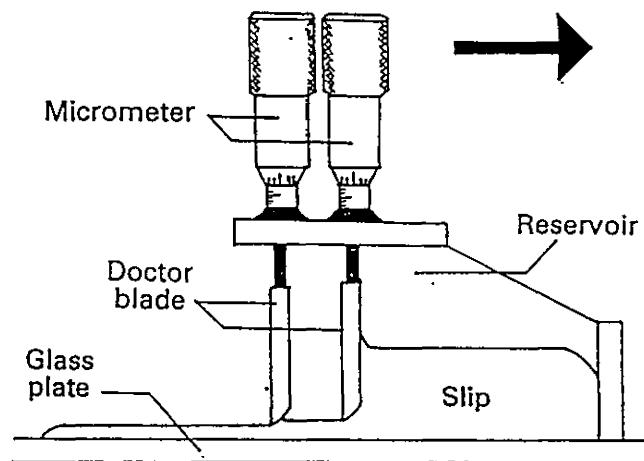


Figure 2.4: (a) Ceramic processing flowsheet (Roosen, 1988), (b) doctor blade apparatus.

## 2.4 Powder Consolidation

Solid state consolidation mechanisms occurring during sintering and hot pressing are now addressed. Sintering is commonly defined as a process in which powder compacts densify and develop useful properties under heat treatment. Hot pressing, which involves pressure assisted sintering, offers advantages in the densification of powder compacts. Detailed reviews of the mechanisms involved in sintering and hot pressing have been published (Richerson, 1992; Wu, 1986).

### 2.4.1 Theory of Sintering

The driving force for powder sintering is the difference in free energy or chemical potential (which is related to powder surface curvature) between surfaces of particles and points of contact between adjacent particles. The finer the powder the larger the initial surface area hence the larger the driving force for densification. Densification during solid state sintering is facilitated by volume diffusion mechanisms. Diffusion is activated via thermal energy, in conjunction with chemical potential gradients due to particle-particle contact and surface tension (Richerson, 1992).

Solid state sintering is conceptualized in a sequence of three steps. During the initial stage neck growth occurs between the powder grains and grain boundaries are created. In the intermediate stage necks between particles grow, porosity decreases so that the centers of the original particles move closer together, and grain boundaries begin to move via grain growth processes. The porosity remains continuous as cylinders along three grain edges which meet at four grain corners (Wu, 1986). The final stage of

sintering involves the final removal of porosity which is now discontinuous and relies on vacancy diffusion along grain boundaries for its removal. It is important during this stage to control grain growth since rapid grain boundary movement can leave pores isolated within grain interiors which significantly increases the atomic distance between pore and boundary, hence effectively terminating densification.

#### 2.4.2 Theory of Hot Pressing

Compared to conventional sintering, hot pressing offers a number of processing advantages, including: (1) reduced temperature and time required for densification; (2) densification in materials which do not readily undergo densification during conventional sintering; and (3) attainment of higher density with less grain growth. The effectiveness of hot pressing arises because the applied pressure directly assists the densification process while leaving grain growth relatively unaffected. Several reviews provide discussion of hot pressing in ceramics (Coble, 1967; Spriggs and Dutta, 1973; Stuijts, 1973).

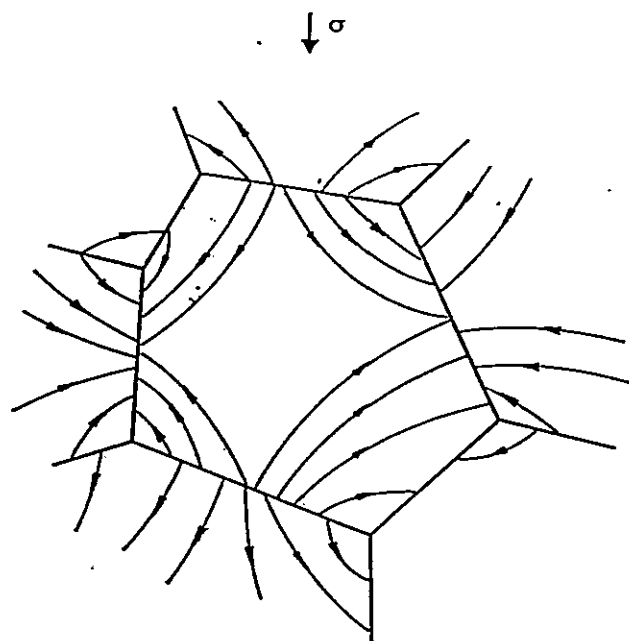
Along with the atomic processes occurring during conventional sintering which contribute to densification of a compact, hot pressing improves densification by particle rearrangement, dislocation flow and diffusion enhancement (Wu, 1986). During early stages of hot pressing, particle rearrangement by sliding and fragmentation can increase powder packing and increase the number of point contacts. High applied pressures at high temperatures can activate dislocations giving rise to plastic deformation. This effect is significant during early stages of hot pressing due to the high stresses present at

particle contacts. Dislocation flow has been found significant in the hot pressing of plastic materials such as silver (Lenel and Ansell, 1967) and copper (Smith and Vasilos, 1964). Applied stress enhances lattice and grain boundary diffusion contributing to improved densification during the hot pressing of many ceramics (Vasilos and Spriggs, 1963; Coble and Ellis, 1963; Rossi and Fulrath, 1965). Figure 2.5 illustrates the atomic flux, via volume diffusion and grain boundary diffusion, during consolidation by axial hot pressing. Essentially in regions normal to applied stress, atoms have higher chemical potential than unstressed or tensile stressed regions, hence diffusion is increased in the plane normal to the applied stress.

## **2.5 Mechanical Behaviour of Metal/Ceramic Composites**

The microstructural distributions expected in powder processed M/C FGMs were described in Section 2.2. From this it is concluded that there exists two distinct regimes in the FGM profile: discrete particulate and interconnected morphology. Although this cognisance is necessary for our investigation, the mechanical properties of each phase, interphase bonding characteristics and phase interactions must be understood to discern the mechanical behaviour of M/C FGMs. For this we can turn to the basic physics of metals and ceramics and then consider their interactions in M/C composites. With knowledge of FGM microstructure and M/C composite mechanics, the applicability of micromechanical and macromechanical approaches to model the behaviour of M/C FGMs can be investigated.

(a)



(b)

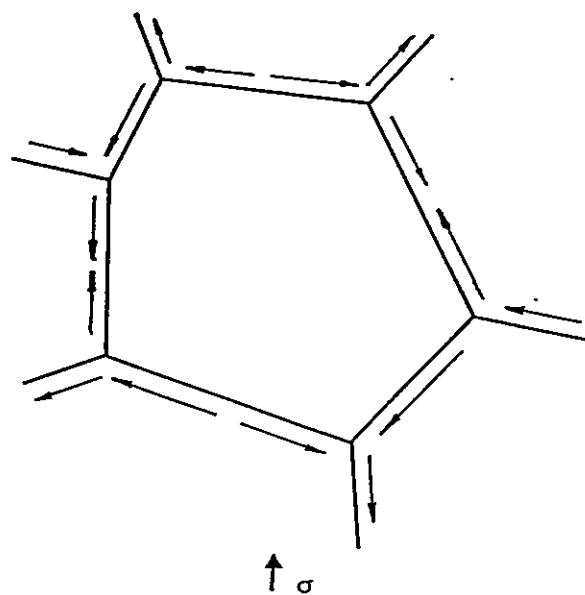


**Figure 2.5:** Atomic flux during sintering under an applied stress. From models of (a) Nabarro-Herring creep, (b) Coble creep.

### 2.5.1 Mechanical Characteristics of Metals and Ceramics

To understand the mechanical behaviour of M/C FGMs it is first necessary to grasp the elastic and mechanical behaviour of metals and ceramics. Ceramics typically exhibit higher stiffness (i.e. moduli), lower coefficients of thermal expansion (CTE), higher intrinsic bond strength, and much lower toughness than metals. The reasons for these differences comes from the basic nature of bonding in these materials. Oxide ceramics incorporate combinations of ionic and covalent bonding, which provide bonding forces that are stronger than metallic bonds. As a result typical metals like iron have a Young's modulus ( $E$ ) of 200 GPa and CTE of  $12 \times 10^{-6}/^{\circ}\text{C}$  and ceramics like alumina exhibit moduli of about 400 GPa and CTE of about  $9 \times 10^{-6}/^{\circ}\text{C}$ .

Although the elastic behaviours of metals and ceramics are similar, the mechanical and fracture properties are much different. Based on bonding considerations alone the theoretical strength for such materials is in the order of  $E/20$ . In practice, commercially pure metals exhibit yield strengths ( $\sigma_{ys}$ ) in the order of  $E/1000$  and ultimate tensile strengths of about  $3\sigma_{ys}$ . This occurs as a consequence of plasticity and dislocation mechanisms in metals which are not accounted for in the ideal strength model.

While metals exhibit similar behaviour under tension and compression ceramics exhibit vastly differing behaviour. Ceramics are very strong in shear, due to factors such as Coulombic repulsion, large Burgers vectors, and few inherent slip systems. This contributes to a high resistance to plastic flow at ambient temperatures. As a result, ceramics typically behave elastically up to the point of failure. If a ceramic could be created without flaws, its failure strength could approach the theoretical limit. However,

engineering ceramics do contain flaws and upon tensile loading notches act as stress concentrators, depending on the crack length ( $c$ ) and crack radius ( $\rho$ ) according to the Griffith crack model:

$$\sigma_m = 2\sigma_a \left(\frac{c}{\rho}\right)^{\frac{1}{2}} \quad [2.1]$$

Since high shear strengths result in crack radii in the order of atomic dimensions, very high stress concentrations ( $\sigma_m$ ) can develop at low applied stress ( $\sigma_a$ ). Under compressive stresses, such flaws are effectively closed and high strengths, approaching that of the theoretical limit, are typically achieved. Taking the example of high purity polycrystalline alumina, tensile and compressive strengths of 220 MPa and 3 GPa respectively are observed. Due to distributions in flaw size and populations in ceramics a high degree of variation (i.e a factor of 2) can be observed in the measured flexure and tensile strengths.

### 2.5.2 Behaviour of Metals and Ceramics within M/C Composites.

The behaviour of metals and ceramics processed separately will behave differently than their constituent counterparts within a M/C composite. Influences such as strain induced dislocations, thermal residual stresses, and grain size constraints contribute to these differences.

Upon cooling from processing or subsequent heat treatments, stresses develop due to a mismatch in the thermal expansion characteristics of each phase. Misfit strains, in the order of  $\Delta(\text{CTE})\Delta T$  must be shared by each phase. If the strains in the metal phase

are high enough to cause metal yielding, diffusional processes and plastic flow may accommodate thermal dilation. The result upon cooling is a work hardened metal with a residual component of tensile stress and a balancing compressive stress in the ceramic. It is generally accepted that the flow stress of a typical metal is proportional to the square root of the dislocation density,  $\rho$ , such that:

$$\Delta\sigma_p = \alpha G b \rho^{1/2}, \quad [2.2]$$

where  $\alpha$  is a constant between 0.5 and 1,  $G$  is the shear modulus, and  $b$  is the Burgers vector (Meyers and Chawla, 1984). Applying this equation to describe strengthening in composites implies the following assumptions (Humphreys, Basu and Djazeb, 1991): 1) the dislocations are uniformly distributed such that they represent a forest hardening component, and 2) stress is relieved solely by plastic flow. Humphreys (1991) mentions that although a pure aluminum matrix satisfies assumption 1, a solution hardened matrix exhibits a higher dislocation density adjacent to the reinforcement. In addition, not all of the misfit strain is relieved, hence leaving residual stresses in the matrix. Nevertheless, the model enables an estimation of MMC flow stress.

A model estimating the dislocation density versus volume fraction and particle size has been developed (Miller and Humphreys, 1990) and has the form:

$$\rho = 12(\Delta T)(\Delta CTE) \frac{V_p}{bd}, \quad [2.3]$$

where  $V_p$  is the volume fraction of ceramic phase and  $d$  is the ceramic particle size. This equation assumes that all of the stress is relieved by plastic flow hence gives an upper

bound estimate of matrix strength. For the iron and alumina example, cooled through a  $\Delta T$  of  $900^\circ\text{C}$ , with  $V_p=0.5$  and  $d=2\ \mu\text{m}$ , dislocation densities of  $2.5 \times 10^{13}\text{m}^{-2}$  and an increase in strength of  $\approx 100\ \text{MPa}$  can be expected. Comparatively, typical annealed metals contain dislocation densities in the order of  $10^{11}\text{m}^{-2}$ , while heavily work hardened metals can achieve  $10^{16}\text{m}^{-2}$ . In practical composites, both an increased dislocation density in the metal phase and residual stresses are thus expected upon fabrication.

Grain sizes in well dispersed powder processed M/C composites can vary between the initial starting powder size and a size approximately equal to the mean phase intercept length. This is especially true in interconnected morphologies where a grain of maximum size is surrounded by dissimilar phase neighbours. Such a grain size constraint may contribute to an increased flow stress in the metal phase as described by the Hall-Petch relation:

$$\Delta\sigma_d = kd^{-1/2}, \quad [2.4]$$

where  $k$  is a work hardening constant ( $k \approx 0.1\ \text{MPa}\sqrt{\text{m}}$  for most FCC metals). Thus the contribution of grain size strengthening to a metal with a grain size of  $2\ \mu\text{m}$ , is in the order of  $70\ \text{MPa}$ .

It may not be appropriate to apply the same Hall-Petch coefficients to the metal phase in a composite as that developed for homogeneous nickel. Hall-Petch strengthening was initially developed for polycrystalline metals. When nearest neighbour grains are phase dissimilar, larger dislocation pile-ups may result at the interface since dislocations cannot be transferred or generated in adjacent grains. This may contribute

to a higher average  $k$  coefficient in the Hall-Petch relation, hence increasing the grain size-strength dependence.

In summary the yield stress for the metal constrained within a M/C composite may be influenced by all of the above processes. As a first approximation it is appropriate to define the metal phase yield strength as a summation of the above contributions (Eqns. 2.2 and 2.4) as:

$$\sigma_{ys} = \sigma_o + \Delta\sigma_p + \Delta\sigma_d \quad [2.5]$$

Due to the characteristics of ceramics the dislocation strengthening and Hall-Petch relations are not applicable. However, the strength of a ceramic is dependent on the scale of the flaw size. Combining stress intensity considerations with Griffith's energy criteria, the fracture strength of a material can be written as:

$$\sigma_f = \frac{K_{IC}}{Y\sqrt{\pi c}} \quad [2.6]$$

where  $K_{IC}$  is the critical stress intensity factor or fracture toughness. Finer scale ceramics contain smaller flaws which thus results in ceramics of higher fracture strength.

### 2.5.3 Metal/Ceramic Bonding Characteristics

For metal-ceramic interactions to be operative, there must be sufficient M/C interfacial strength. Interphase strength depends on the nature of M/C bonding and on the degree of interfacial tortuosity. Depending on the material compatibility, interphase bonding can be facilitated physically or by a chemical reaction.

Physical bonding relies on Coulombic attraction between the ions of the oxide based ceramic and the free electron structure of the metal (Stoneham and Tasker, 1988; Finnis et al., 1990; Finnis, 1992). The attraction is balanced mainly by the repulsions between the ceramic ions and metal atoms. Energy is required to create a solid surface since the surface atoms or ions experience unbalanced bonding forces (Howe, 1993). Therefore, the driving force for the formation of a M/C interface is the decrease in free energy that occurs when intimate contact is established between the metal and ceramic surfaces. In the simplest case, this energy is equivalent to the work required to separate a unit area of interface into the two original surfaces ( $W_{ad}$ ). This energy can be written in the form of the Dupre equation (Murr, 1975; Adamson, 1960) as:

$$\gamma_{mc} = \gamma_m + \gamma_c - W_{ad} \quad [2.7a]$$

where  $\gamma_m$  and  $\gamma_c$  are surface energies of the metal and ceramic respectively and  $\gamma_{mc}$  is the metal-ceramic interfacial energy. From this equation it is evident that a low interfacial energy is conducive to high bonding strength. Considerable energy is usually absorbed by the metal and ceramic during interfacial fracture such that the relationship is best represented by:

$$W_{ad} \geq \gamma_m + \gamma_c - \gamma_{mc} \quad [2.7b]$$

where the work of adhesion includes the dissipative processes that occur upon separation (Howe, 1993).

Some evidence suggests that the bonding of ceramics to transition metals may be due to a covalent metal-oxygen anion bridge at an atomic scale (Johnson and Pepper,

1982). This hypothesis is supported by the observation that bond strength correlates with the free energy of oxide formation for transition metals; both increase in the order Ag→Cu→Ni→Fe→... Since this bonding occurs at an atomic level it is difficult to visually distinguish this mechanism from that of purely Coulombic attraction. Some researchers (Schonberger et al., 1992) have attempted to identify the lattice matching that occurs at such interfaces.

Chemical reaction bonding involves mass transport processes in the vicinity of the interface. The result is an intermediate phase joining the metal and ceramic such as in the case with nickel/alumina composites created in the presence of oxygen. The result is a spinel ( $\text{NiAl}_2\text{O}_4$ ), at the M/C interface. The resulting interfacial energy is generally lower than for physical bonding (Howe, 1993); however, the interface no longer conforms to equation 2.7.

Interfacial tortuosity contributes a mechanical interlocking component to interfacial strength of M/C composites. The relative effectiveness may depend on the scale and degree of interfacial roughness.

#### **2.5.4 Behaviour of M/C Composites**

Arsenault (1991) suggests that the increase in  $\sigma_y$ , observed in particulate M/C composites (via a 0.2% offset criterion) can be completely accounted for by the dislocation substructure created by the relaxation of thermal stresses. However Humphreys (1988) has shown, using SiC particulate reinforced aluminum, that quenching conditions expected to provide matrix  $\sigma_y$ , increases of 20 MPa experimentally yield

$\Delta\sigma_y \approx 100$  MPa. This observation suggests that the strength of the composite is not solely related to the dislocation substructure created in the metal upon cooling, but must instead be related to metal-ceramic interactions. The dependence of scale in modelling metal matrix composites has led to two approaches in modelling these materials. These are based on micromechanics and macromechanics. Some properties are structure insensitive and are themselves scale independent. These developments are of importance in the understanding and modelling of M/C FGM behaviour.

#### **2.5.4.1 Micromechanics vs. Macromechanics**

It has been shown that pure single crystals containing oxide dispersions of the order  $0.01 \mu\text{m}$  are well characterised by micromechanics while composites containing large scale fibres,  $0.1 \text{ mm}$  in diameter, have been shown to approximately obey continuum mechanics (Ashby, 1971). Chen and Argon (1979) state that the boundary between micromechanics and continuum mechanics is not clearly defined or agreed upon. However, they suggest that continuum methods can be considered for particles of several microns in size. The fundamentals of both models are presented here.

Micromechanics approaches are suitable for systems whereby dislocation-particle interactions significantly contribute to flow stress. Dispersion strengthening materials are examples of systems where such dislocation mechanics are operative. Some general features of micromechanics are:

1. strengthening effect is scale dependent,
2. particles are not considered load bearing, and

3. particles act as barriers to dislocation motion.

One strengthening mechanism in this regime involves the Orowan process. Upon sufficient stress ( $\Delta\sigma_r$ ) a dislocation will pass between adjacent particles leaving dislocation loops around the particles. The shear stress necessary to bend a dislocation to the critical radius before passing the particle contributes to an increased matrix flow stress of:

$$\Delta\sigma_r \approx \frac{Gb}{l}, \quad [2.8]$$

where  $l$  is the separation distance between particles. This stress approximates the increase in composite yield stress due to particles. Table 2.3 distinguishes some differences between dispersion strengthened alloys (DSA) and particulate MMCs. Considering nickel as an example matrix, equation 2.8 yields  $\Delta\sigma_r=300$  MPa for DSA (fine particles) and  $< 14$  MPa for MMCs (course particles). This indicates that Orowan strengthening may not be significant for MMCs and M/C composites.

As shown in Table 2.3, there are large differences between DSA and particulate MMCs. DSA systems contain fine second phase dispersions in the matrix. MMCs have second phase particles in the order of the matrix grain size. The particles in MMCs are typically at matrix grain boundaries. It is expected that these differences contribute to different dislocation-particle interactions in each case.

Continuum approaches are microstructural scale independent. Whereas dislocation particle interactions within the microstructure are important in dispersion strengthened models, they are in fact short order effects and are considered insignificant for large microstructures ( $\geq$  several microns). Continuum mechanics assumes an average

**Table 2.3:** Average and typical characteristics of dispersion strengthened alloys and particulate composites.

Comparison Category	Dispersion Strengthening ( $\mu\text{m}$ )	Particulate MMCs ( $\mu\text{m}$ )
Volume fraction	$\sim 0.01$ (0.001-0.1)	$\sim 0.2$ (0.05-0.4)
Particle size	$\sim 0.05$ (0.01-0.1)	$\sim 10$ (2-100)
Particle spacing	$\sim 0.35$ (0.05-2.5)	$\sim 15$ (2-300)
Matrix grain size	$\geq 10$	$\sim 10$ (2-100)

stress or strain in each constituent. Composite strength is a result of stress or strain partitioning between the two constituent phases under an applied load. Partitioning depends on the properties of the constituents, their volume fractions, and their geometrical arrangement within the composite (i.e. aspect ratio of reinforcement and alignment in the composite). Using the slab model as a simplified case representing composite behaviour the following expressions are derived:

$$\sigma_c = \sigma_f V_f + \sigma_m V_m \quad [2.9a]$$

$$\epsilon_c = \epsilon_f V_f + \epsilon_m V_m \quad [2.9b]$$

Consider a continuous fibre reinforced MMC. Loading the composite parallel to the fibre orientation leads to stress partitioning (i.e.  $\epsilon_f = \epsilon_m$ ), whereas loading the composite perpendicular to the fibre orientation results in strain partitioning ( $\sigma_f = \sigma_m$ ). Equations 2.9a and 2.9b set the upper and lower bounds of mechanical properties for most fibre reinforced composites. To a first approximation dispersed particulate composites may be represented by equation 2.9b.

In terms of describing flow characteristics of composites, the model is too simplistic as the behaviour of most two phase systems do not agree with the model (Fan, Tsakiropoulos and Miodownik, 1994). The slab model approach neglects considerations of matrix-second phase load transfer and fibre end stresses, which are important considerations for discontinuous reinforced composites. More sophisticated models, such as the modified shear-lag model considers the shear transfer between matrix and fibre (contribution by Cox, 1952) and includes a correction for fibre end loading (contribution

by Fukuda and Chou, 1981). For particulate composites, other methods such as those incorporating the Eshelby inclusion method (Eshelby, 1957) may provide a more accurate account of mechanical response.

Note that equations 2.9a,b are special cases of the linear rule of mixtures, which states that the properties of the composite  $P_c$  are simply the weighted average (by volume) of the properties of the individual components  $P_i$ . Evaluating composite properties in series (Voigt model) or in parallel (Ruess model) yields the following general relations:

$$P_c = \sum P_i V_i \quad [2.10a]$$

$$\frac{1}{P_c} = \sum \frac{1}{P_i V_i} \quad [2.10b]$$

#### 2.5.4.2 Structure Insensitive Properties in M/C FGMs

Some composite properties are structure insensitive (eg. specific heat, density, and to a first approximation, modulus and CTE) and thus are basic functions of the materials present, regardless of reinforcement shape, size or distribution. Such properties are often closely approximated by the linear law of mixtures in the form proposed by Voigt (Eqn. 2.10a).

#### 2.5.4.3 Mechanical Interactions in M/C FGMs

The M/C interactions operative across an FGM profile may depend significantly

on phase volume and microstructure. As previously alluded (Section 2.2), the microstructure across an FGM profile involves two phase continuity transitions. Pure component morphologies exist at both the metal and ceramic limits of the FGM. Dispersed particulate systems exist up to about 15 volume percent of second phase. The remaining microstructure will consist of an interconnected phase morphology. These composite regimes can be simplified into three categories:-

1. particulate dispersed metal matrix composites,
2. metal-ceramic interconnected morphologies, and
3. metal dispersed ceramic matrix composites.

Due to the scale of the particles in composites represented by regime 1, it is unlikely that dislocation mechanics can account for the observed strengths. Regimes 2 and 3 contain an interconnected ceramic phase acting as long scale reinforcements. Based on these considerations it is expected that the mechanical behaviour across the FGM profile will be best described using continuum mechanics.

Alternatively, the behaviours in each of these regimes may be considered more specifically. It has already been established that regime 1 represents a particulate MMC system. The microstructure of regime 2 may be considered analogous to fibre reinforced structures. Regime 3 may be best characterized as a dispersed metal toughened ceramic. Reviews of ceramic toughening by ductile reinforcements have been made by Ruhle and Evans (1989).

## 2.6 Summary

This review has covered an introduction to FGM technology, a description of powder processing technology, a discussion of two phase microstructure development resulting from powder processing, the details behind tape casting and subsequent consolidation, and the mechanics of uniform M/C composites. The focus of this review was two fold: (1) to provide the necessary background to solid state processing of M/C composites, and (2) to establish concepts describing the microstructure-property relationship of M/C FGMs. Although the microstructural profile anticipated across an FGM is understood, the characteristics of metal-ceramic interaction have only been speculated. This review provides a framework for the work completed in this thesis.

## **CHAPTER 3**

### **MATERIAL SELECTION AND PROCESSING**

Great efforts have been pursued to fabricate the metal/ceramic composites in this study. This chapter emphasizes the development of tape casting, binder burnout and consolidation techniques. Each stage is described as a sequence of events leading to a satisfactory result. To commence this chapter, material system selection criteria and details about the system selected for this study are addressed.

#### **3.1 Model-System Materials Selection for M/C FGM Study**

##### **3.1.1 Material Selection Criteria**

The development of a model system to study M/C FGM behaviour involves consideration of fabrication method, thermal/elastic property comparisons, and material chemical compatibility. In addition, it was desired to select a material system that could be fabricated using solid state powder processing techniques, namely tape casting and sintering. As such, phase density differences during colloidal processing (to avoid tape inhomogeneities) and phase sinterability during consolidation become important considerations.

In two phase composites any mismatch in coefficient of thermal expansion (CTE)

will result in residual stresses upon cooling from processing or upon subsequent thermal exposure. Phase elastic moduli are important as they affect the overall composite dilation and determine the magnitude of residual stress within each phase (i.e. lower moduli produce lower overall residual stress). When dealing with a brittle and a ductile phase under residual stress it is desired to sustain a state of residual compression in the brittle phase. It is therefore desirable to select materials with the metal exhibiting a CTE equal to or slightly larger than the ceramic CTE. In developing FGMs for thermally gradient applications, it becomes additionally important that the CTEs are relatively low to prevent failure under conditions of thermal stress.

Material chemical compatibility refers to the knowledge of any chemical reaction products between the metal and ceramic. It was desired to select a system without a reaction, where interphase adhesion could be accomplished through physical bonding.

Powder sinterability requires that both phases can be consolidated below the melting temperature of the metal phase. Powder sintering characteristics depend on particle size and melting temperature. Finer powders increase the driving force for surface diffusion hence lower the sintering temperature. The melting temperature for a powder indicates the level of atomic bonding strength; thus, higher melting temperatures suggest higher sintering temperatures. Hence a higher melting point supports a higher sintering temperature.

### **3.1.2 Materials Selected**

Table 3.1 lists some potential metal and ceramic components for a model system.

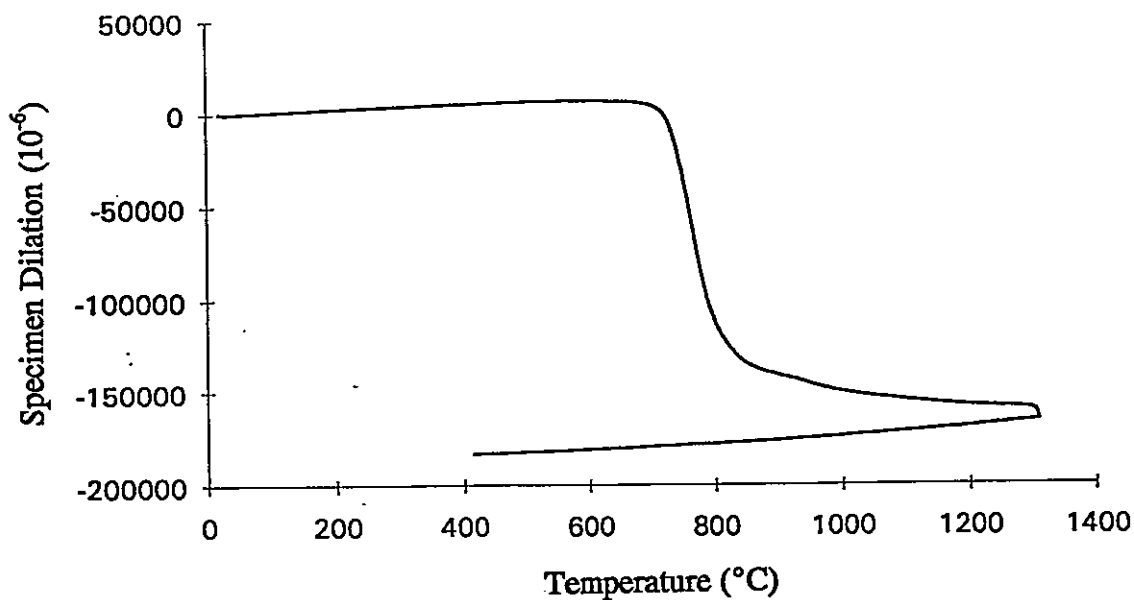
**Table 3.1:** Potential M/C "model system" components for FGM characterization. Properties taken from CRC Handbook 1985-1986.

Material	Coefficient of Thermal Expansion @ 25°C ( $\times 10^{-6}/^{\circ}\text{C}$ )	Melting Temperature (°C)
$\alpha\text{-Al}_2\text{O}_3$	9	2020
ZrO <sub>2</sub>	10	2700
Ti	8.5	1665
Ag	19	960
Ni	13	1455
Fe	12	1535
Cu	17	1080
Al	22	660

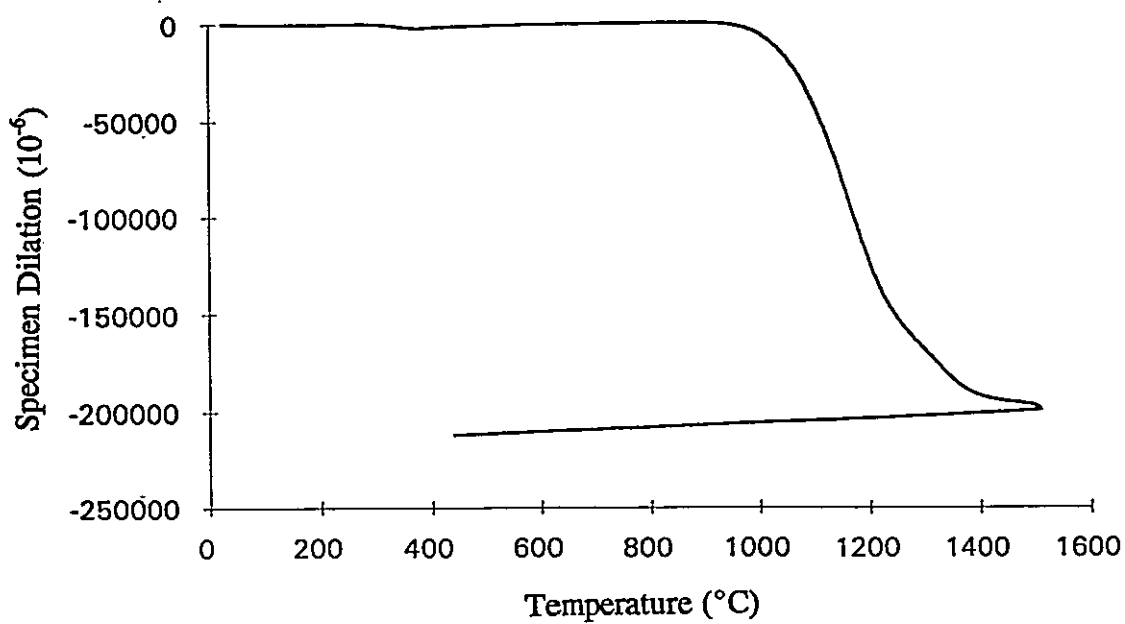
Unfortunately alumina reacts with most of the metals listed creating an interfacial spinel phase. Zirconia is not expected to react with any of the metals listed. Both nickel and iron exhibit properties that are similar to zirconia. Iron however is allotropic and will transform ( $\alpha$ - $\gamma$ ) at 912°C resulting in a phase change and a discontinuous volume expansion upon cooling. Since this would complicate the stress state developed within the composite, iron remains as a second choice. Nickel exhibits a second order transformation at the curie temperature. Although this results in an inflection in the CTE-temperature dependence, it is a small continuous change compared to the instantaneous change accompanying a first order transformation. On this basis, nickel and zirconia were selected as model system components in this M/C FGM study.

This leaves the issues of component chemical compatibility and phase sinterability. Reported studies reveal clean interfaces between nickel and zirconia when diffusion bonded in vacuum (Qin and Derby, 1992; Wagner, Kirchheim and Ruhle, 1992). Sintering in the presence of air can result in a nickel oxide region separating zirconia from nickel without a Ni-Zr<sub>x</sub>O<sub>y</sub> reaction product. Chemical compatibility between nickel and zirconia is therefore satisfied. The sinterability of nickel and zirconia was determined by volume dilation experiments performed on homogeneous green bodies nickel and zirconia. The densification curves shown in Figure 3.1 indicate that nickel and zirconia show rapid shrinkage rates at about 750°C and 1150°C respectively. Since these are comparable, yet well below the melting point for nickel (1455°C), composite sinterability is satisfied.

The nickel powder selected was the ONF grade produced by hydrometallurgy at



(a)



(b)

**Figure 3.1:** Pressureless sintering dilatation for powder compacts of (a) ONF-nickel, (b) TZ0-zirconia.

Sherritt Technologies. Details regarding the production of nickel from hydrometallurgy can be found elsewhere (Burkin, 1966; and Gilchrist, 1989). The characteristics of this powder (determined at McMaster) are: average grain size of about  $1.9 \mu\text{m}$  (standard deviation of  $1.3 \mu\text{m}$ ) and specific surface area of  $4 \text{ m}^2/\text{g}$ . The powder purity was evaluated using X-Ray Fluorescence in the Geology Department at McMaster. Analyses for oxygen and carbon were performed using the Leco<sup>®</sup> inert gas fusion method and the Leco<sup>®</sup> combustion/volumetric method respectively. Table 3.2 lists the impurity levels for the nickel powder.

Among the various grades of zirconia available (i.e. monoclinic, tetragonal, or cubic stabilized polymorphs) and stabilizer additives (eg. CaO, MgO and  $\text{Y}_2\text{O}_3$ ) Tosoh grade TZ8Y (i.e. containing 8 mol%  $\text{Y}_2\text{O}_3$ ) was selected. The substitution of yttria ions for zirconia ions in the formation of a solid solution creates a stable fluorite structure ( $\text{c-ZrO}_2$ ) when alloyed with  $\geq 8 \text{ mol}\% \text{ Y}_2\text{O}_3$  (Kim and Tien, 1991). Selection of cubic zirconia was made to avoid any thermal or stress induced transformations which can occur in non-cubic grades. Such transformations may complicate composite fabrication and mechanical response of the composites and thus make modelling of the system more difficult. TZ8Y powder is made via a hydrolysis technique which coprecipitates  $\text{ZrO}_2$  and  $\text{Y}_2\text{O}_3$  crystals of about 25 nm diameter. The powder is then calcined and milled to create a single phase oxide with an average particle size of  $0.15 \mu\text{m}$  and a specific surface area of  $15.7 \text{ m}^2/\text{g}$ . Calcining treatments of this type are typically performed near  $500^\circ\text{C}$ . The components and impurities of this powder (TZ8Y), provided by Tosoh, are listed in Table 3.2.

**Table 3.2:** Powder composition analysis for ONF-nickel and TZ8Y-zirconia.

ONF Powder		TZ8Y Powder	
Element	wt %	Compound	wt %
C	0.16	Y <sub>2</sub> O <sub>3</sub>	13.26
O	0.9	Al <sub>2</sub> O <sub>3</sub>	<0.005
S	0.003	SiO <sub>2</sub>	0.006
Al	0.2	Fe <sub>2</sub> O <sub>3</sub>	<0.002
Si	0.021	Na <sub>2</sub> O	0.057
Cl	0.005	ZrO <sub>2</sub>	86.67
Ti	0.046		
Mn	0.0059		
Fe	0.22		
Co	0.068		
Ni	98.4*		

\* Excluding oxygen, the nickel balance becomes 99.3%.

For comparison purposes, the physical, elastic and mechanical properties typical of nickel and cubic stabilized zirconia are listed in Tables 3.3 and 3.4. The properties for nickel are those of commercial grade nickel 200, containing comparable impurity levels.

## **3.2 Composite Fabrication**

The elemental materials as well as the composite grades are prepared using the same processing method to ensure consistency in fabrication. This section describes the tape casting formulation development, the tape casting procedure, tape characteristics, laminating and burnout procedure, and consolidation method.

### **3.2.1 Tape Casting Development**

Among the various powder processing techniques available to produce composite materials and FGMs, tape casting was selected on the basis of equipment availability, group expertise, slurry and tape characteristics (uniformity, powder dispersion, and reproducibility), composite geometry control, and low composite contamination (controlled by the binder system). Tape casting is the first step in fabricating the M/C composites. The formulation and procedure developed for tape casting of this material system are described.

In developing slurry formulations for new powders much can be applied from existing formulas, such as those developed for alumina powders (e.g. Williams, 1976). Some useful parameters can be drawn from existing formulations, namely dispersant level (relative to the powder volume), solids loading (i.e. the powder to organic ratio in

**Table 3.3:** Physical/elastic properties of commercial nickel and cubic stabilized zirconia.

Material	Density (g/cm <sup>3</sup> ) [25°C]	Melting T (°C)	CTE (10 <sup>-6</sup> /°C) [25-100°C]	E (GPa) [25°C]	Poisson's Ratio
Nickel	8.9	1453	13.3	207	0.31
Zirconia	6	2500	10	233	0.32

**Table 3.4:** Room temperature mechanical properties of annealed Nickel 200 and cubic stabilized zirconia (TZ8Y).

Material	0.2% YS (MPa)	UTS (MPa)	Elongation (%)	Flexure (MPa)	DPH 10kg (kg/mm <sup>2</sup> )	K <sub>IC</sub> (MPa m <sup>1/2</sup> )
Nickel	148	462	47		90	50-100
Zirconia		144		300	1250	1.5

Sources: Betteridge, 1984; CRC Handbook, 1985-1986; Tosoh Corporation.

volume proportions), binder / plasticizers (B/P) ratio, plasticizer-1 / plasticizer-2 ratio (P1/P2), and solvent level (as a volume fraction of slurry ingredients). In general, a solids loading of 55%, B/P ratio about 1/1 to 1/2, and  $P1/P2 \approx 1$  provides a useful guide to initial formulation development. Dispersant and solvent levels depend strongly on powder characteristics but in the case of the alumina slurry studied by Plucknett et al. (1994), 7 vol% dispersant and 55 vol% solvent was found to be optimum.

Since powder size, morphology, and interactions affect slurry characteristics, some scientific as well as trial and error approaches were implemented to develop tape casting strategies. Acceptable tapes are homogenous and free of cracks, open pores, and agglomerates. Initial slurry formulations were developed for the metal and ceramic powders separately. Commonly used organic ingredients were selected for these formulations. Composite slurry formulations simply use a volume based linear rule of mixtures of these pure component formulations. The only significant slurry alteration required for the composite slurries was a reduction in solvent level of about 10% compared to levels required for single component slurries. The most likely reason for this is the improved packing efficiency of bimodal powder distributions.

### 3.2.1.1 TZ8Y-Zirconia Slurry Development

Zirconia slurry development was first attempted on an available stock of Tosoh zirconia (TZ0) having an average particle size of  $0.25 \mu\text{m}$  and a BET of  $14 \text{ m}^2/\text{g}$ . The first step in formulation development is determining an optimum dispersant level, corresponding to a minimum slurry viscosity. Studies performed by Plucknett et al.

(1994) on alumina/TZO slurries of fine particle size (0.25 to 0.3  $\mu\text{m}$ ) revealed a viscosity-dispersant minimum corresponding to a level of about 7 vol% phosphate ester (PE). These tests were performed on slurries containing ceramic powder with PE and solvent (TCE) with solids loading of 40 and 45 vol%. For the current study, development began with TZO using a solids loading of 30 to 35 vol%. Slurries were ultra-sonicated to break down TZO agglomerates. The results were somewhat inconclusive in that a minimum viscosity was not achieved upon dispersant additions greater than 12% (compare Figures 3.2 and 2.3). PE seems very effective as additions in the order of 1 vol% were required to liquify the solvent powder mixture. To circumvent additional testing, a dispersant level of 7 vol% PE was implemented (based on work by Plucknett et al., 1994).

Estimating organic requirements for the slurry began with the basic guidelines previously indicated. The first alteration to this formulation was the solvent requirement. Essentially, levels of about 68%, up from the 55% suggested, were necessary to create a slurry of acceptable consistency. Early tapes contained numerous macroscopic agglomerates and drying cracks. The contents of these agglomerates were not investigated; instead, their prevention was given priority. Slurries containing 7 and 10 vol% PE resulted in identical tape characteristics, indicating that the dispersant level was not the problem. A subsequent slurry containing a reduced solids loading of 52.5% resulted in fewer agglomerates, many pin holes and drying cracks. In attempts to eliminate agglomeration, improve tape flexibility (to prevent crack development while drying and subsequent handling) and reduce solvent requirements, the B/P level was

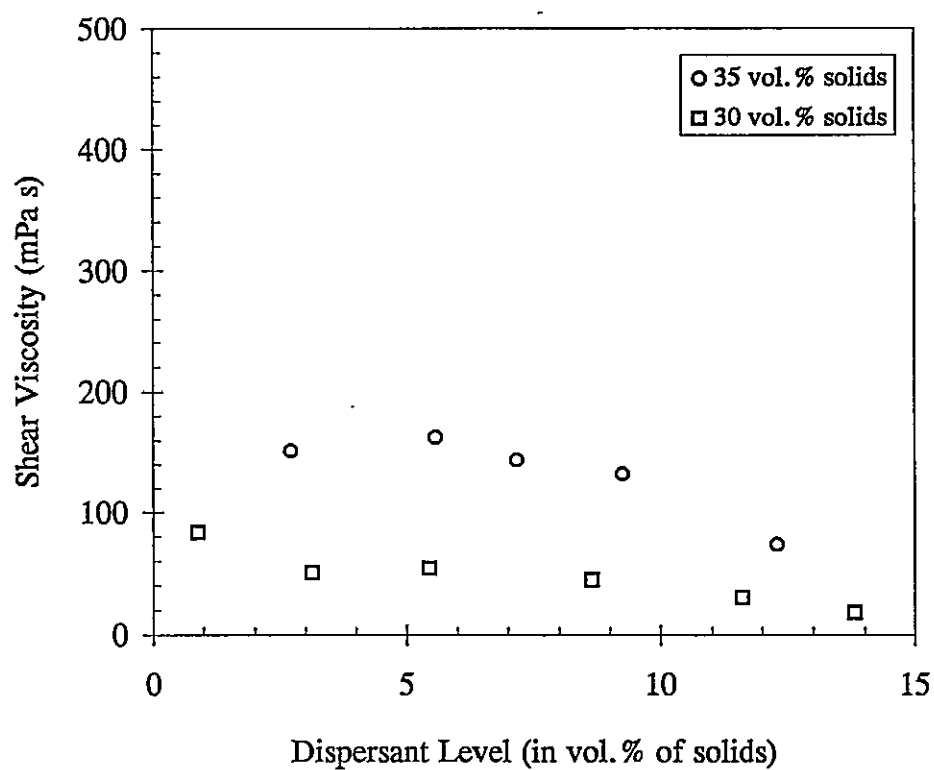


**Figure 3.2:** The shear viscosity-dispersant dependence obtained for slurries containing zirconia powder (TZO), phosphate ester and trichloroethylene.

lowered from 0.72 to 0.55, while maintaining 52.5% solids loading. This alteration was successful in all aspects except in reducing solvent levels.

Following arrival of the powder selected for use in this study (TZ8Y), small changes to the formula were necessary to account for the different powder characteristics (smaller average size ( $0.15 \mu\text{m}$ ) and higher BET ( $15.7 \text{ m}^2/\text{g}$ )). The final formulation for TZ8Y powder is listed in Table 3.5 with the parameters: 7% dispersant (by solids volume), 66% solvent, a solids loading 52.5%,  $B/P=0.5$  and  $P1/P2=1$ .

### 3.2.1.2 ONF Nickel Slurry Development

The formulation for ONF nickel, having a powder size of  $1.9 \mu\text{m}$  and BET of  $4 \text{ m}^2/\text{g}$  was developed using the same approach described for TZ8Y. To minimize time in development, nickel dispersant levels were not optimized. Since this powder is much coarser than TZ8Y, it is expected that less dispersant will be necessary. A level of 5 vol% PE was found successful. Preliminary casts exhibited very high viscosities with the low solvent level. About 68% solvent was considered necessary at this stage. Early casts showed no agglomerates and no cracks, but many pin holes (suggesting a degassing problem). Pin hole porosity was alleviated by a vacuum degassing the slurry prior to casting. These tapes were very flexible but weak and pliable, suggesting that  $B/P$  was too low. Increasing  $B/P$  from 0.72 to 0.9 improved tape characteristics. With the increased binder content, a higher solvent level (72%) was necessary to reduce slurry viscosity and prevent tape adherence to the glass casting substrate. The final ONF nickel formulation is listed in Table 3.5.

**Table 3.5:** Slurry formulations developed for TZ8Y-zirconia and ONF-nickel powders.

Material	TZ8Y Formula		ONF Formula	
	vol %	wt %	vol %	wt %
Powder	17.9	51.7	15.6	57.0
TCE+ethanol (72:28)	66.0	40.1	71.7	37.4
Phosphate ester	1.2	0.6	0.8	0.3
Poly(vinyl butryal)	4.9	2.5	5.6	2.5
Poly(ethylene glycol)	5.0	2.7	3.2	1.5
Diocetyl phthalate	5.0	2.4	3.2	1.3

### 3.2.1.3 Tape Casting Procedure

Slurries were all prepared in high density polyethylene containers. Slurries occupied at least 50% of the container volume. Milling and mixing were performed using ultrasonically clean zirconia milling balls (5 mm in diameter) at a rate of approximately 70 rpm. The volume of balls used was roughly equivalent to the powder volume in the slurry. Slurry measurements were all made by weight. A standard tape casting procedure was developed for all composite grades.

First the powders are dispersed in an azeotropic solvent with dispersant by ball milling for a period of 24 hours. Metal and ceramic powders are dispersed separately. For composite slurries a carefully measured quantity of TZ8Y slurry is added to the nickel slurry following the milling cycle. The dispersed TZ8Y batch will have been initially prepared in excess (about 10%) of that required for the given composite grade. This accounts for slurry waste due to the container and ball entrapment. Prior to TZ8Y slurry transfer, the suspension is continuously agitated to avoid sedimentation which would alter the composite slurry composition. The slurry transfer is not performed in the reverse order (nickel slurry added to TZ8Y) since much nickel slurry is lost to its container. Once combined, the composite slurry is mixed with ball milling for a period of about 1 hour. The viscosity of the slurry in this condition is too low to prevent sedimentation. As a result as soon as mixing is arrested, the white TZ8Y begins to float up. Therefore it is unnecessary to mix the slurry longer than 1 hour at this stage.

The binder and plasticizers are then added and the slurry is mixed for an additional 6 hours. Comparisons were made between TZ8Y slurries mixed for 1, 4 and

16 hours by examining the tapes following burnout (see Figure 3.3). One hour mixing does not provide sufficient mixing. Large scale porosity is seen throughout the tape. Mixing for 4 to 16 hours provides much better mixing. Comparing 4 hours with 16 hours suggests that around 4 hours is optimum. A mixing period of 6 hours was selected as a safe guard to ensure sufficient mixing as well as for convenience.

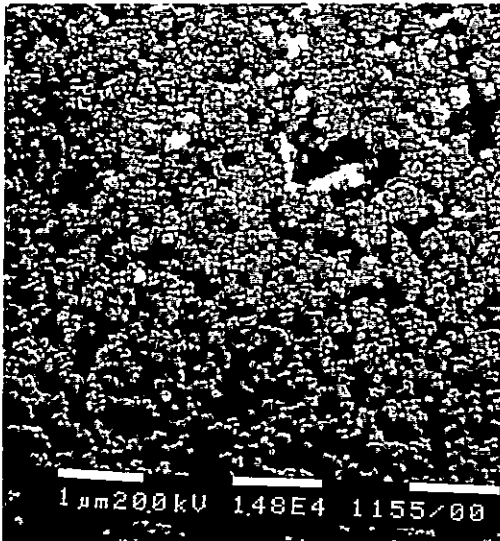
The slurry is then transferred to a cylindrical brass container suitable for controlling the slurry flow into the tape caster reservoir. The slurry is transferred to this container without the zirconia balls. The balls often trap gas and agglomerates from the slurry. The slurry is then degassed using a vacuum pump control set to -150 mm Hg pressure. The container is periodically swirled to help free any trapped gas within the slurry. Degassing is considered complete once no bubbles remain on the slurry surface. Degassing treatments were performed for 2 to 4 minutes.

The tape casting unit is cleaned and re-assembled prior to each cast. Since large slurry batches are prepared to produce sufficient material for property evaluation, three or four tape casting runs are required from each batch. While the tape caster is being cleaned and re-assembled, the contained slurry is left standing. Due to the adequate slurry consistency, no noticeable sedimentation results from standing. The tape casting unit is assembled with two blades, the front blade typically 50  $\mu\text{m}$  higher than the trailing blade. This produces a smooth even tape. The leading and trailing blade heights from the glass casting substrate are listed with an accuracy of about 5  $\mu\text{m}$ , in Table 3.6.

The slurry is poured into the doctor blade reservoir just prior to tape casting. The caster is hydraulically driven at a rate of 1 cm/s and the slurry is cast onto heat treated



(a)



(b)



(c)

**Figure 3.3:** Green tapes from slurries milled for 24 hours and mixed with organics for: (a) 1 hour, (b) 4 hours, and (c) 16 hours. Images from constrained surface.

**Table 3.6:** Characteristics of tapes and laminates.

Composite Grade (vol %)	Blade Heights ( $\mu\text{m}$ )	Tape Thickness ( $\mu\text{m}$ )	Tape Porosity (vol %)	Laminate Porosity (vol %)
100% Ni	440/400	150-170	29	9
75:25	440/400	140-150	15	5
50:50	450/400	130-150	6	3
25:75	340/300	110-130	9	5
100% TZ8Y	400/350	125	14	10

glass sheets. Tapes are allowed to dry overnight under a fume hood. The tapes are cut into 25 cm strips, peeled from the glass substrate and stored for later use.

#### 3.2.1.4 Tape Characteristics

Using the technique and formulations developed for tape casting, consistent, reproducible tapes are achieved. Tapes are free of agglomerates, cracks and vapour holes. Tape shrinkage and porosity development accompanies solvent evaporation during tape drying. Slurries and the dried tapes exhibit characteristic color depending on the composite grade level. Composite slurries produce distinct color inhomogeneity in sections of the cast tapes.

The thickness of the cast tapes depends on the slurry viscosity, blade height, and casting rate. Shrinkage and porosity development accompanies solvent evaporation. Since the tape is constrained to a glass substrate, only through thickness shrinkage is observed. Tape density determination identifies porosity while the difference between blade height and final tape thickness can be used to quantify shrinkage. This data is compared in Table 3.6.

The desired final thickness for consolidated samples for use in property measurement was about 3 mm. Since axial hot pressing is employed on green bodies of about 50% density, tape laminates in the order of 6 mm are necessary. About 50 to 60 tapes are needed per sample to achieve this thickness. It seems reasonable to create thicker tapes to minimize processing time. Casting attempts with a trailing blade height of 950  $\mu\text{m}$  resulted in TZ8Y tapes of 330  $\mu\text{m}$  and 50:50 composite tapes of 280  $\mu\text{m}$

thickness. However, large drying cracks developed in these tapes. To avoid procedure modification, thin tapes were accepted.

A characteristic macroscopic color appears in tapes, laminates, and consolidated specimens depending only on composition. TZ8Y powder is white producing white tapes and nickel powder is greyish-brown due to surface oxide resulting in a light brown tape. Composite tapes containing 25% Ni appear dark charcoal grey in color. Composite tapes of 50% Ni appear as a color mixture of the 25% Ni and 100% Ni grades, while 75% Ni tapes appear slightly darker than the 100% Ni tapes. The 25% Ni composites remained dark following burnout and consolidation. Composites with 50% or more nickel resume a more metallic appearance following consolidation. Optical microscopy indicates that the zirconia phase is a very dark constituent in the composites.

As a result of the different powder sizes and densities of nickel and TZ8Y powders, inhomogeneity exists during slurry mixing. The surface of composite slurries typically reveal white streaks, representing TZ8Y separation. Increased sedimentation was not observed while the slurry was left standing. The inhomogeneity likely results as a consequence of the pseudoplastic slurry characteristics. Slurry separation is also observed during the transfer of slurry to the tape casting reservoir and white swirls reside on the slurry surface in the reservoir. Upon casting, the slurry rolls over and under the casting blade. The first stretch of tape consumes most of the inhomogeneity on its glass side. At the trail of the tape, once the first reservoir empties, a final white streak crosses the tape. Since the volume corresponding to the white streaks is very low in comparison to the slurry volume, it is assumed (based on microscopic evaluation) that the

homogeneous sections contain the nominal metal and ceramic fractions.

### 3.2.1.5 Tape Lamination

Two sizes of disk specimens were fabricated in this study, 25.4 mm diameter for preliminary characterization and 50.8 mm for property assessment. Tapes were cut with the appropriate size tool steel punch. Tape fragments are removed from the tape surfaces and edges. Tapes without blemishes and inhomogeneities are stacked with a random orientation with respects to casting direction in a thermal compression (laminating) die. Stainless steel die construction is used for both diameters but the 50.8 mm diameter includes a brass die insert to avoid galling of the die and plungers. Between the plungers and the tapes are 3 mm teflon sheets followed by filter paper to aid in the removal of the teflon from the laminate.

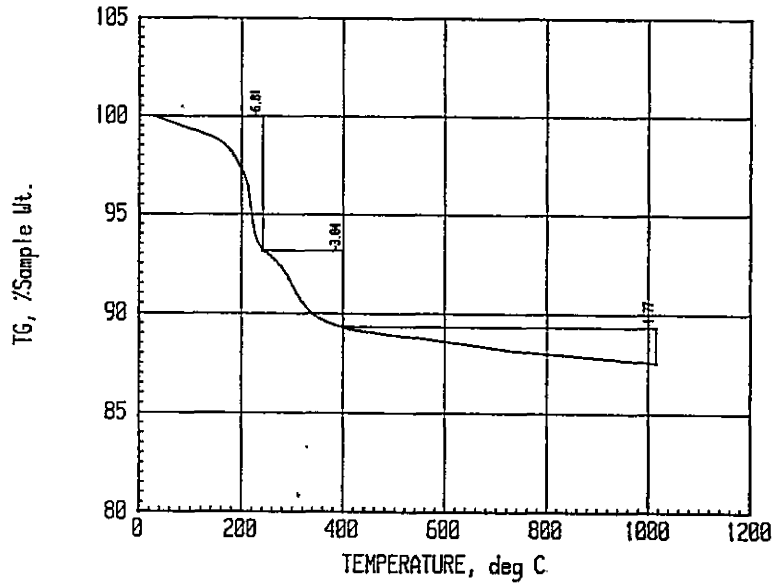
The assembled unit is heated to about 120°C in air (heating times of 30 minutes for the 25.4 mm die and 3-4 hours for the 50.8 mm die). The heated unit is removed from the furnace, exposed to a vacuum pump set to -450 mm Hg, and loaded in axial compression (40 MPa for 25.3 mm and 20 MPa for 50.8 mm specimens) until the die is warm to the touch (about 10 minutes for 25.4 mm and 30 minutes for 50.8 mm specimens). The longer thermal compression time for the large specimens enables the lower laminating pressure. Proper lamination ensures laminate integrity during organic burnout. As a consequence of lamination, tape porosity is reduced as is indicated in Table 3.6.

### 3.2.2 Organic Burnout

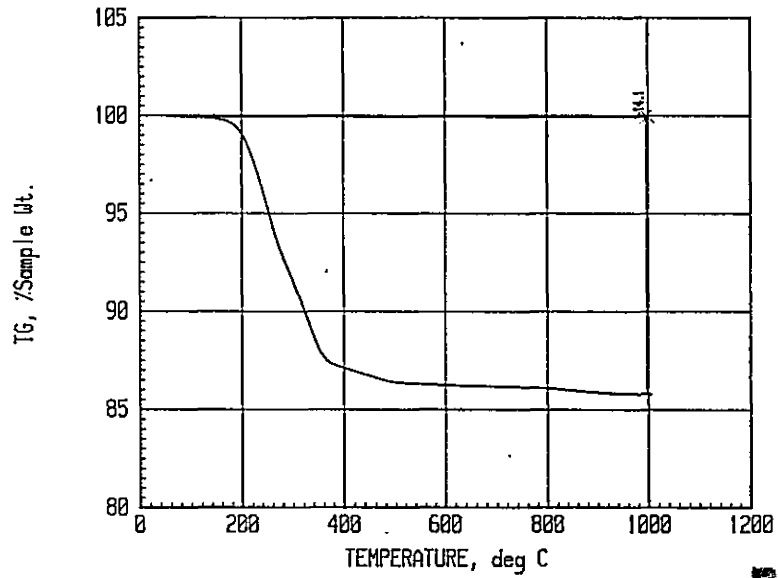
Developing a burnout procedure for the laminates was time consuming and laborious. The goal of the burnout treatment is to remove all of the organics and provide sufficient strength to the laminates through diffuse interparticle necks while maintaining the structural integrity of the laminate. Factors such as the characteristics of the organics, burnout atmosphere, heating-rate, and specimen geometry all influence burnout characteristics. The initial focus was on the burnout characteristics of nickel and TZ8Y tapes. Through scientific and trial and error experiments, an appropriate procedure was developed.

#### 3.2.2.1 Burnout in Argon

It was originally desired to burnout in an inert atmosphere to prevent oxidation of the nickel phase, hence high purity argon was selected. Thermal gravimetric analyses (TGA), performed to identify the burnout characteristics (weight loss versus temperature at a constant heating rate) of nickel and TZ8Y tapes are shown in Figure 3.4. The burnout rate for TZ8Y is roughly constant at  $-0.4 \text{ wt\%/min}$  over the temperature range of  $200^\circ\text{C}$  to  $360^\circ\text{C}$ . Nickel tapes exhibit two burnout extremities,  $-0.95 \text{ wt\%/min}$  from  $220^\circ\text{C}$  to  $240^\circ\text{C}$  and  $-0.25 \text{ wt\%/min}$  from  $280^\circ\text{C}$  and  $320^\circ\text{C}$ . The higher severity during Ni burnout may be due to a catalytic effect of nickel on organic pyrolysis. Since laminate integrity is highly dependent on burnout rate these high rate temperature regimes are of concern. Due to the lower molecular weight of the plasticizers they pyrolyze at a lower temperature than the binder. In the case of nickel burnout it is seems necessary



(a)



(b)

Figure 3.4: Thermal gravimetric analysis of (a) nickel, (b) TZ8Y tapes treated in flowing argon. Heating rate of 5°C/minute.

to completely burnout the plasticizers, at a low pyrolysis rate, before pyrolyzing the binder. Subsequent binder pyrolysis must also be achieved at a low burnout rate. More detailed TGA analyses showed a small weight decrease upon heating above 700°C, corresponding to the pyrolysis of phosphate ester.

Organic removal is essentially complete by 500°C. Ceramic laminates are typically heated to about 1000°C to provide some handling strength. Nickel containing laminates should not be heated to this temperature during burnout since densification would result. Nickel-zirconia composite burnout treatments with a heating rate of 1°C/hour to 500°C followed by a 5 hour dwell have been reported (Takemura et al., 1993).

Burnout of TZ8Y in argon is easily accomplished using treatment #1 of Figure 3.5. The resulting laminate is black in color due to residual carbon ash. The laminate exhibits sufficient strength to enable handling and shows insignificant shrinkage following burnout. Vacuum hot pressing results in dense black TZ8Y. It was found that following burnout, a heat treatment in air at 500°C removes this color with a corresponding weight loss of about 1.1 wt%.

Burnout attempts using treatment #1 were unsuccessful on nickel laminates. Using the TGA for nickel tapes and trial and error burnout runs, treatment #8 in Figure 3.5 was established which enables burnout of 25.4 mm diameter by 3.5 mm thick nickel laminates. The resulting specimens are covered with a black powder-like ash (especially on the periphery) and are relatively weak. Specimen dilation is negligible.

Upon consolidation of nickel and nickel-zirconia composites poor density is

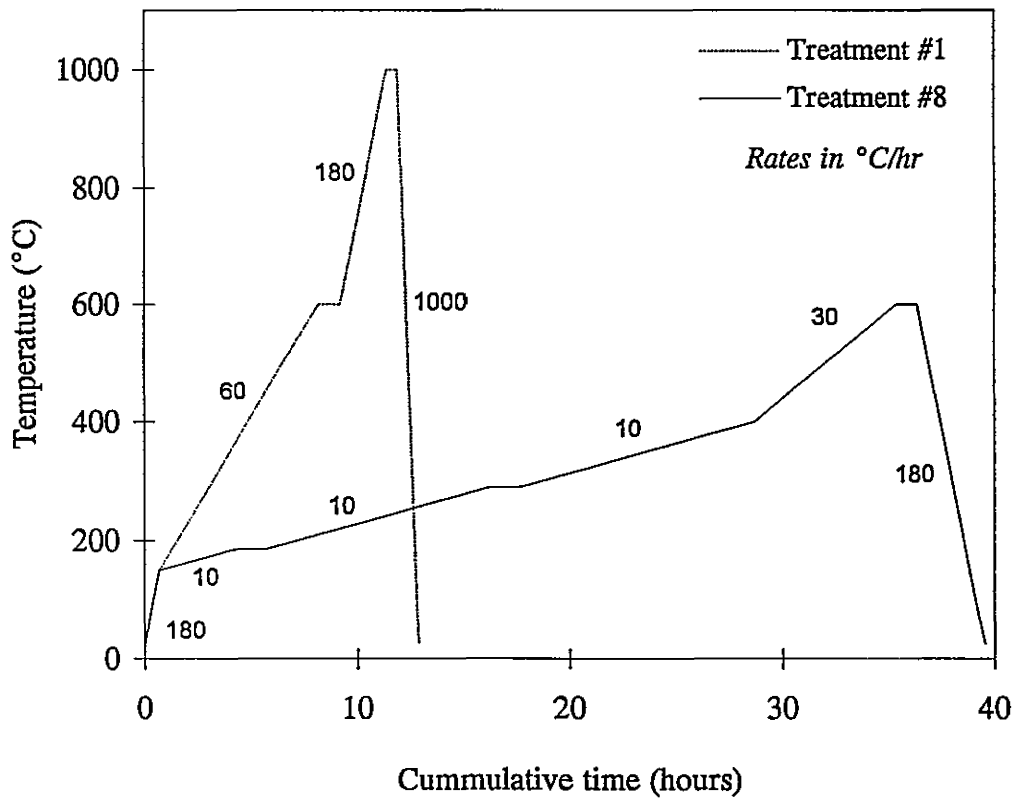


Figure 3.5: Laminate burnout treatments in flowing argon gas.

achieved ( $\approx 95\%$  dense) if carbon is present. The carbon likely reacts with either the oxygen in the green laminate or with the surface oxide on nickel producing CO/CO<sub>2</sub> gas in the densifying laminate. Carbon also affects the properties of nickel (e.g. increases strength but decreases ductility). Carbides may also form upon cooling from processing. It was thus desired to ensure low carbon levels in the consolidated materials.

The source of carbon in nickel may be impurities in the powder, residual ash from burnout, or contamination from the graphite hot pressing die. Table 3.7 contains the carbon levels following various stages of processing. The residual carbon resulting from burnout in argon is  $\approx 1.7$  wt% in Ni and  $\approx 1.1$  wt% in TZ8Y. Nickel burnout in argon followed by a heat treatment in H<sub>2</sub> at 700°C and 1200°C decarburizes the nickel, most likely via the formation of CH<sub>4</sub>. Similar treatments on TZ8Y did not decarburize. Since the TZ8Y may transfer carbon to the nickel in subsequent processing, decarburization in H<sub>2</sub> was deemed inappropriate. The alternative is burnout in air which eliminates the carbon from both nickel and TZ8Y.

### 3.2.2.2 Burnout in Air

Figure 3.6 illustrates the TGA results for TZ8Y and nickel laminates during burnout in air. Burnout of TZ8Y shows similar weight loss behaviour in both argon and air. Nickel tapes in air show an initial weight loss due to organic pyrolysis and combustion which is countered by a weight gain due to nickel oxidation at higher temperatures. Most of the organics are removed at 360°C, beyond which the laminate oxidizes appreciably. The initial rate of weight loss is  $\approx -0.42$  wt%/min which is

**Table 3.7:** Carbon, oxygen and sulfur levels in nickel at various stages of processing.

Specimen Condition	Sample Number	Element Level (wt%)		
		C	O	S
Powder	-	0.16	0.8	0.003
BO-Ar	37	1.70	0.25	
BO-Ar, HP vac (900°C)	7	1.50	0.1	
BO-Ar, HP-3.5%H <sub>2</sub> (1300°C)	14	1.40	0.09	
BO-Ar, R-H <sub>2</sub> (700°C)	37	0.04	0.23	
BO-Ar, R-H <sub>2</sub> (700°C), HP-5%H <sub>2</sub> (1200°C)	57	0.02	0.1	
BO-Ar, PS-H <sub>2</sub> (1200°C)	37	<0.01	0.14	
BO-air, PS-H <sub>2</sub> (1200°C)	47	<0.01	0.09	
BO-air, R-H <sub>2</sub> (450°C), HP-vac (950°C)	B12	0.01	0.6*	0.003

\* Estimated from oxide volume

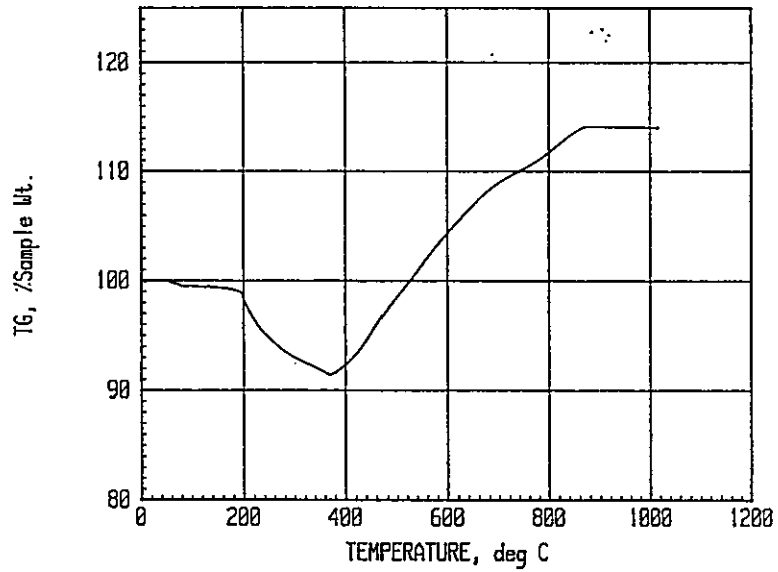
Key:

BO-burnout

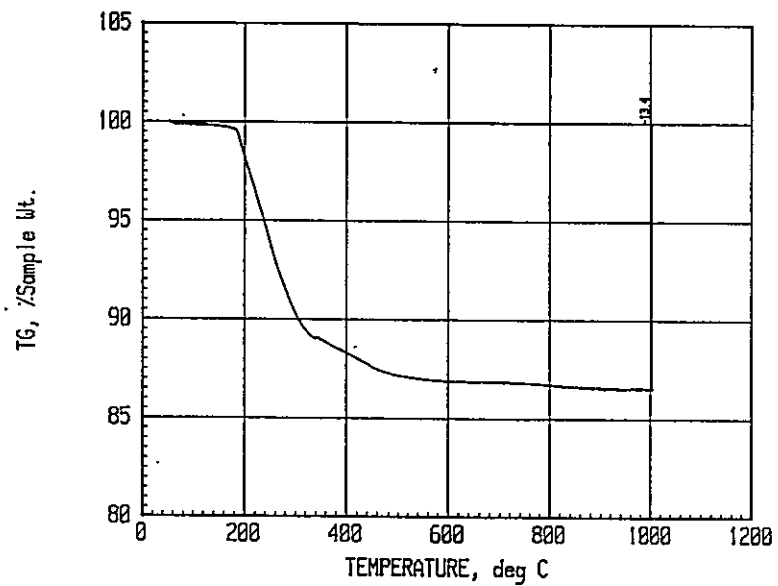
R-reduction

HP-hot pressed

PS-pressureless sintered



(a)



(b)

**Figure 3.6:** Thermal gravimetric analysis of (a) nickel, (b) TZ8Y tapes during treatments in flowing air. Heating rate of 5°C/minute.

comparable to that observed for TZ8Y.

Burnout treatment #8 in air was successful for laminates of TZ8Y and small laminates of nickel (25.4 mm diameter by 4.2 mm thick). The resulting TZ8Y is white but has low strength due to the low firing temperature. The nickel appears dark with oxide but clean of carbon ash. Increasing the specimen thickness and diameter required further treatment alterations to avoid crack development in nickel bearing laminates. Changes focused on the burnout extremities observed in argon derived TGAs. Burnout treatment #14 illustrated in Figure 3.7 was successful for specimens of 50.8 mm diameter by 5.5 mm thickness. Fine surface edge cracks result on composite laminates with this technique; however, such cracks are healed by hot pressing.

As a result of the burnout treatment in air, the metallic phase oxidizes appreciably. Table 3.8 indicates the influence of oxygen on these materials. It appears from the apparent density data that nickel oxidation reaches a limit in the composites when the density reaches about 72% of theoretical in the laminates. For this reason composites containing lower nickel compositions exhibit higher levels of nickel oxidation. After considering thermodynamic data and testing reduction kinetics (see Figure 3.8), it was found that nickel oxide reduction could be accomplished in flowing Ar-5% $H_2$  at 450°C. These conditions impose a reasonably low reduction rate at a low enough temperature to prevent substantial shrinkage. Higher reduction rates and increased shrinkage rates contribute to specimen cracking. For the large specimen geometry (50 mm diameter x 5.5 mm) about 12 hours is necessary to fully reduce the nickel in the composites. Pure nickel laminates continued to show small weight reduction after 12

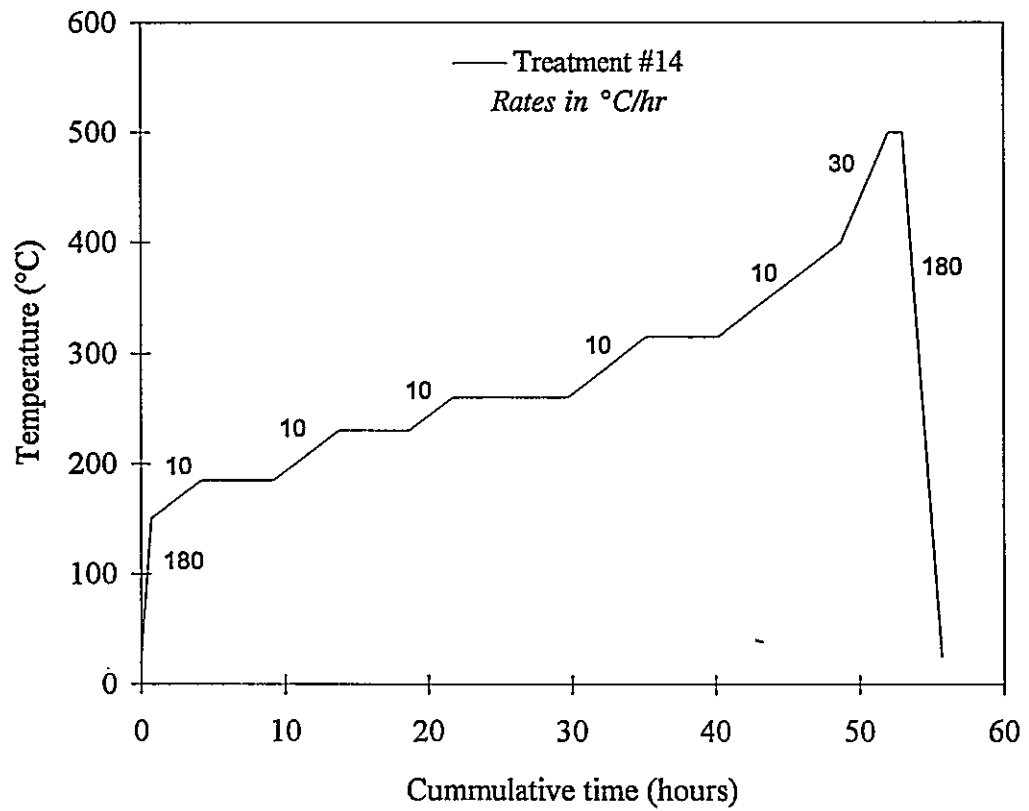


**Figure 3.7:** Burnout treatment of large geometry, nickel laminates in air.

**Table 3.8:** Oxidation, dilation, and density data of nickel laminates following burnout and reduction.

Composite Grade (vol %)	Wt% of Ni as Oxygen in BO lam.	Vol% of Ni as NiO in BO lam.	Apparent Density		Specimen Dilation	
			Burnout (% theo)	Reduction (% theo)	Burnout (vol %)	Reduction (vol %)
100% Ni	12.6	66	72	54	-6.0	-2.6
75:25	13.0	80	72	54	-4.5	2.1
50:50	11.2	91	62	51	2.8	-0.3
25:75	6.4	93	52	50	2.7	-1.4
100% TZ8Y	-	-	48	48	0.0*	0.0

\* 100% TZ8Y is typically treated to 1000°C during burnout resulting in 1.5 volume % shrinkage

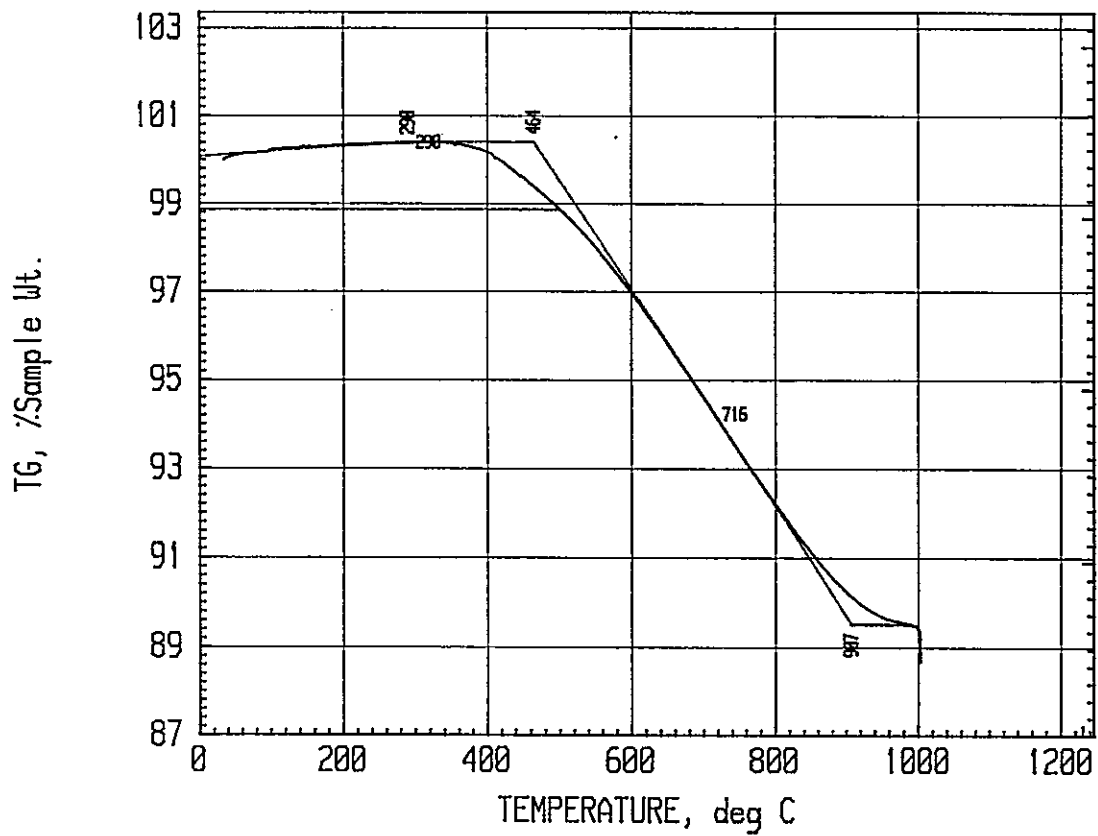


**Figure 3.8:** Reduction of oxidized nickel laminates via thermal treatment in Ar-5% $H_2$  gas. Heating rate of 10°C/minute.

hour treatments. Since the surface of nickel powder will oxidize in air under ambient conditions further nickel reduction was negated. All specimens exhibited very good strength following this treatment.

Due to laminate burnout in air and reduction in hydrogen, specimen dilation occurs as shown in Table 3.8. Burnout results in shrinkage in 100% Ni, 75% Ni and 50% Ni materials, expansion in 25% Ni and negligible changes in TZ8Y. Subsequent reduction results in variable degrees of dilation in nickel containing samples with magnitudes of about half those achieved during burnout. After accounting for specimen dilation, the green densities of the reduced composites are listed in Table 3.8.

The differences in dilation between grades suggests a problem in the fabrication of nonuniform composite laminates. The burnout of a five layer 25.4 mm diameter discontinuous FGM was attempted (containing  $\approx 0.3$  mm interlayers of 25, 50, and 75% Ni). The result was delamination in the 25% Ni level with the TZ8Y layer remaining planar and the nickel rich layers conforming to a concave shape toward the 100% Ni side. Large cracks accommodated this concave shape. Successful FGMs were achieved only by stacking individually processed green laminates or bi-layers in the hot press. This, however, introduces contamination between layers.

### 3.2.3 Laminate Consolidation

Three techniques for specimen densification are available at McMaster: pressureless sintering (PS), hot isostatic pressing (HIP), and hot pressing (HP). The atmosphere and other contamination sources are of concern in all these techniques. PS

is the simplest consolidation method to perform. However, it requires high temperatures, involves 3 dimensional shrinkage, and results in poor final density (especially in composites). HIP is very effective yet it requires the use of encapsulation and results in three dimensional contraction. HP relies on uniaxial shrinkage, via the application of uniaxial pressure, and provides good densification. The uniaxial shrinkage sets the specimen's transverse dimensions to that of the die wall. This is advantageous for designing specimens for mechanical testing. HP was selected based on this benefit, its ability to produce high densities at low temperatures, and its relative ease of implementation. The mechanisms of densification are outlined in the Section 2.4.

At McMaster, HP is facilitated in a vacuum furnace within a graphite die. Due to the chamber design, the vacuum is limited to about  $10^{-1}$  torr. Nonexplosive backfill gas is permitted in this system. Backfills using Ar-5% $H_2$  were shown to have little effect due to the stagnant flow conditions. Due to the large quantities of graphite within the furnace, thermodynamic calculations indicate that a CO/ $CO_2$  reducing atmosphere will be created while under vacuum. However, consolidation experiments indicate that heavily oxidized nickel samples show negligible weight loss (about 0.5%) while previously reduced nickel laminates showed a gain of about 0.3 wt% during the course of HP treatments. All hot pressing runs for specimen preparation were performed under vacuum. To avoid nickel-graphite reactions, boron nitride was coated on all parts as well as the composites to prevent direct contact.

Tests were performed to identify hot pressing conditions which would be suitable for all laminates. Experiments focused on the sintering performance of 100% TZ8Y

laminates, using density as a performance indicator. From the sintering dilation experiment of Figure 3.1, it is noted that at least 1100°C is necessary to facilitate composite sintering. The upper bound for hot pressing is the melting point of pure nickel, 1455°C. The hot pressing characteristics of TZ8Y is influenced by numerous factors including temperature, time, uniaxial pressure, and axial loading temperature. It is desirable to use the least intensive hot pressing conditions possible. Figure 3.9 is a compilation of the tests performed to optimize these conditions. The optimized conditions drawn from these results is that hot pressing should be performed at 1250°C for 3 hours at 65 MPa pressure with load being applied at a temperature of 1150°C on heating. These conditions ensure greater than 99% dense TZ8Y samples in both small and large geometries. These conditions densify all composite grades to greater than 98% dense.

Difficulties were encountered with hot pressing large diameter specimens of 100% Ni at 1250°C, due to reaction with the environment and the graphite die. Also nickel grain growth at this temperature is very high, possibly trapping porosity within the grains. Since the nickel phase within the composites is constrained from grain growth to the adjacent ceramic, it was considered desirable to fabricate 100% Ni with a fine grain morphology. Tests indicated that hot pressing at 950°C is sufficient to densify nickel to >99% density with negligible grain growth.

### 3.4 Summary

The details in this chapter describe the materials selection process employed, and

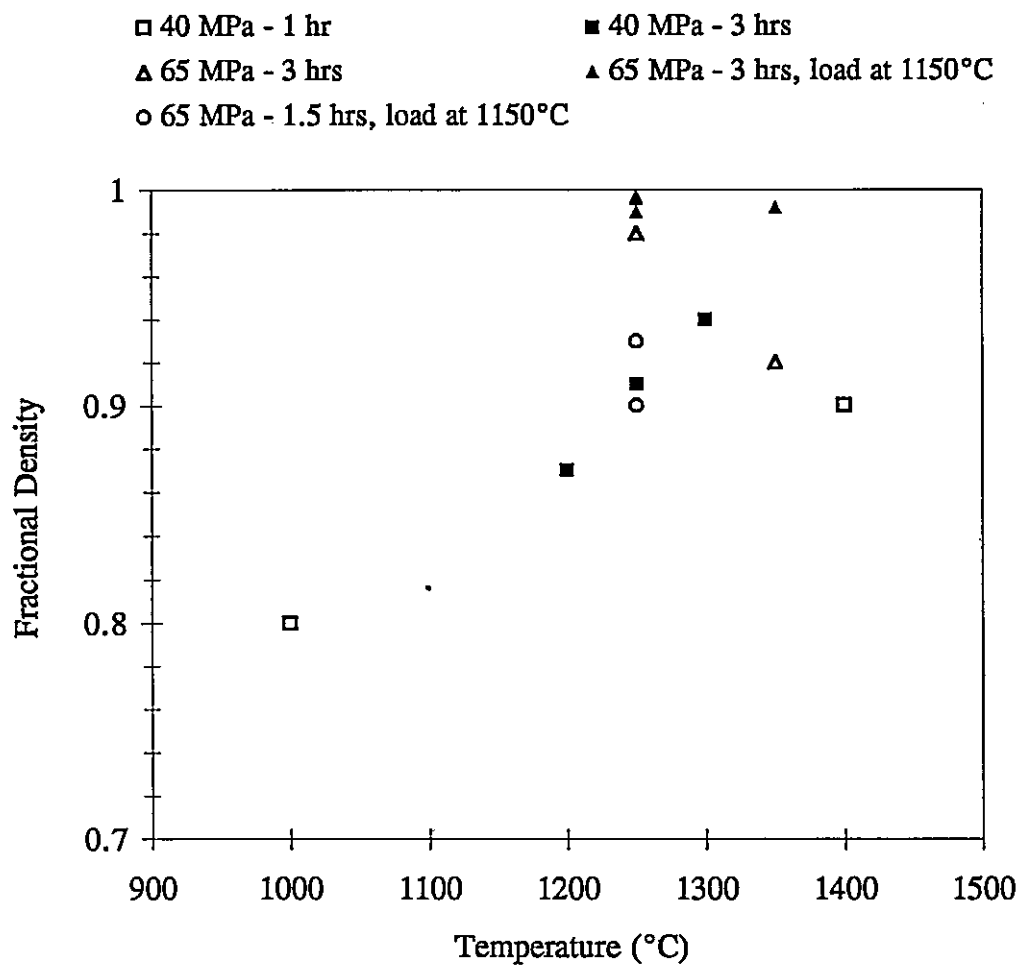


**Figure 3.9:** Effect of hot pressing parameters on the consolidated density of TZ8Y laminates.

the conditions and procedures employed to fabricate materials in this study. Tape casting requires strict compliance to formulation ingredients and procedure. Burnout must be facilitated in air at a controlled heating rate to 500°C which completely removes the tape casting organic but heavily oxidizes the nickel. Reduction of nickel oxide is performed at 450°C in flowing Ar-5%H<sub>2</sub> gas for about 12 hours. Hot pressing (under vacuum) of TZ8Y and composite laminates at 1250°C for 3 hours under 65 MPa axial pressure, applied at 1150°C on heating provides >98% dense materials. Hot pressing of 100% Ni samples at 950°C for 1 hour ensures dense structures with negligible grain growth.

## **CHAPTER 4**

### **EXPERIMENTAL PROCEDURE**

The processing procedure has been described in detail in Chapter 3 and will not be addressed here. This chapter describes the treatments and test procedures employed on fabricated materials. Considerations include heat treatments, specimen preparation for microstructural characterization, and details concerning property evaluation.

#### **4.1 Specimen Heat Treatments**

Heat treatments were performed in alumina tube furnaces. Specimens were buried within zirconia powder in alumina crucibles. The powder provides specimen temperature control and prevents specimen contact with alumina. The gas used for these treatments was either argon or hydrogen having a purity designation of PREP (ie. containing  $\leq 10$  ppm of reactive impurities). Prior to heating, the furnace was purged with high flow rate gas for 1 hour. Heat treatments employed a continuous gas flow at about 2 bubbles per second. The furnace heating rate was controlled to 150°C/hour. Specimen cooling was facilitated by furnace cooling (ie. at zero furnace power).

Nickel specimens were treated at various temperatures and in either argon or hydrogen. Based on this assessment, a standard treatment was established to treat the

nickel and the composites so that acceptable nickel phase behaviour was achieved. Samples were treated in argon at 950°C for 5 hours. This treatment lowers the strength of the nickel yet does not result in significant grain growth or warp the specimen which may occur at higher temperatures. 100% TZ8Y specimens were treated at 1100°C for one hour. This temperature was selected so as to anneal out machining stresses while preventing significant grain growth; however, negligible improvements to flexure properties resulted.

## **4.2 Specimen Microstructure Evaluation**

Specimens were examined via optical, scanning electron, and transmission electron microscopy. Specimen procurement and evaluation techniques are described.

### **4.2.1 Optical Microscopy**

The standard specimen grinding technique was used on sample surfaces (ie. SiC paper of incrementally finer grit). Best polishing was achieved by first using 6  $\mu\text{m}$  diamond lapping for about 1 minute, followed by silica dispersion polishing.

Micrographs were taken using a Leco<sup>®</sup> 2001 image analyzer. The resulting digital images are useful for phase characterization. These images are also of very high magnification for optical sources, hence providing acceptable scale microstructural images.

#### **4.2.2 Scanning Electron Microscopy**

SEM analysis was performed on fracture surfaces. Qualitative compositional analysis, using the EDX system was occasionally performed. Fracture specimens were handled in a careful manner prior to mounting. Specimens were ultrasonically cleaned in acetone, in methanol, and then dried. A silver paste was used to adhere the specimens to the SEM mounting stub. Specimens containing nickel were demagnetized. Specimens containing zirconia were platinum coated to prevent surface charging.

#### **4.2.3 Transmission Electron Microscopy**

Conventional TEM (using the Phillips CM12) and high resolution work (using the FEG JOEL 2010F equipped with EDS) was completed on nickel by Dr. Xiaoguang Ning and on composites by Dr. Wenying Yang. These individuals performed all necessary sample preparation and sample analysis techniques.

### **4.3 Elastic Property Assessment**

Elastic modulus measurements via the pulse-echo technique were performed by Dr. N. D. Patel. Smooth, flat, parallel samples were provided for analysis. The analysis produced the longitudinal and shear pulse transfer times ( $t_L$  and  $t_s$  respectively). The longitudinal and shear velocities are calculated from  $v_L = 2d/t_L$  and  $v_s = 2d/t_s$ , (where  $d$  is specimen thickness) from which Poisson's ratio, and subsequently the Young's Modulus are calculated as:

$$\nu = \frac{v_L^2 - 2v_S^2}{2(v_L^2 - v_S^2)} \quad [4.1]$$

$$E = \frac{8\rho b^2}{t_S^2} (1 + \nu) \quad [4.2]$$

where  $\rho$  is the specimen density. The frequency and wavelength of the pulse used was 10 MHz and  $\approx 5$  nm respectively.

#### 4.4 Thermal Dilatometry

A Theta Industrial dilatometer system was used to produce temperature-dilation profiles for the specimens. Bars of about 25 mm length were used in this testing. Experiments were performed at a heating rate of 3°C/minute to 950°C or 1200°C, followed by dwelling for 1 hour and then cooling at 3°C/minute. To avoid nickel oxidation, tests were performed in flowing argon gas. Cooling dilation represents the behaviour of heat treated material.

#### 4.5 Mechanical Testing

Flexure tests, tensile tests and hardness tests were performed on the materials. The details of these tests and data treatments are described.

##### 4.5.1 Flexure Test

Flexural strength was determined using four point bend testing in accordance to

ASTM C1161. All bars (except 100% nickel specimens) were machined to 1.5 x 2 x 22 mm dimensions. This geometry, the smallest geometry specified in the C1161 Specification, was selected so as to easily fabricate numerous bars and thus perform statistical analysis of the data. Machined specimens were heat treated prior to flexure testing.

A flexure rig consisting of four articulated pins, shown in Figure 4.1, was used. The pins can rotate and translate to accommodate the specimen under flexure. A Lloyd's 6000R testing system was used to load the rig and computer software recorded load and axial dilation. The 1 kN load cell used assumes an error of about  $\pm 5$  N. The Lloyd's, when tested in compression, reveals a system compliance as shown in Figure 4.2. Unfortunately the curve is not linear and the response varies somewhat from test to test. The resulting flexure data was corrected to remove the effects of the system compliance. However, the linear slopes on the flexure plots do not provide accurate modulus values.

An assumption in four point flexure testing is that specimen yielding does not occur. In such cases, the stress profile is linear from tension to compression with zero stress along the centre axis. The standard formula for the strength of a beam in four-point flexure is as follows:

$$S = \frac{3PL}{4w(th)^2} \quad [4.3]$$

where:

P= failure load (N),

L= outer support span (20 mm),

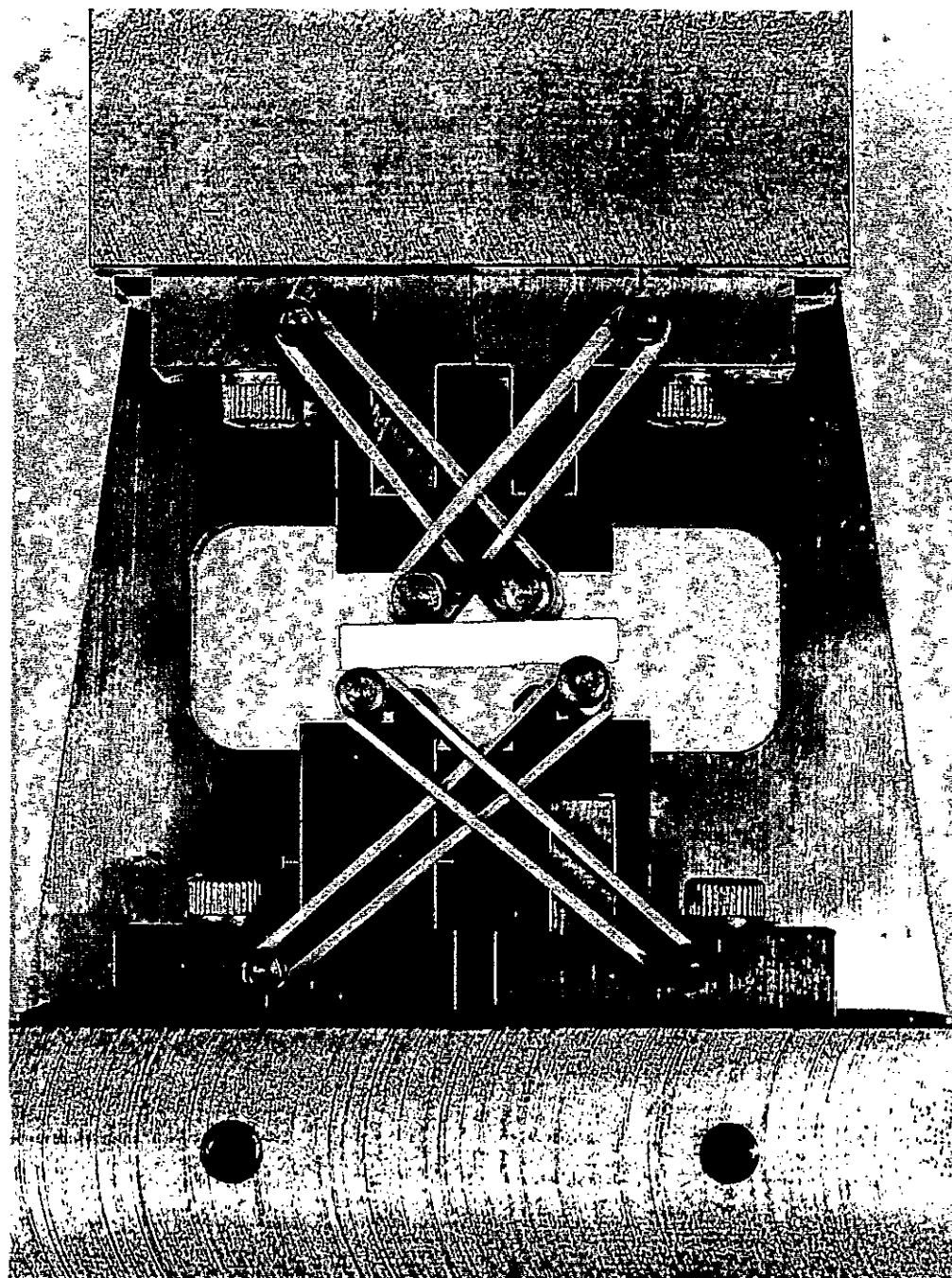


Figure 4.1: Fully articulated four point 1/4-point flexure test rig.

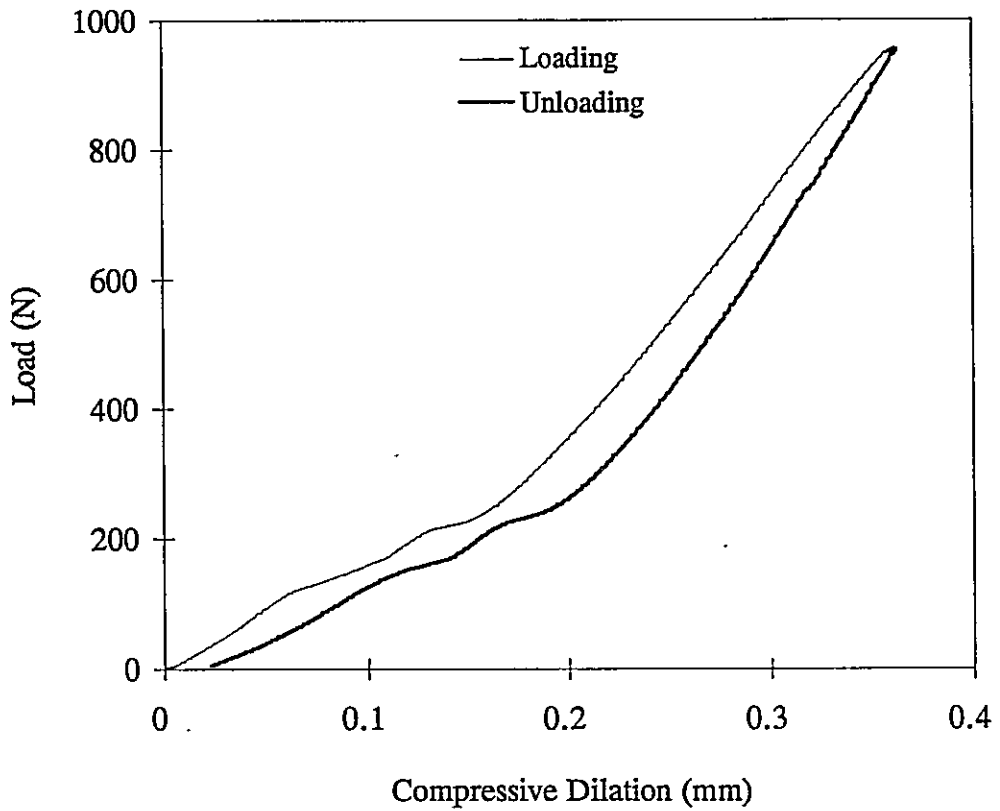


Figure 4.2: System compliance of the Lloyd's materials testing system.

$w$ =specimen width (2 mm), and

$th$ =specimen thickness (1.5 mm).

Equation 4.3 can be used to relate the applied stress at the flexure surface to the applied load for brittle materials. The tensile strain at the flexure surface as a function of the load cell dilation is expressed as:

$$\epsilon = \frac{6(th)}{(L-a)(L+2a)} Y \quad [4.4]$$

where:

$a$ =inner support span (10 mm) and

$Y$ =load cell dilation.

Equations 4.3 and 4.4 were used to compute the flexure stress-flexural strain plots of Figures 5.2-5.4. Note that the stress profiles for 100% Ni samples are only accurate up to the point of specimen yielding. The levels of failure strain experienced by the nickel samples are approximate.

#### 4.5.2 Tensile Test

Nickel specimens, processed by hot pressing at 950°C, were tensile tested. Tensile bars were machined to gauge dimensions of 4 x 2 x 20 mm, with a total specimen length of 35 mm. Load versus extension tests were performed on a MTS-810 with a strain gauge for accurate strain measurement. The error in load measurement is about  $\pm 10$  N.

### 4.5.3 Hardness Test

Vicker's hardness measurements were measured at low loads (15g-microhardness) and at high loads (500g-macrohardness). The distinction between micro- and macro-hardness is based on the scale of the indented surface with respects to the microstructure. Low load indentation can identify the hardness of a select phase within the microstructure. The hardness tester was calibrated to ensure reliable values were attained from both microhardness and macrohardness.

## **CHAPTER 5**

### **RESULTS**

Analyses have been performed to characterize the elemental materials (nickel-grade ONF and zirconia-grade TZ8Y), the uniform Ni/TZ8Y composites and to evaluate the processing technique developed. Microstructural development and thermal, elastic, and mechanical properties have been examined. Fractography is included in support of this characterization. Great efforts have focused on examining nickel behaviour in the consolidated 100% nickel samples. The results are presented here with subsequent discussion in Chapter 6.

#### **5.1 Microstructural Observations**

Microstructural studies relied on optical microscopy, TEM and SEM. The general phase morphology within the composites is described. The results of TEM studies on consolidated nickel, TZ8Y and composites are provided and fractographic images are included.

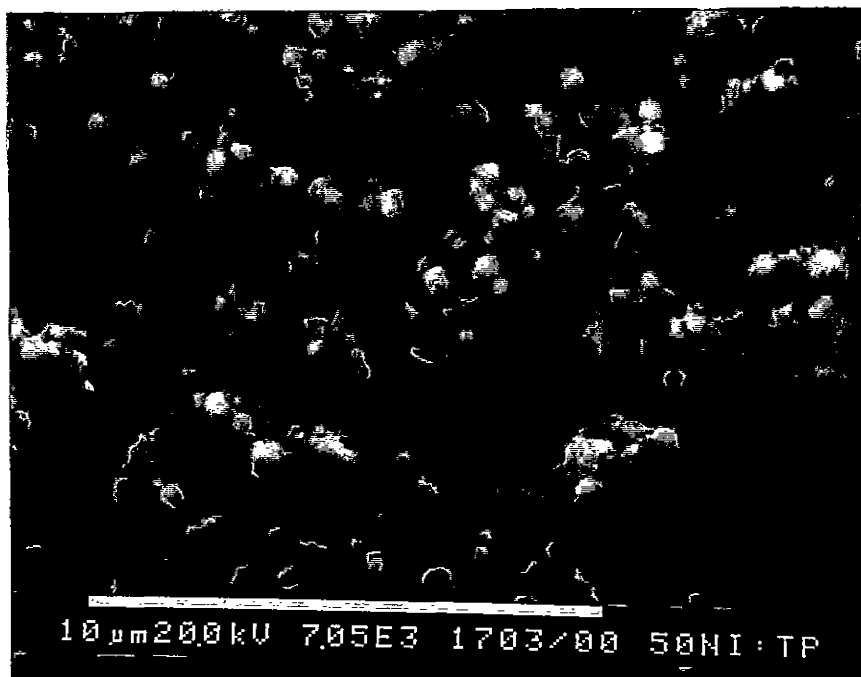
##### **5.1.1 General Phase Morphology**

The top and bottom surfaces of composite tapes following burnout in argon were

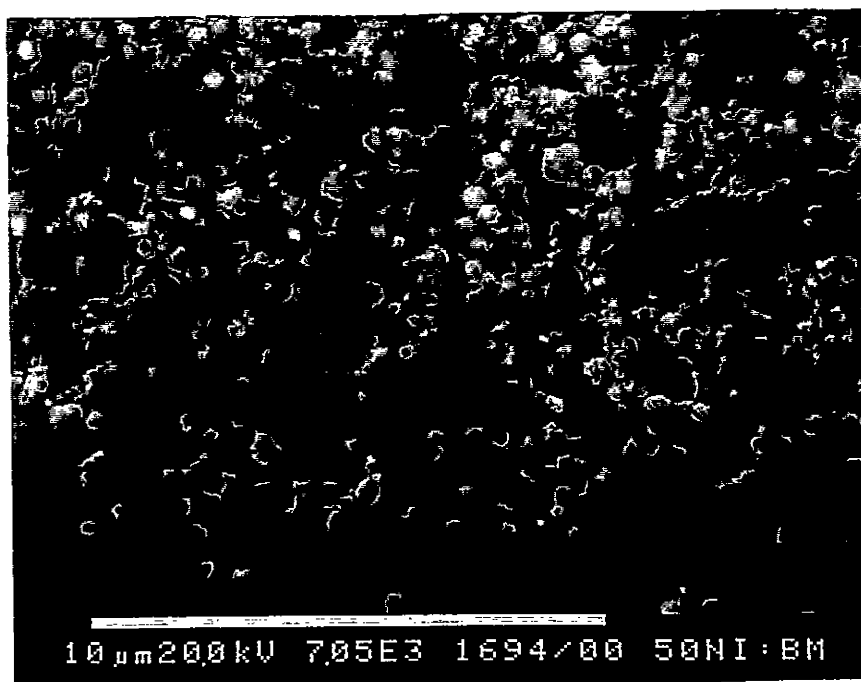
examined via scanning electron microscopy (SEM) and are illustrated in Fig 5.1. The tapes exhibit well dispersed characteristics. The bottom surface shows fine, evenly distributed porosity due to shrinkage constraint of the glass substrate. The microstructures of densified composites, shown in the optical micrographs of Figures 5.2-5.4, show well dispersed phases of comparable phase scale. Some anisotropy is apparent between transverse sections (i.e. hot pressing plane) and axial sections. Figure 5.5 defines the nomenclature used to describe planes and directions in regards to specimen orientation.

The phase intercept lengths of the second phase in 75% metal and 75% ceramic composite micrographs were evaluated using the Feret function included with the Leco® 2001 image analysis software. A Feret dimension (named after a French mathematician) is a straight line measurement made between parallel outermost tangents of a particle, as illustrated in Figure 5.6. These Feret measures can be used to describe the size and distribution of the second phase and the microstructural anisotropy in planar images. Microstructural characterization of the 50:50 composite was handled manually by measuring the intercept lengths of each phase along a random line. Tables 5.1 and 5.2 contain these measurements. In summary the mean phase intercept lengths are of the order 2-3  $\mu\text{m}$ , the second phase aspect ratio is about 1.6-2.0, and the microstructural aspect ratio (the indicator of anisotropy) is about 1.5.

Composite densities all exceeded 98% of theoretical, as determined by the fluid displacement technique. Table 5.3 lists the densities achieved in all hot pressed materials. Both water and ethanol were used to confirm results. Polished phases often

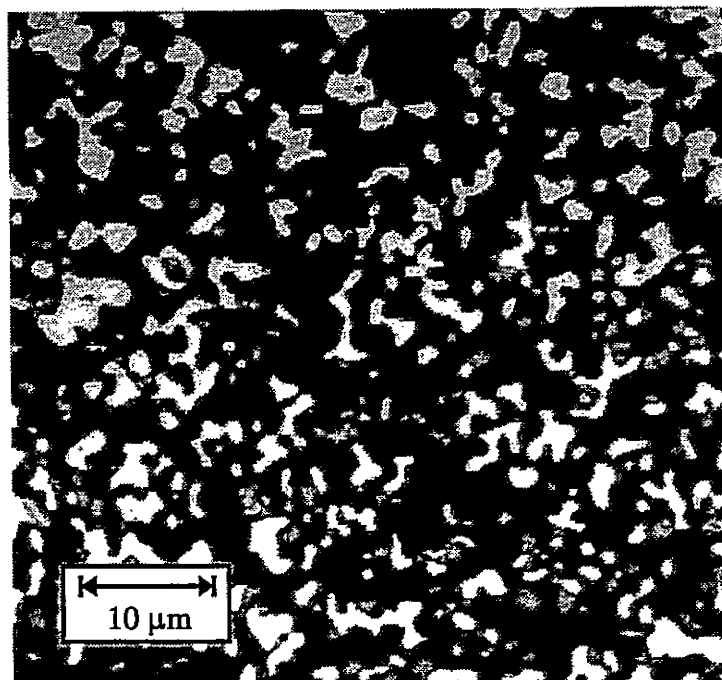


(a)

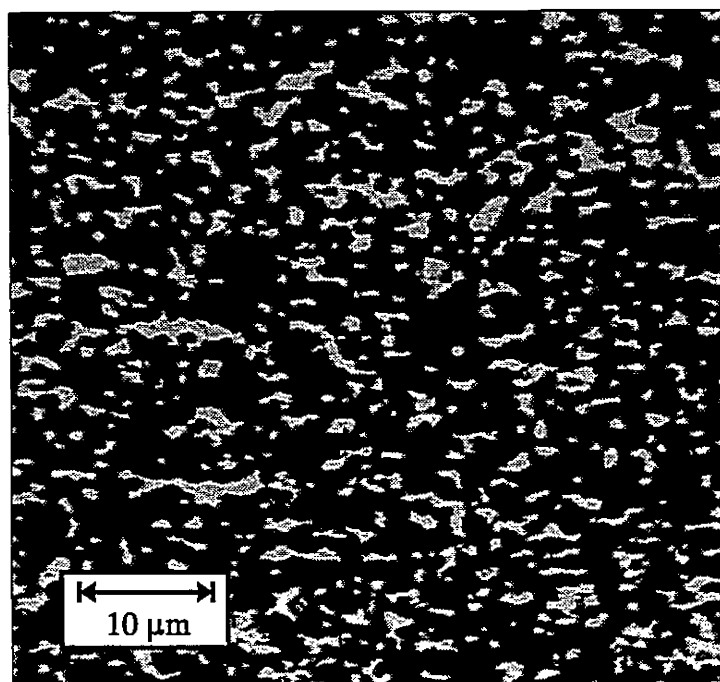


(b)

**Figure 5.1:** 50%Ni:50%TZ8Y composite green tapes revealing dispersive characteristics, (a) unconstrained surface (top of tape), (b) constrained surface (dried in contact with glass substrate).



(a)



(b)

**Figure 5.2:** Optical images of 25%Ni:75%TZ8Y in (a) transverse section (i.e. hot pressing plane), (b) axial section (i.e. perpendicular to hot pressing plane).

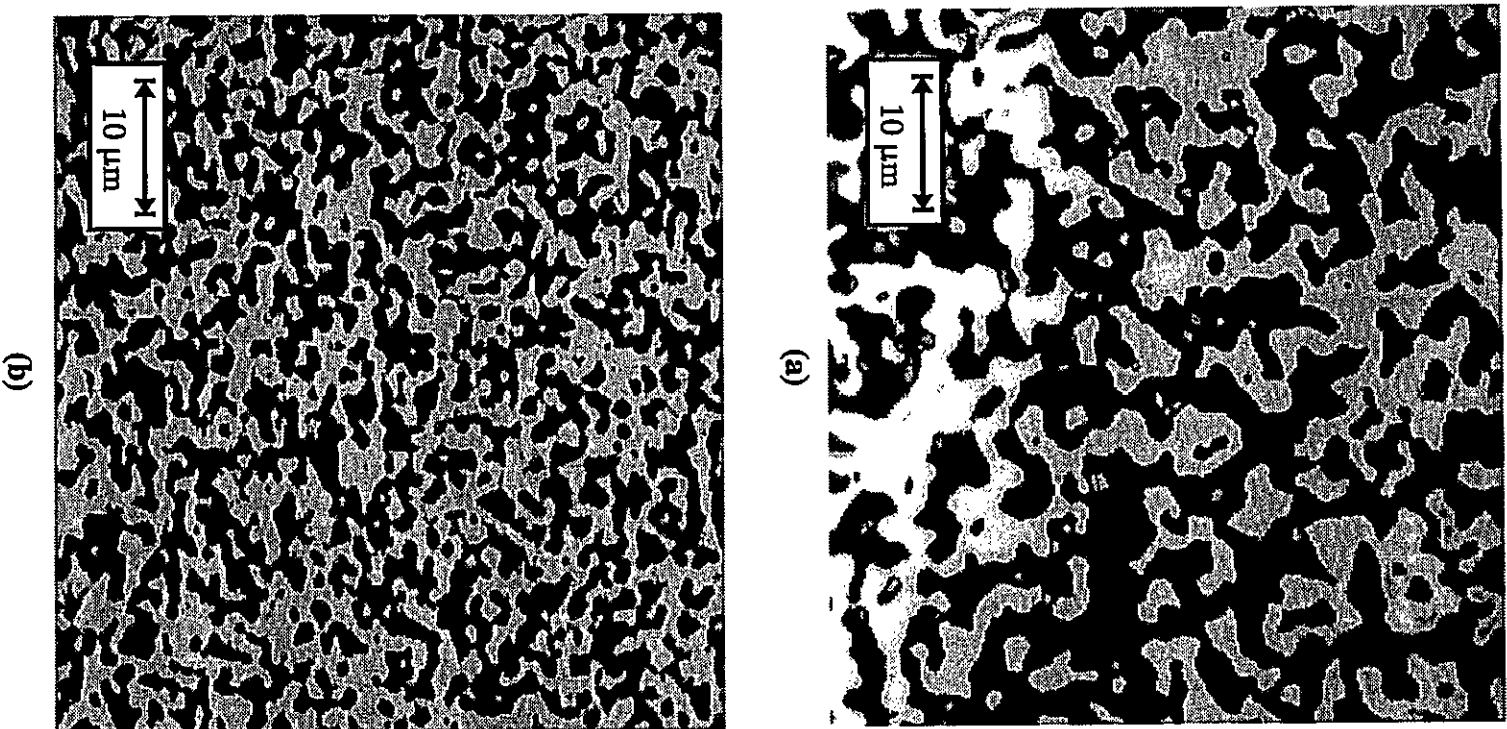
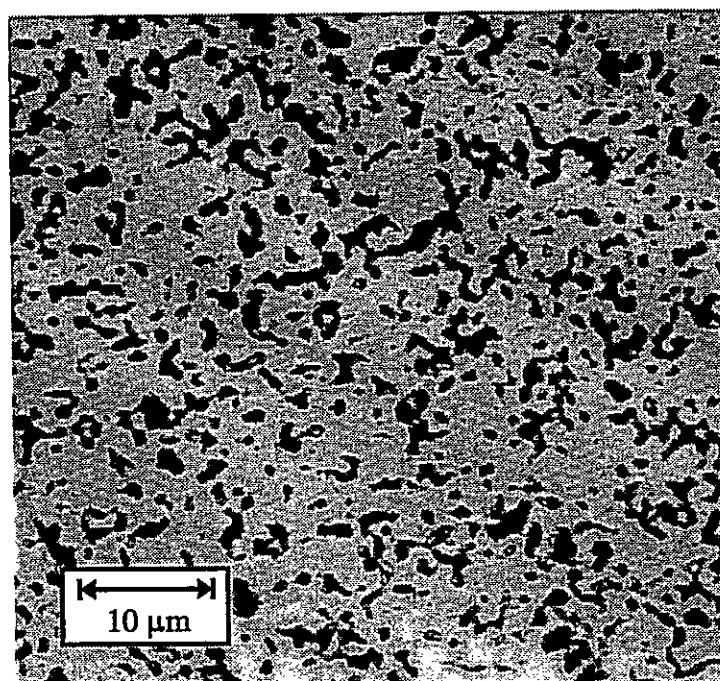
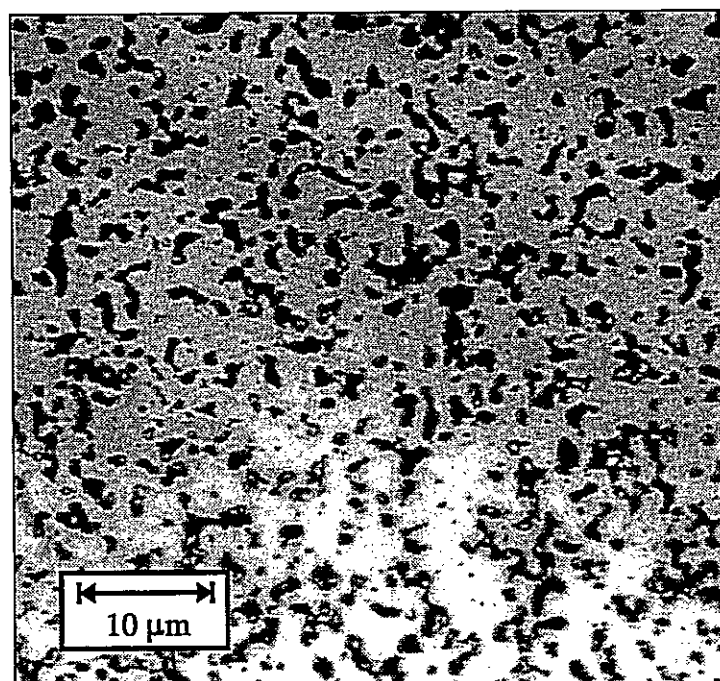


**Figure 5.3:** Optical images of 50%Ni:50%TZ8Y in (a) transverse section (i.e. hot pressing plane), (b) axial section (i.e. perpendicular to hot pressing plane).



(a)



(b)

**Figure 5.4:** Optical images of 75%Ni:25%TZ8Y in (a) transverse section (i.e. hot pressing plane), (b) axial section (i.e. perpendicular to hot pressing plane).

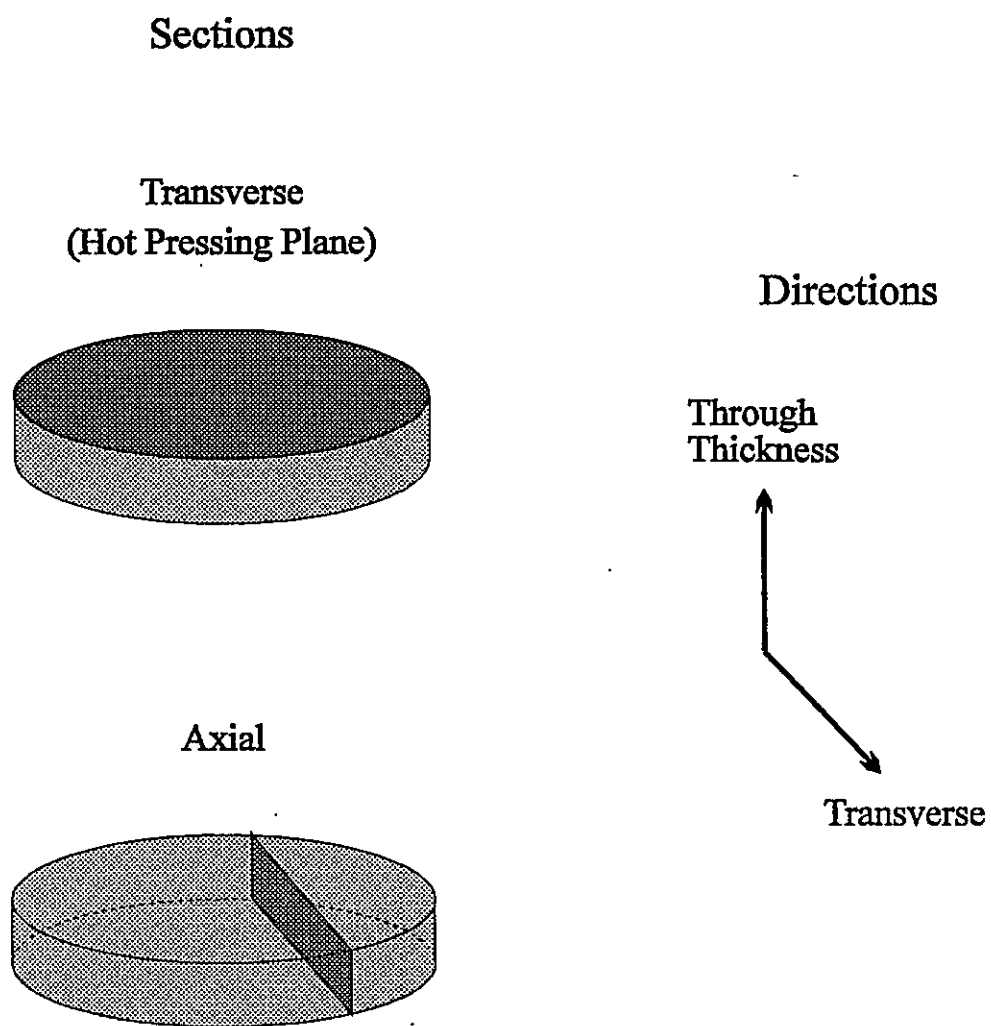


**Figure 5.5:** Schematic of section and direction nomenclature used to characterize composite micrographs.

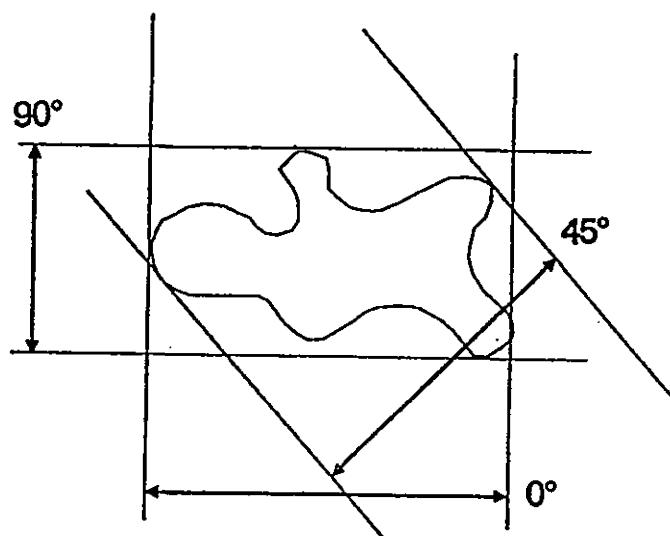


**Figure 5.6:** Schematic representation of ferets (i.e. straight line measurements made between tangents at various angles) shown in three feret angles. (From Leco<sup>®</sup> 2001 reference manual).

**Table 5.1:** Morphology of second phase in 25% Ni and 25% TZ8Y composites.

Composite Grade	Specimen Orientation	Feret Measurements ( $\mu\text{m}$ )			Microstructural Aspect Ratio	Second Phase Aspect Ratio
		0°	90°	Average		
25 vol% Ni	transverse	2.0	2.0	2.0	1.0	1.7
	axial	2.0	1.2	1.7	1.6	2.0
25 vol% TZ8Y	transverse	1.9	1.9	1.9	1.0	1.6
	axial	1.4	1.0	1.2	1.4	1.7

**NOTES:**

Specimen section and direction orientation is defined in Figure 5.5.

Feret orientation is relative to specimen orientation. Feret nomenclature is defined in Figure 5.6. Feret average is the average of 8 ferets measured for a particle.

Microstructural aspect ratio is the ratio of the average second phase Feret measurements at 0° and 90°. Second phase aspect ratio is the average, particle specific, aspect ratio.

**Table 5.2:** Phase intercept length (L) in 50%Ni:50%TZ8Y composite (in  $\mu\text{m}$ ).

Specimen Orientation	Measurement Direction	Nickel Phase-L		Zirconia Phase-L	
		L-avg.	Std. dev.	L-avg.	Std. dev.
transverse	random	2.9	3.2	3.2	2.2
axial	random	1.4	1.1	1.7	1.2
	transverse	1.7	1.3	1.8	1.4
	thickness	1.3	1.1	1.7	1.3

**Table 5.3:** Hot pressed densities measured using the fluid displacement technique.

Composite Grade (vol %)	Sample Density (g/cm <sup>3</sup> )	Approximate % density (% of theoretical)
100% Ni	8.73	98.1
75:25	8.00	97.7
50:50	7.31	98.2
25:75	6.60	98.2
100% TZ8Y	5.97	99.4

reveal higher degrees of apparent porosity; however, much of this is a polishing effect whereby grains are mechanically pulled out. This effect complicates area fraction image analysis.

The grain sizes of each phase within a composite were examined using mean grain intercept lengths ( $L$ ). Thermal etching in air for 5 minutes at  $1200^{\circ}\text{C}$  reveals a grain size of  $L \approx 0.25 \mu\text{m}$  in 100% TZ8Y (Fig. 5.7). TEM examination revealed comparable grain sizes in both the 100% TZ8Y and the ceramic phase of 50% TZ8Y composites. Thermal etching of composites at  $750^{\circ}\text{C}$  in  $\text{H}_2$  revealed a nickel phase grain size of  $L \approx 3\text{-}5 \mu\text{m}$  in the composites. Nickel processed at  $950^{\circ}\text{C}$  produces  $L \approx 5 \mu\text{m}$ , while subsequent heat treatments of nickel at  $950^{\circ}\text{C}$  (5 hours) increases this to  $L \approx 10 \mu\text{m}$ .

### 5.1.2 TEM Characterization of TZ8Y, Ni and Ni/TZ8Y Composites

Transmission Electron Microscopy (TEM) examination of 100% ceramic samples (Fig. 5.8) revealed a solid solution of cubic stabilized zirconia. In contrast, the ceramic within the composites was identified as a two phase material (Fig 5.9). The twinned grain morphology encompasses about 95% of the ceramic volume with a crystal structure identified as tetragonal zirconia. The minor ceramic phase is yttria having a cubic structure. Crystal structures were identified using select area diffraction analysis. The average grain size of the ceramic phases are comparable, giving cubic grains distributed in a tetragonal zirconia matrix. Figures 5.10 and 5.11 reveal the characteristics of nickel/zirconia, nickel/yttria, and zirconia/yttria interfaces. The M/C interfaces are atomically clean, without reaction products or metal oxide barrier. Nickel grain interiors

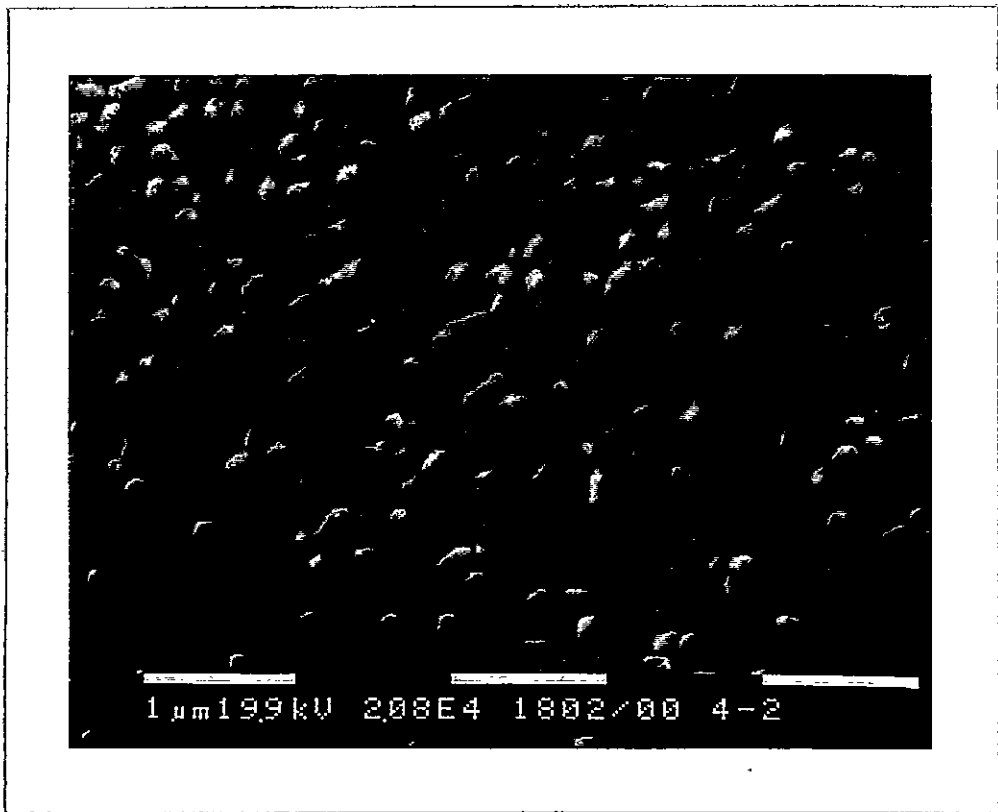


**Figure 5.7:** Grain structure developed in TZ8Y (consolidated at 1250°C for 3 hours and thermally etched at 1200°C for 5 minutes).

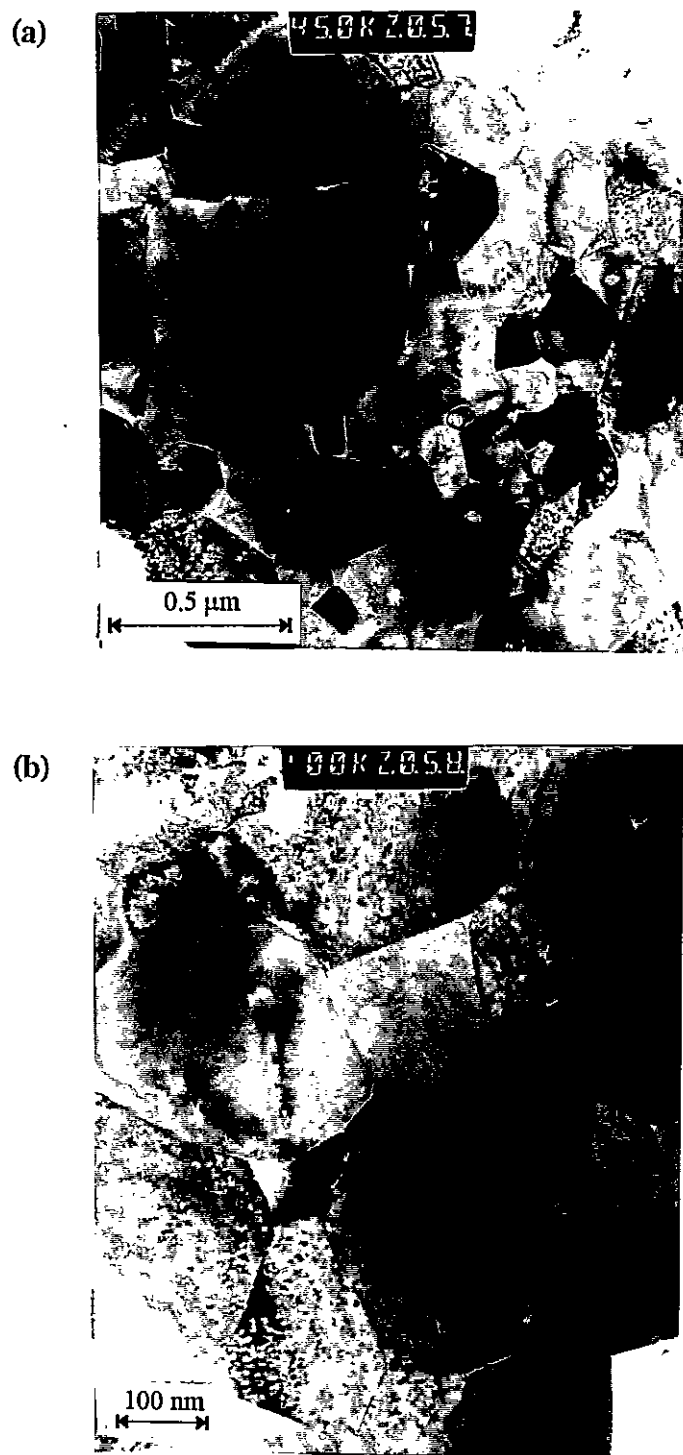


Figure 5.8: TEM images of 100% TZ8Y.

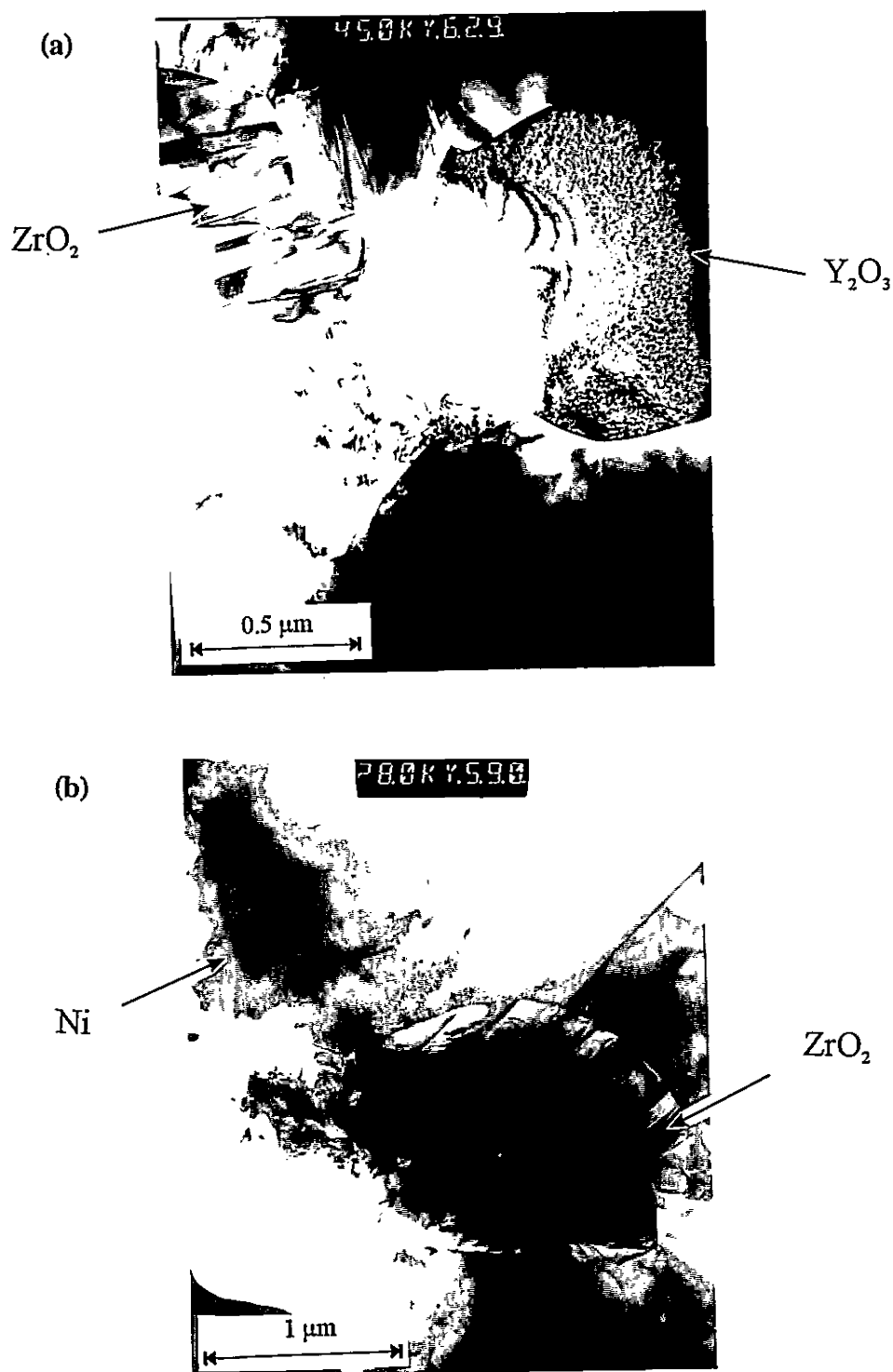
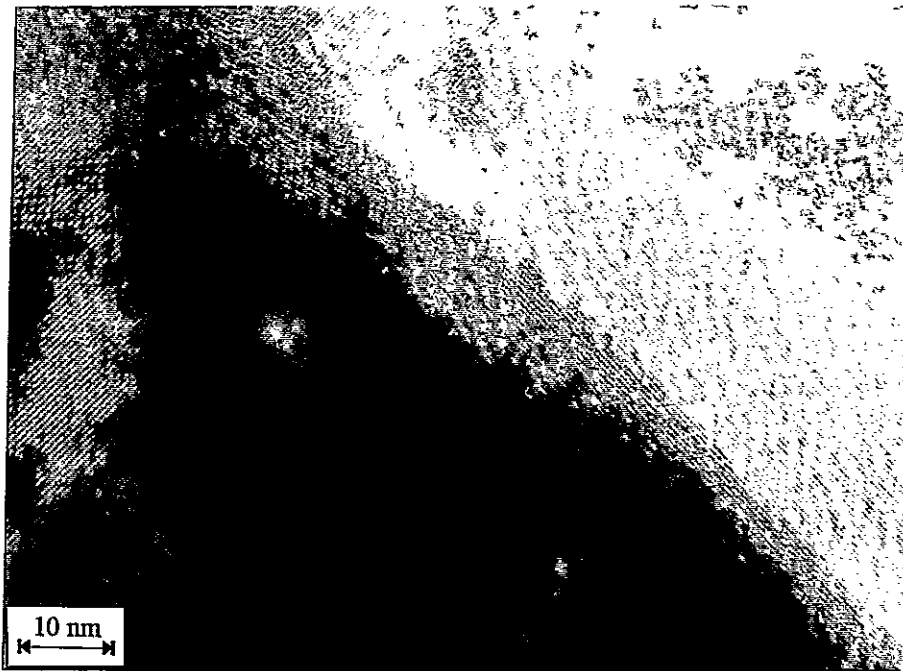
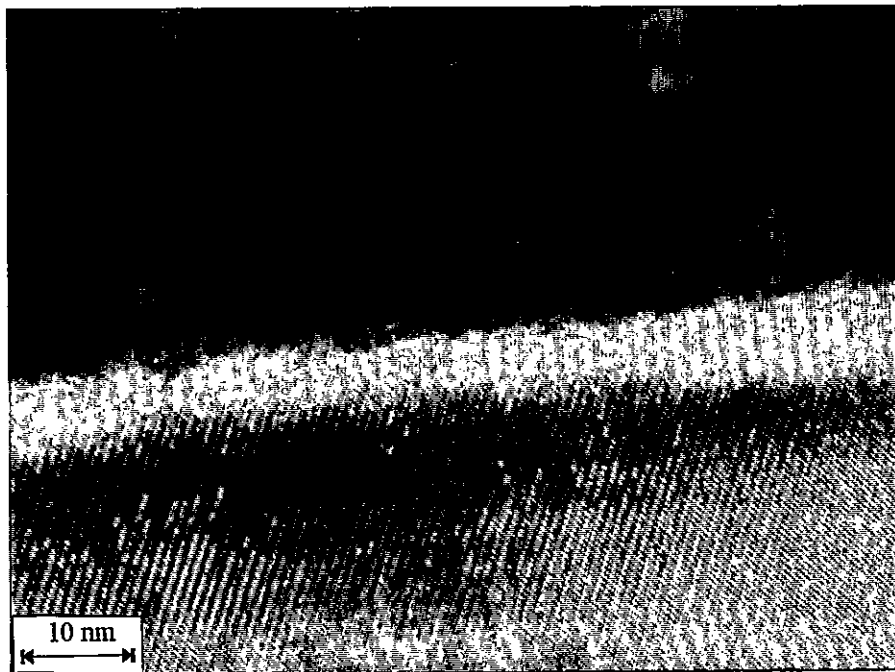


Figure 5.9: TEM images of 50%Ni:50%TZ8Y composite revealing two phase ceramic.



(a)



(b)

Figure 5.10: TEM images of composite interfaces, (a) Ni-ZrO<sub>2</sub>, (b) Ni-Y<sub>2</sub>O<sub>3</sub>.



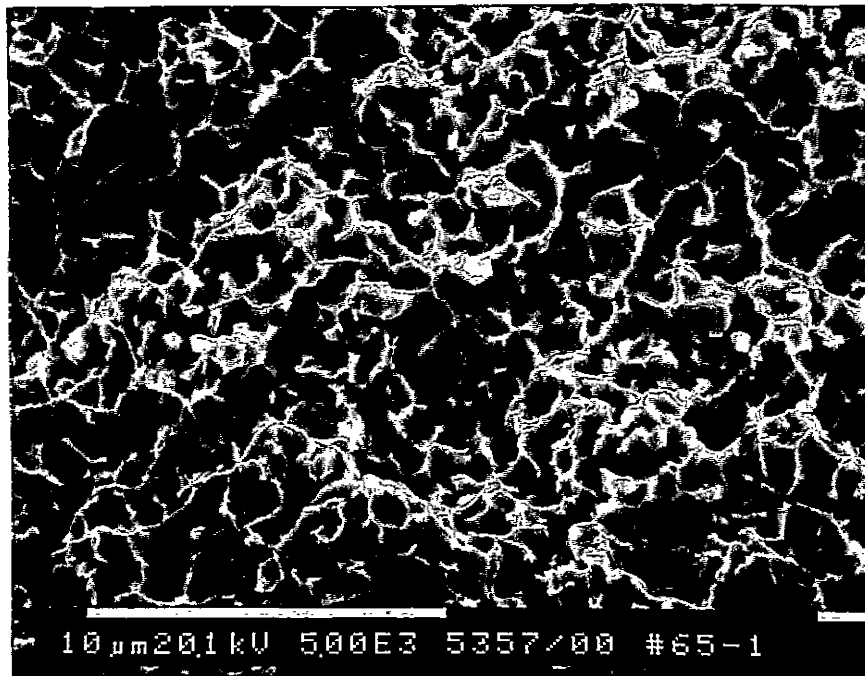
**Figure 5.11:** TEM image of  $ZrO_2$ - $Y_2O_3$  interface in ceramic phase of 50%Ni:50%TZ8Y composite.

within the composites are free of oxides or other dispersed phases and show a heavily twinned structure.

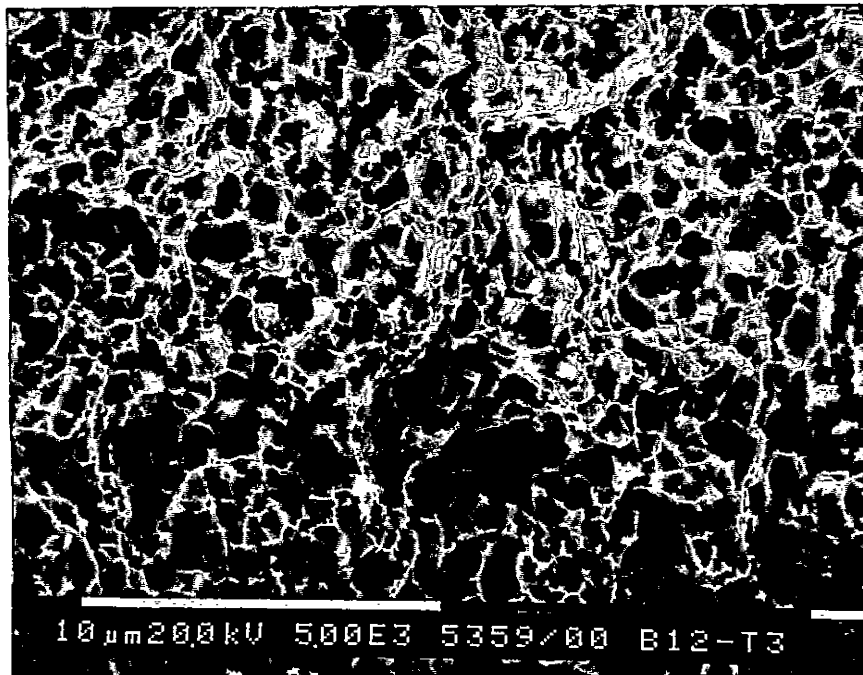
TEM was performed on nickel samples to compare nickel processing at 950°C via hot pressing in vacuum (HP), pressureless sintering in H<sub>2</sub> (PS-H<sub>2</sub>), and the resulting structures following heat treatments in argon (HT-Ar). In the as processed condition nickel grain interiors were heavily twinned while structures after HT showed little twinning. Nickel, after HP at 950°C, contains oxide particles at grain boundaries and within grains. Oxide particles range in size from 0.03 μm to 0.3 μm and occupy about 4 percent of the material volume. The larger particles are found along the grain boundaries. EDS and diffraction pattern indexing revealed the particles to be primarily nickel oxide; however, some NiAl<sub>2</sub>O<sub>4</sub> spinel was identified. Treating the HP nickel (HT-Ar at 950°C) produced large oxide clusters at triple grain junctions. Few particles were seen within the grains. Nickel after PS-H<sub>2</sub> at 950°C contains some fine Ni<sub>3</sub>Al intermetallic particles (of about 10 to 20 nm and occupying ≤ 1 vol%). Oxide particles were not found. However, following HT-Ar at 950°C, oxide particles were seen within grains and along grain boundaries.

### 5.1.3 Fractography

SEM micrographs of nickel and composites fracture surfaces were prepared. The series of images in Figures 5.12-5.14 outlines the different fracture behaviour observed in nickel following processing by PS-H<sub>2</sub> or HP-vac and following subsequent HT-Ar. For comparison the nickel grain size after processing at 950°C and subsequent treatments

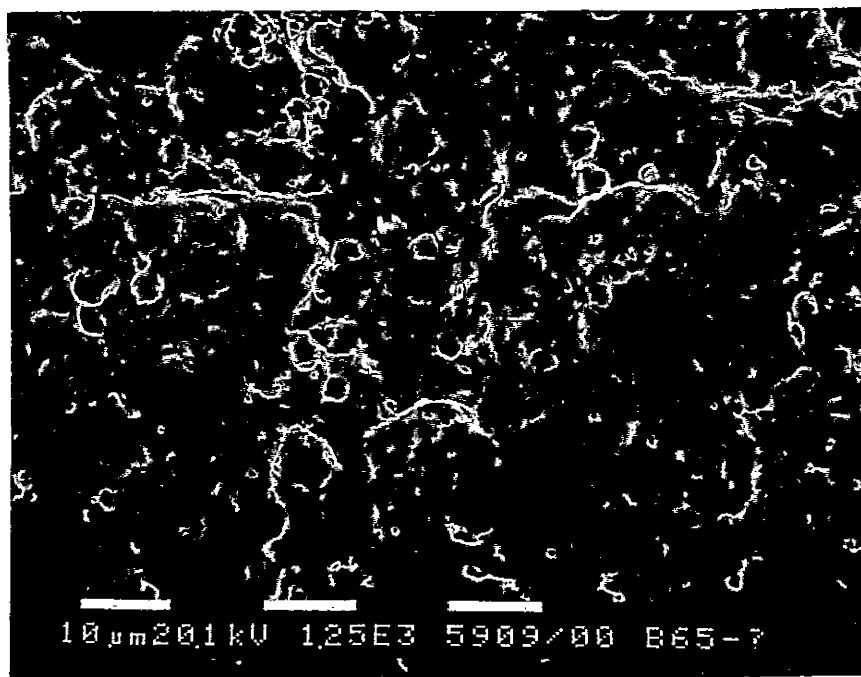


(a)

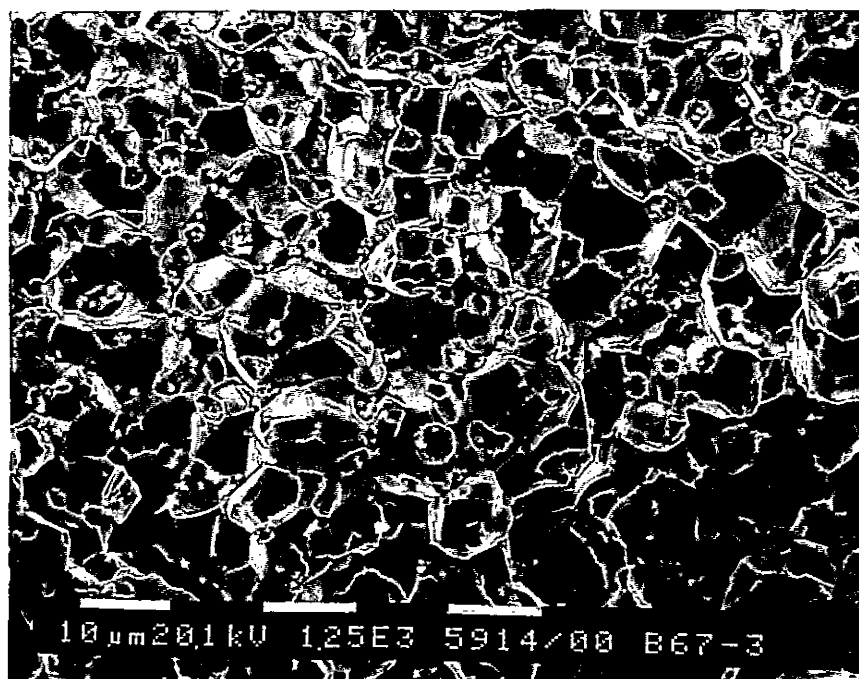


(b)

Figure 5.12: Fracture surfaces of ONF-nickel processed at 950°C by (a) pressureless sintering in flowing Ar-5% $H_2$ , (b) hot pressing in vacuum.

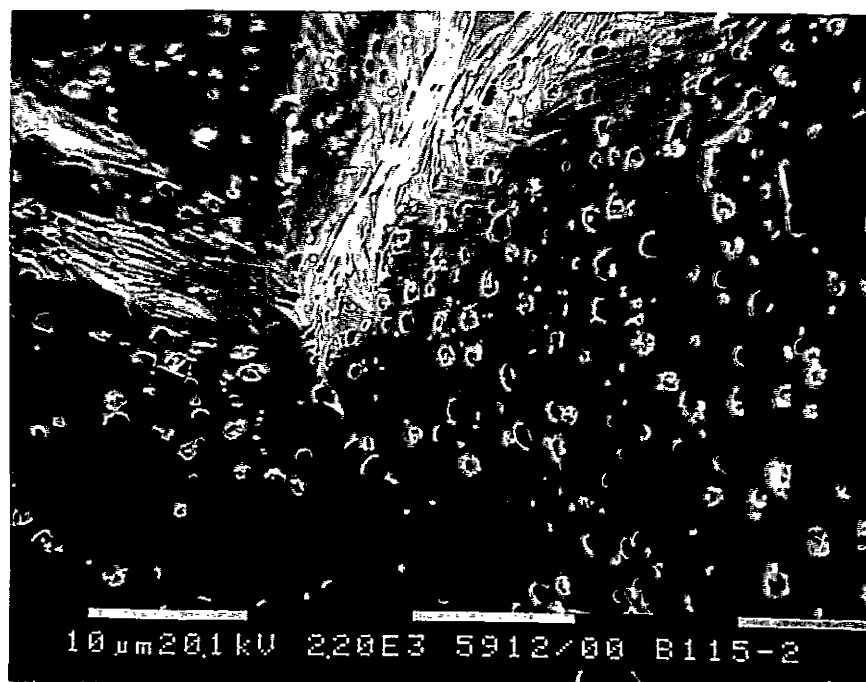


(a)

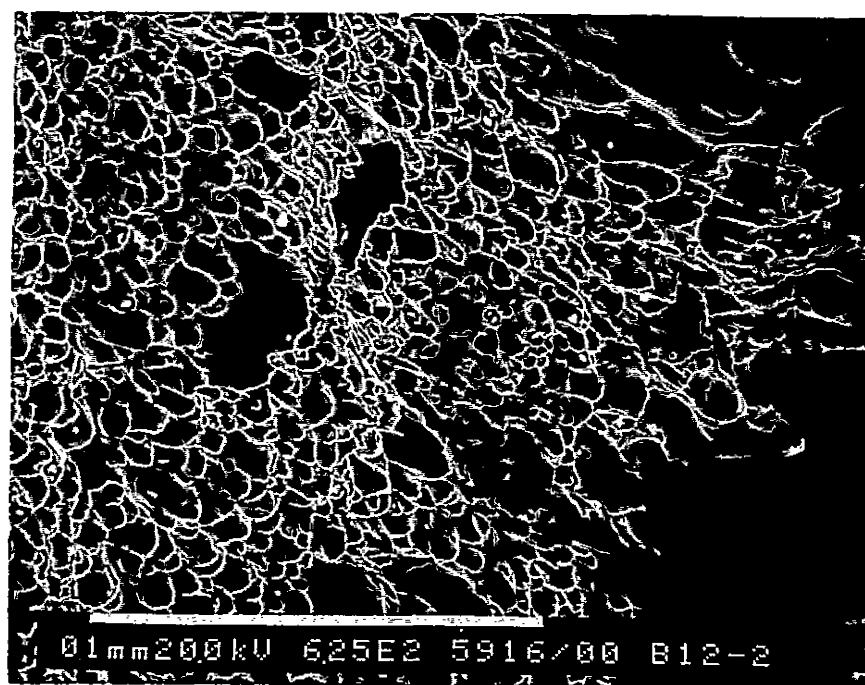


(b)

**Figure 5.13:** Fracture surfaces of ONF-nickel after heat treating (950°C for 5 hours in flowing argon) for (a) initially pressureless sintered, (b) initially hot pressed.



(a)



(b)

**Figure 5.14:** Fracture surfaces of ONF-nickel after heat treating (1250°C for 1 hours in flowing argon) for (a) initially pressureless sintered, (b) initially hot pressed.

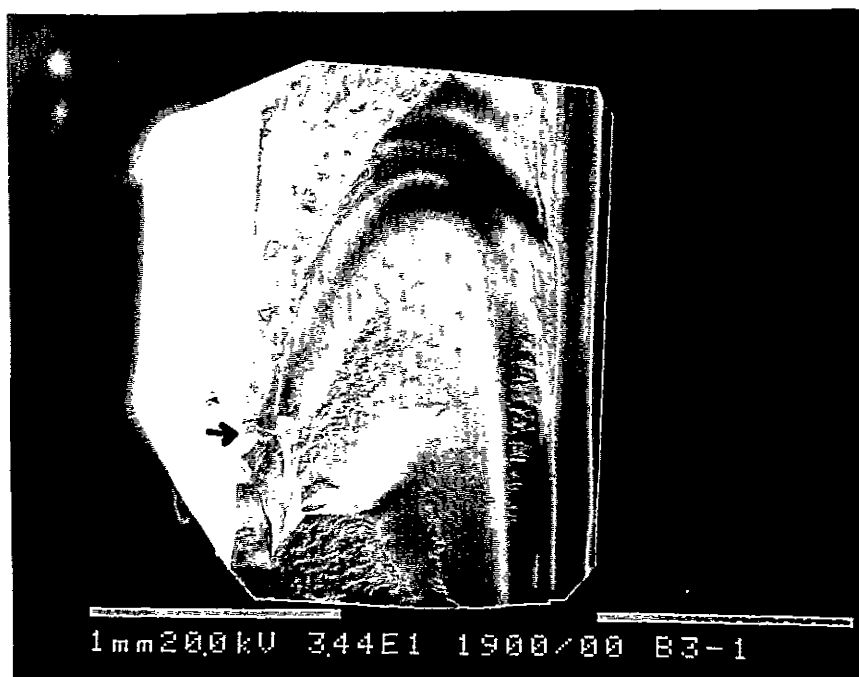
at 950°C and 1250°C are  $\approx 5 \mu\text{m}$ ,  $\approx 10 \mu\text{m}$  and  $\approx 1000 \mu\text{m}$ , respectively. Particles are not visible in Figure 5.12a while small particles are visible within the voids in Figure 5.12b. The particles seen in Figure 5.13a are nickel grains likely having undergone intergranular decohesion. Grain boundary particles are clearly seen in Figure 5.13b and were identified, via TEM, as spinel clusters. Numerous oxide particles are seen in Figure 14a (showing cleavage type rupture, possibly intergranular) and in the voids of Figure 14b (revealing more ductile characteristics).

The general appearances of 100% TZ8Y and composite fracture surfaces are shown in Figure 5.15. The tensile surface of the flexure bar is the edge opposite the side showing the hill and valley topography. The fracture path in 100% TZ8Y clearly marks fracture initiation while the location of fracture initiation in composites is not obvious. High magnification fracture images for the 100% TZ8Y and for the composites are included in Figures 5.16-5.17. The ceramic shows both intergranular and transgranular fracture characteristics, whereas the nickel phase (in bright contrast) reveals more ductile characteristics (clearly seen in Figure 5.16b).

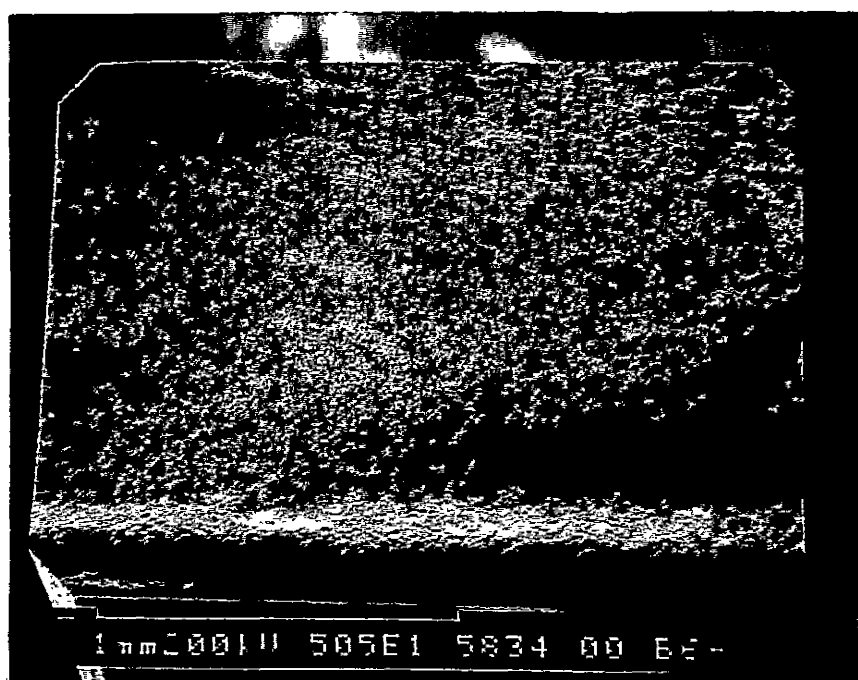
## 5.2 Material Properties

### 5.2.1 Elastic Properties

Ambient temperature elastic properties were measured using the pulse-echo technique. The average values along with the standard error for the Young's modulus in each composite grade is displayed in Figure 5.18a. Poisson's ratio, calculated from the same test results, is displayed in Figure 5.18b.

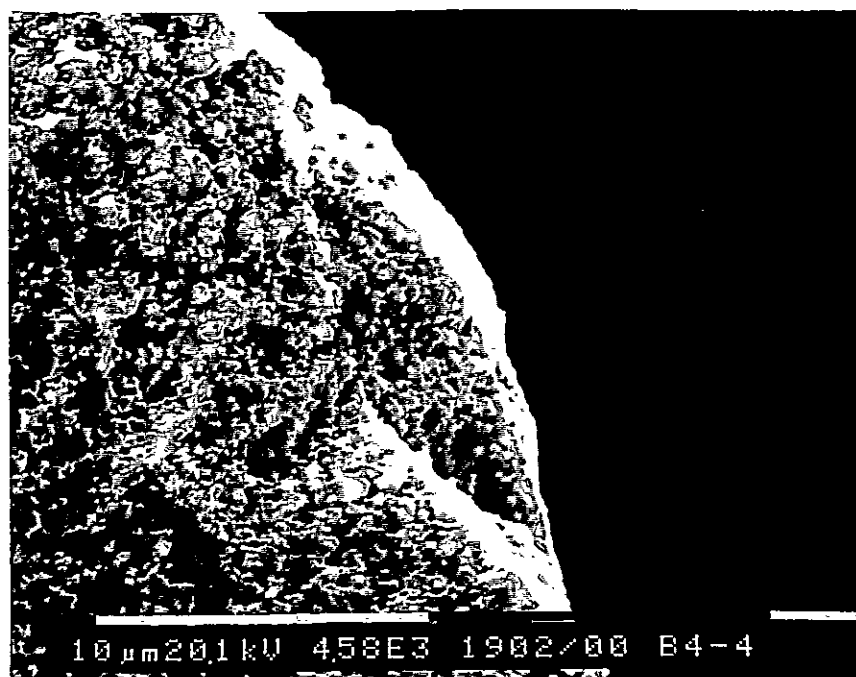


(a)

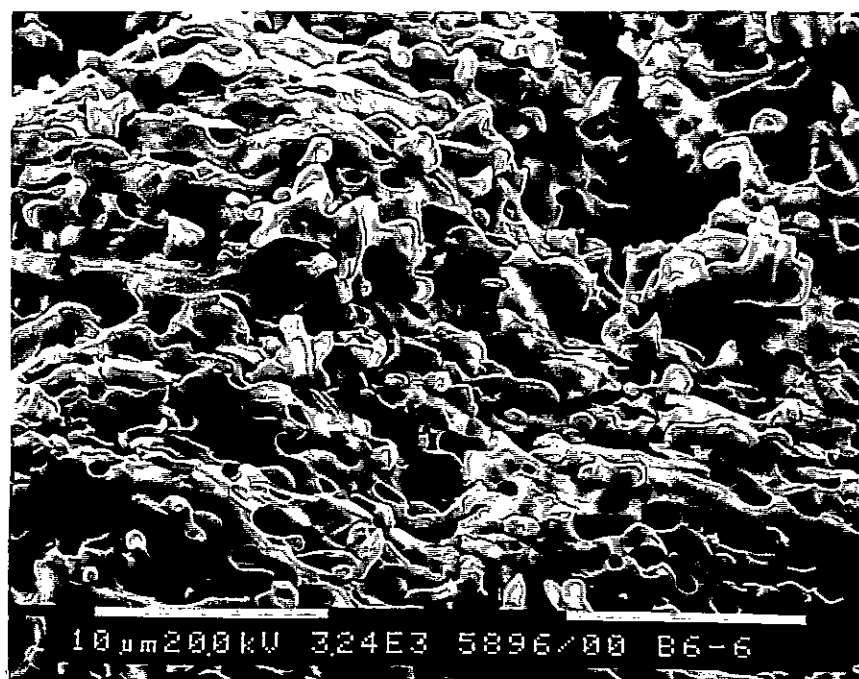


(b)

Figure 5.15: Fracture appearances of (a) 100% TZ8Y, fracture origin identified by arrow, (b) 25%Ni:75%TZ8Y composite, tensile surface at top of image.

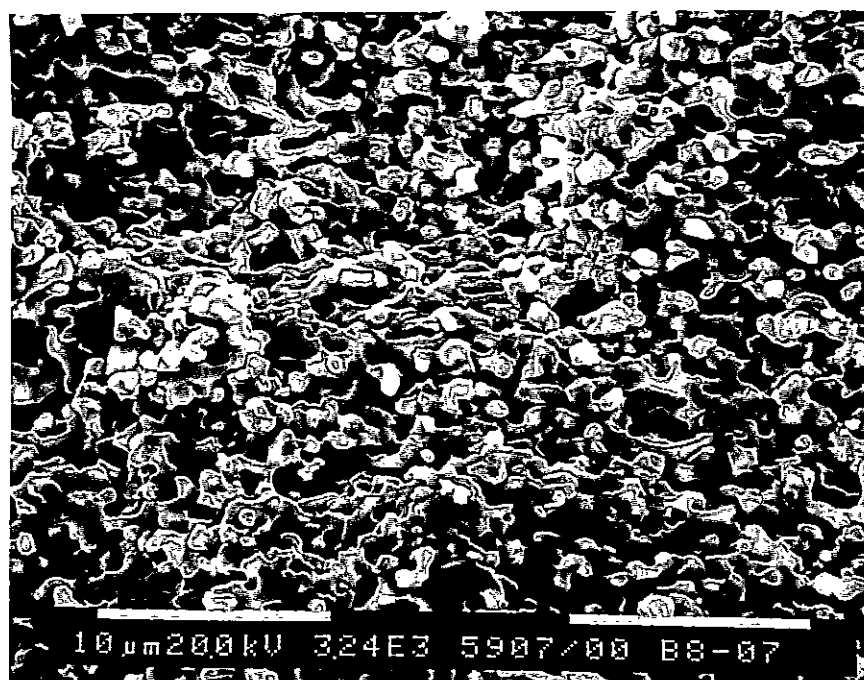


(a)



(b)

**Figure 5.16:** Fracture images of (a) 100% TZ8Y, including origin of fracture, (b) 25%Ni:75%TZ8Y (brighter phase is nickel).

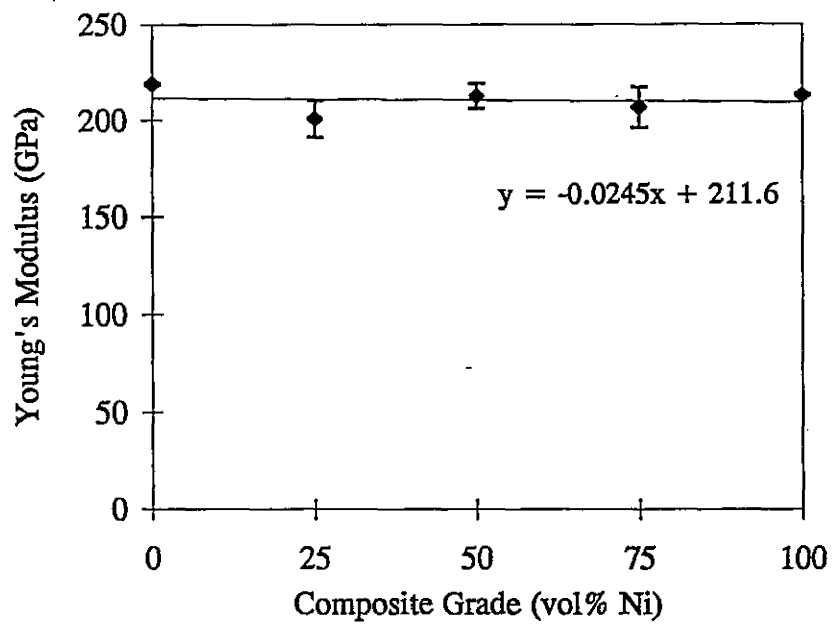


(a)

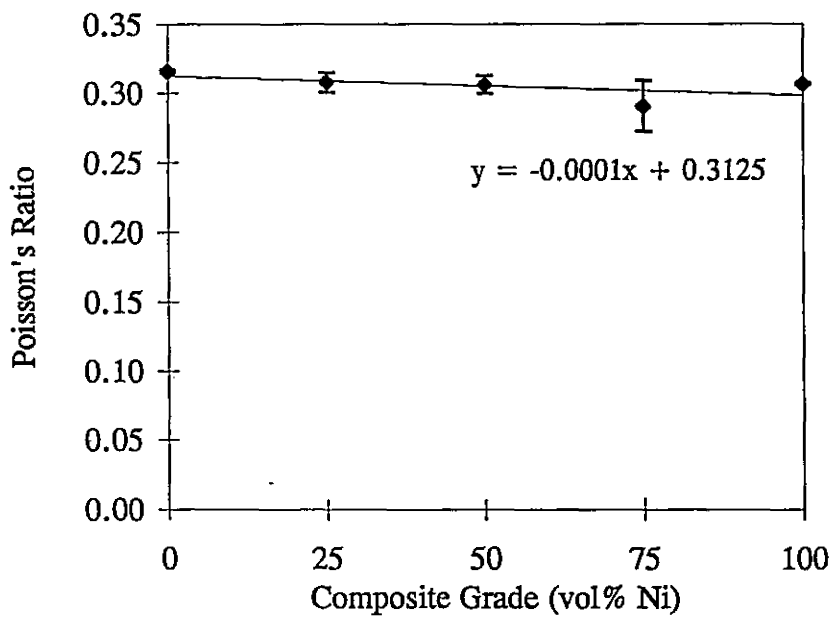


(b)

Figure 5.17: Fracture images of (a) 50%Ni:50%TZ8Y, (b) 75%Ni:25%TZ8Y. Brighter phase is nickel.



(a)



(b)

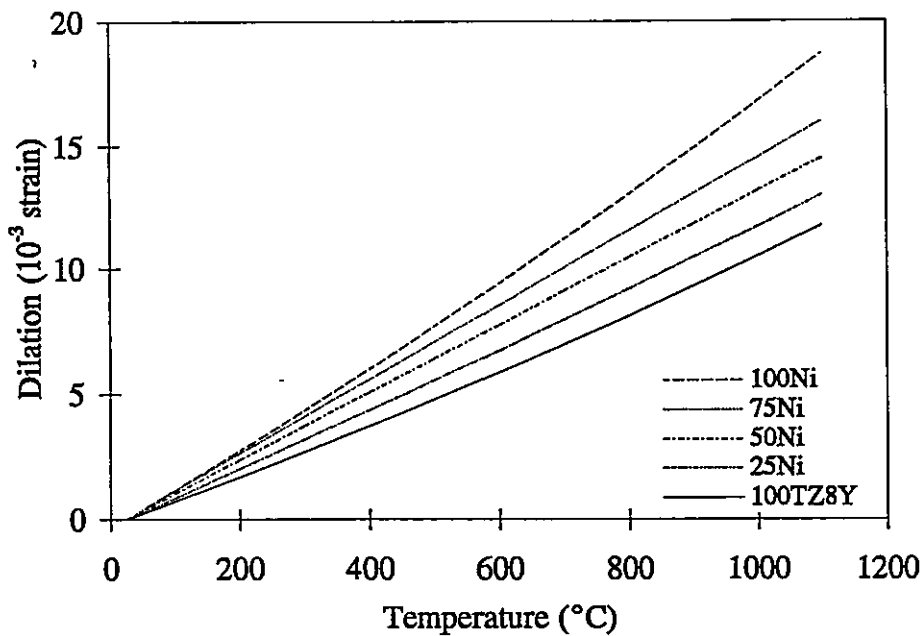
**Figure 5.18:** Elastic Properties of Ni:TZ8Y composites, (a) Young's Modulus, (b) Poisson's ratio.

### 5.2.2 Thermal Dilation Response

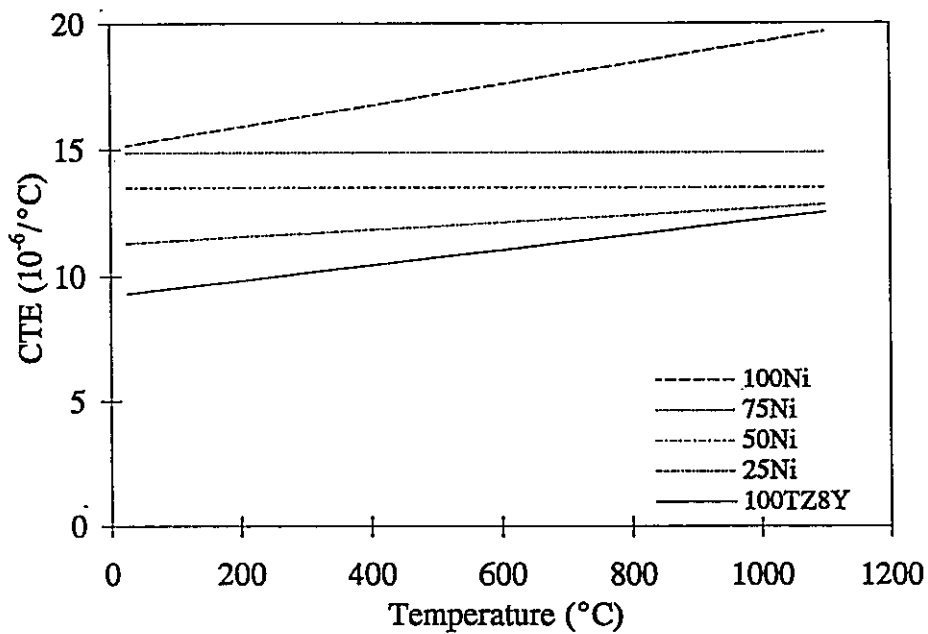
The dilation data upon cooling of all specimens yield smooth continuous characteristics. This cooling provides dilation characteristics analogous to those experienced during processing and subsequent heat treatments. It is therefore appropriate to use the cooling data in the composite comparison. The dilation-temperature data were curve fit, with correlations not less than  $R_2=0.9999$ , and plotted as Figure 5.19a. Differentiating the curve-fit equations yields the coefficient of thermal expansion (CTE) as a function of temperature for these materials as shown in Figure 5.19b.

### 5.2.3 Mechanical Behaviour of Processed Nickel

Various measurements have been performed on 100% Ni samples to examine mechanical behaviour. For purposes of data comparison, a yield strength can be estimated from both the flexure data and hardness data. The onset of non-linearity in a flexure test approximates the onset of yielding as shown in Figure 5.20. The HP curve in Figure 5.20a can be compared to tensile data shown in Figure 5.21. The tensile data indicates very low ductility as failure occurs prior to yielding according to the standard 0.2% offset technique. A 0.1% offset estimates the  $\sigma_{ys} \approx 750$  MPa, compared to  $\approx 950$  MPa from flexure data. More realistic values for yielding in this high strength material may be around 800 MPa. The flexural yield stress for low strength material is expected to more closely resemble tensile yield due to the well defined yield transition. Sufficient testing was performed to correlate yield stress to measured hardness, shown in Figure 5.22a. The relation  $\sigma_{ys} \approx H/3$  can be applied to high hardness nickel while low hardness

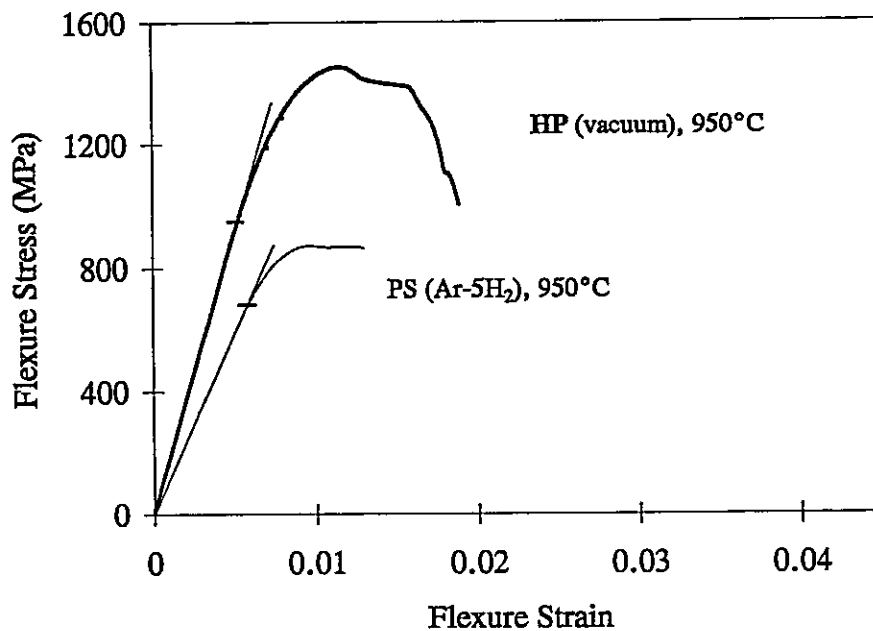


(a)

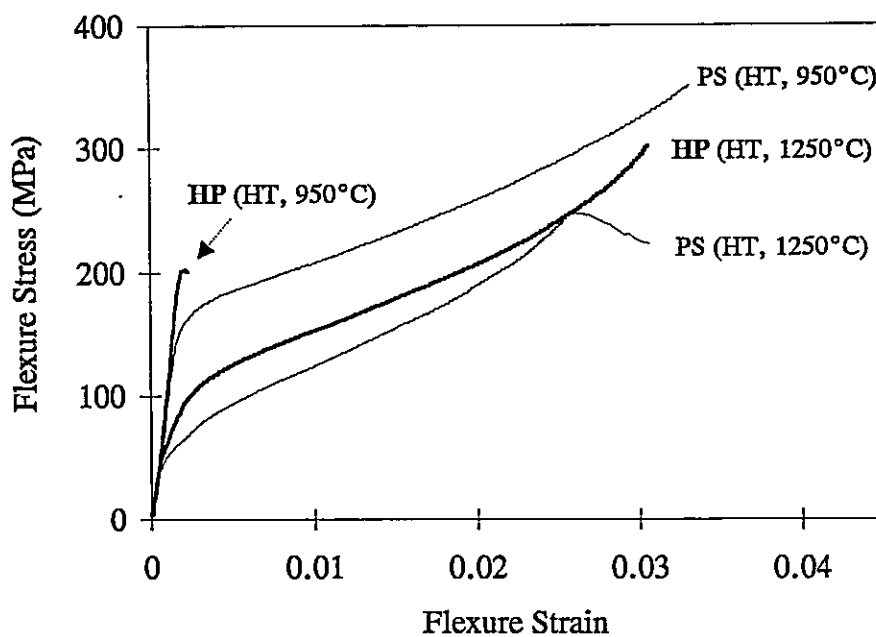


(b)

**Figure 5.19:** Thermal expansion response for the composites shown via (a) dilation-temperature dependence, (b) coefficient of thermal expansion-temperature dependence.



(a)



(b)

**Figure 5.20:** Flexure response of ONF-nickel in (a) as processed condition, (b) heat treated condition.

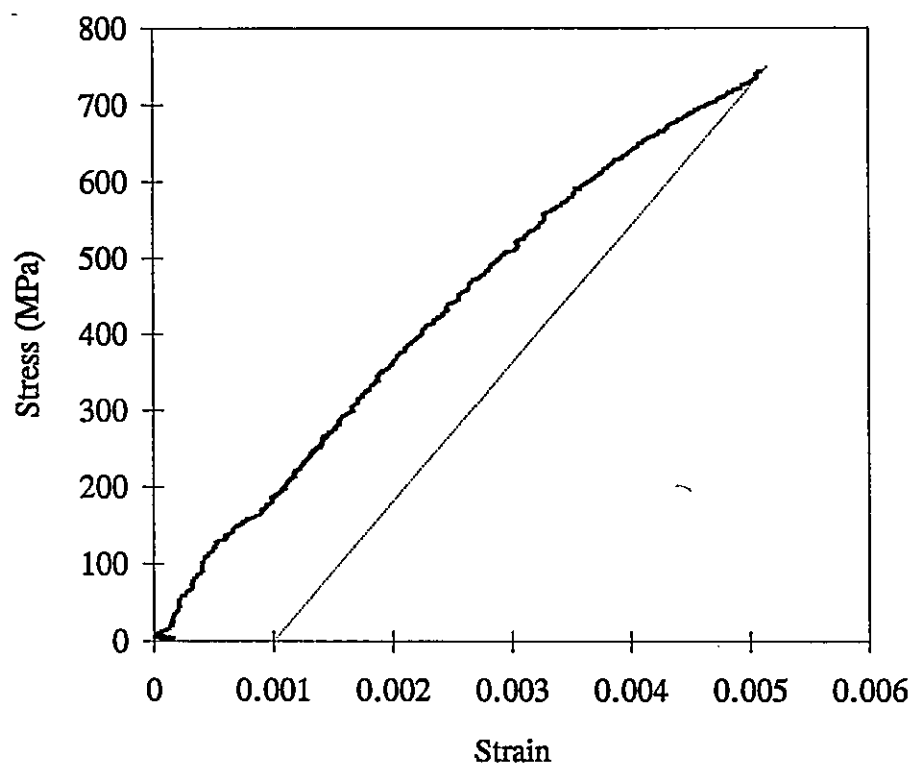
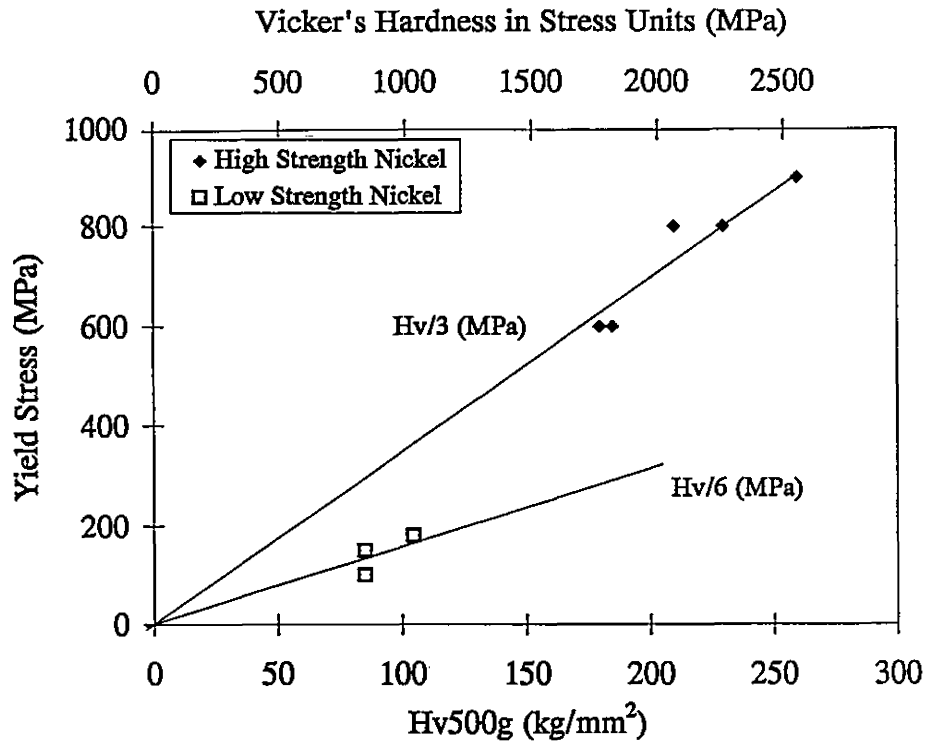


**Figure 5.21:** Tensile profile for ONF-nickel hot pressed at 950°C in vacuum. 0.1% offset yield point indicated.

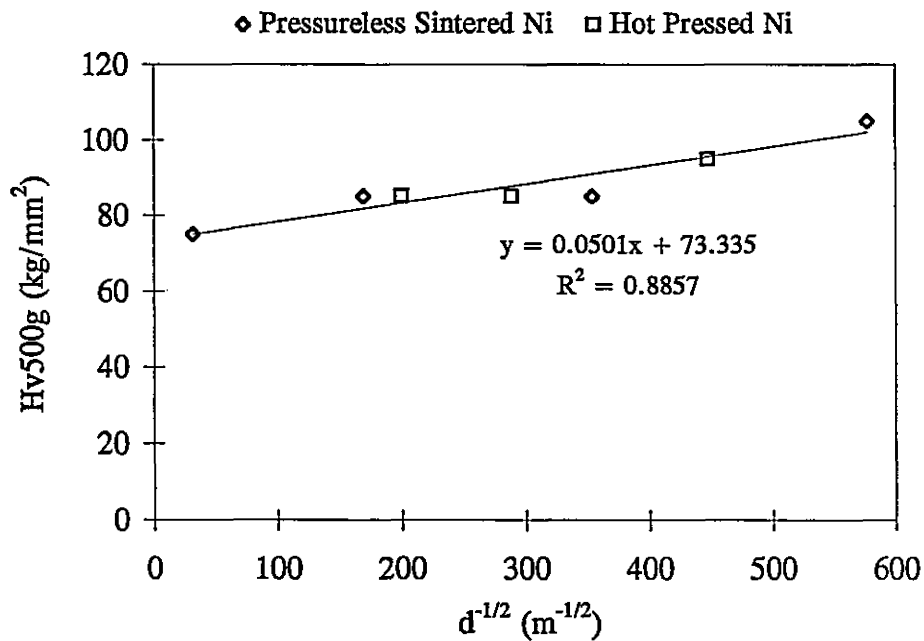
nickel ( $\approx 100 \text{ kg/mm}^2$ ) is best represented by  $\sigma_{ys} \approx H/6$ . Figure 5.22a enables estimations of yield strength from hardness for nickel and for the nickel phase within composites.

The effects of processing route and subsequent heat treatment on the hardness and flexure behaviour of nickel are shown in Figures 5.23 and 5.20. Flexure test results can be compared with the fracture surfaces in Figures 5.12-5.14. Nickel processed at  $950^\circ\text{C}$  via HP or PS- $\text{H}_2$  exhibits very high hardness and strength but low ductility. High temperature processing ( $1200^\circ\text{C}$ ) via HP produces hardnesses approaching typical annealed levels for nickel while PS- $\text{H}_2$  at  $1200^\circ\text{C}$  nickel retains a higher hardness. Nickel processed at  $950^\circ\text{C}$  indicates no change in hardness following HT- $\text{H}_2$  at  $950^\circ\text{C}$  (not shown in figures due to data overlap), while HT-Ar at  $950^\circ\text{C}$  significantly reduces hardness and strength. Notice that nickel HP at  $950^\circ\text{C}$  followed by HT-Ar at  $950^\circ\text{C}$  exhibits no ductility which is in agreement with its intergranular fracture behaviour. Subsequent HT-Ar at  $1200^\circ\text{C}$  of the nickel processed at  $950^\circ\text{C}$  results in hardnesses and yield strengths typical of annealed nickel, with yet low ductility. A gradual decrease in hardness for increasing HT temperature is likely the result of increasing grain size as indicated in Figure 5.22b. The maximum levels of strain experienced prior to fracture in these nickel bars is  $<4\%$  before large cracks develop. The hardness of PS nickel after HT-Ar at  $950^\circ\text{C}$  was  $105 \text{ kg/mm}^2$  prior to flexure testing and  $160 \text{ kg/mm}^2$  at the tensile surface after flexure.

Comparisons were made between tape cast-PS nickel behaviour and powder pressed-PS nickel behaviour. No differences were observed in strength values or fracture behaviour, hence eliminating the tape casting as a variable in the high strength nickel



(a)



(b)

**Figure 5.22:** (a) yield stress (flexural) versus hardness for ONF-nickel, (b) hardness-grain size dependence for heat treated ONF-nickel.

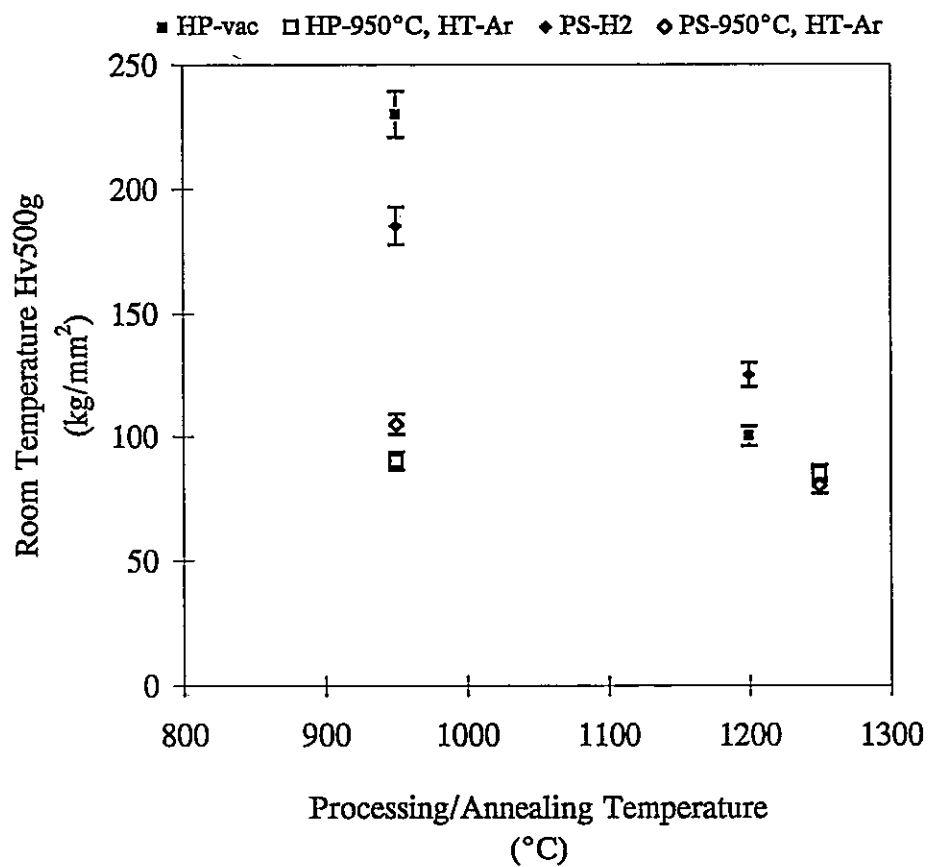


Figure 5.23: The effects of processing and subsequent heat treatment on the hardness of ONF-nickel.

investigation.

#### 5.2.4 Mechanical Properties of Composites

Microhardness and macrohardness was measured for nickel and composite specimens. Hardness measurements of individual phases as well as composite hardness measured for the heat treated composites are displayed in Figure 5.24. The data indicates a work hardened nickel phase within the composites and a composite hardness which is dependent on ceramic fraction. Unfortunately the size of the micro-indentation in the nickel phase of the composites is comparable to the phase dimensions (i.e. a 15 gram load produces indentation of 8 to 13  $\mu\text{m}$  and the largest nickel agglomerate size ranges from 20 to 50  $\mu\text{m}$ ). Thus, microhardness measurements for the nickel phase are erroneously high, yet are still useful for characterization purposes.

Flexural strength, failure strain and hardness values (macro and micro) have been determined for the composite materials following HT-Ar at 950°C. Typical flexure stress-strain curves for these composites, calculated at the tensile surface, are displayed in Figure 5.25a. The curves are all linear to failure, with strains of <0.25%, indicating the absence of macroscopic yield behaviour. Numerous flexure bars were tested at each composite level. The average values, the standard error and the number of tests performed for each grade are shown in Figure 5.25b. The trend indicates that nickel has little influence on composite fracture behaviour up to 75% Ni. In the regime of 75% Ni to 100% Ni, the ceramic phase becomes dispersed with corresponding decrease in flexure strength.

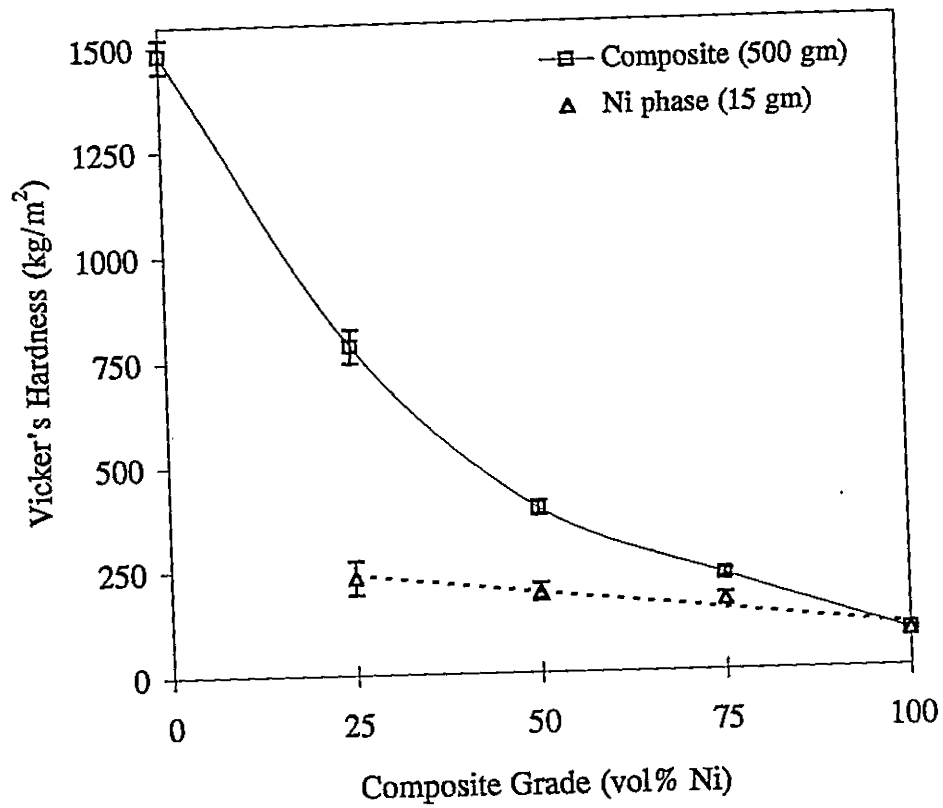
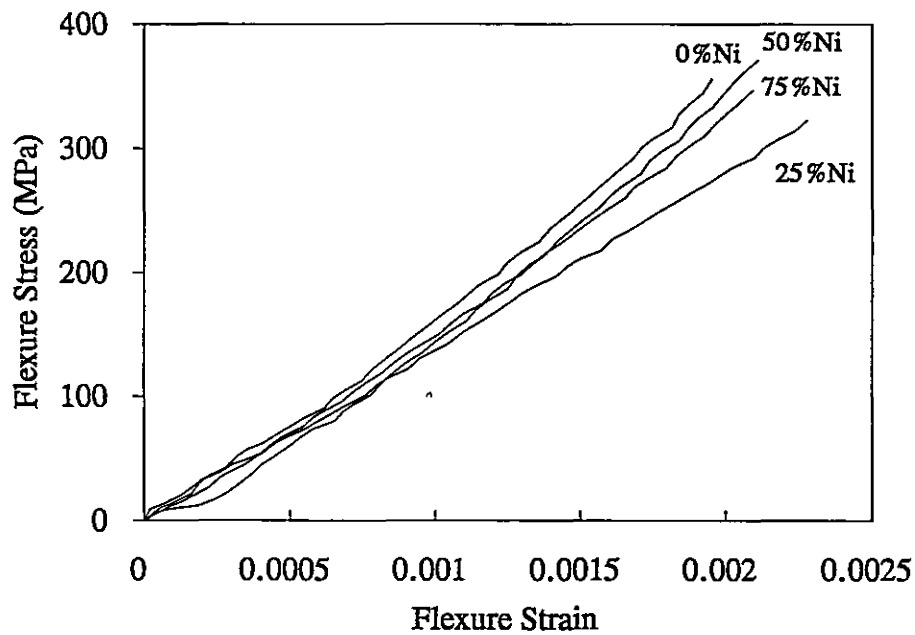
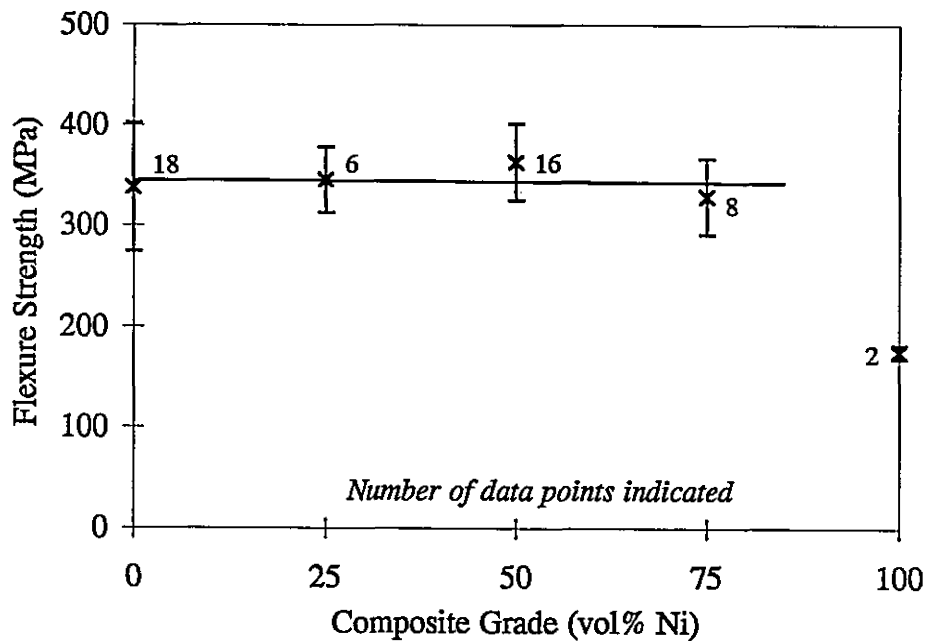


Figure 5.24: Evaluation of composite macrohardness (using 500g load) and nickel phase microhardness (using 15g load) as a function of composite grade.



(a)



(b)

**Figure 5.25:** Flexure test results for Ni:TZ8Y composites, (a) flexure stress-strain profiles, (b) failure strength summary.

## **CHAPTER 6**

### **DISCUSSION**

The objectives of this discussion are four fold: (1) to characterize the processed composite microstructures; (2) to evaluate the solid state powder processing technique developed for M/C composites (based on microstructures developed); (3) to examine the nickel and zirconia materials used in this processing as well as to investigate nickel and zirconia as a suitable model system for M/C FGM development; and (4) to provide insight into nickel/TZ8Y composite (and FGM) properties and mechanical behaviour. To facilitate this discussion, data from the results section, and information from the background and materials processing sections are incorporated.

#### **6.1 Microstructural Characterization of Composites**

The final microstructure of a M/C composite depends on powder characteristics and processing technique. Powder morphology, dispersion characteristics, and sintering behaviour are important parameters of powder characterization. Powder processing in this study includes tape casting and hot pressing steps, both contributing to the final composite microstructure.

### 6.1.1 Powder Dispersion Characteristics

The characteristics of the starting powders, nickel and TZ8Y, were described in Chapter 3 and are seen in green 50:50 composite form in Figure 5.1. Top and bottom tape surfaces (tape drying while in contact with air and glass respectively) exhibit similar features, with no obvious differential settling behaviour. As expected, the bottom surface contains larger pores since tape shrinkage is constrained by the glass substrate. Control of pore size, via appropriate slurry milling procedures (developed in Section 3.2.1.3), to produce fine pore morphology has been used to enhance consolidation. The 50:50 tape morphology shows some apparent tendency for nickel segregation, yet displays good phase dispersion. Phase banding is expected at this grade level due to slurry mixing characteristics which result in phase percolation. The morphology of the tapes depict the spatial distribution of the final laminated composites. Micrographs of consolidated composites (viewed in the transverse plane, i.e. Fig. 5.3a) show similar phase morphologies to that seen in the tapes (Fig 5.1).

### 6.1.2 Composite Phase Morphology

The phase morphologies of M/C composites (Figs. 5.2-5.4) have been quantified (Table 5.1-5.2). Of specific interest are phase scale, dispersion, connectivity, grain size, and microstructural anisotropy. Phase scale and dispersion are related to the powder sizes and tape casting procedures respectively. Microstructural anisotropy can result from both tape casting and hot pressing influences.

### 6.1.2.1 Phase Scale and Dispersion

Although the powder sizes of the metal and ceramic materials are quite different, the scale of ceramic phase is comparable to that of metal phase in consolidated composites (Figs. 5.2-5.4). This is clearly observed in the 25% Ni and 25% TZ8Y micrographs where the mean phase lengths are about 2  $\mu\text{m}$  for the second phase in each image. Similarly, the 50:50 composite micrographs exhibit phase intercept lengths of about 3  $\mu\text{m}$  for both phases. Since the nickel powder size was about 1.9  $\mu\text{m}$  (whereas the ceramic powder size was 0.15  $\mu\text{m}$ ), these observations suggest that: 1) a good phase dispersion has been achieved and 2) the scale of the microstructure is related to the powder size of the larger constituent.

### 6.1.2.2 Phase Connectivity

The microstructures examined in this study (i.e. M:C of 25:75, 50:50, and 75:25) exist as co-continuous phases. The two dimensional photomicrographs are limited in providing a three dimensional prospective and hence do not reveal interconnected morphologies in the 25% metal and 25% ceramic regimes. Electrical conductivity experiments can be used to assess the onset of metal phase percolation. The simplest method to assess whether the material is conductive, is to measure the material's electrical resistance with a multimeter. Pure nickel and zirconia exhibit resistivities of  $6.15 \times 10^{-8}$  ohm-m (Betteridge, 1984a) and  $\geq 10^9$  ohm-m (Brook, 1980) respectively. The 25% Ni composite revealed a resistance value below the detection limit of the measurement apparatus ( $< 0.2$  ohm, or converted to units of resistivity,  $< 1700$  ohm-m),

indicating nickel phase connectivity. Percolation theory indicates that composites containing phases of comparable scale should exhibit percolation at  $\approx 15$  vol% of the minor phase. Since zirconia clusters of approximately the same scale of the nickel phase develops during processing, percolation of zirconia should occur at  $\leq 15$  vol% ceramic. Thus at 25% ceramic, the microstructure must be interconnected.

### 6.1.2.3 Composite Phase Grain Size

Grain size measurements using the line intercept method were performed on the 100% ceramic grade resolving a mean grain length of  $0.24 \mu\text{m}$ . The microstructure indicates normal grain growth. Since the ceramic phase exhibits large phase scale morphology in composites (relative to its initial powder size), it is not surprising to observe a similar ceramic grain size in the composite grades. Nickel, on the other hand, experiences large grain growth tendencies using the processing conditions employed for the composites. However, in the composites, the presence of ceramic phase inhibits nickel grain growth. Although slight variations in nickel grain size is expected for different composite grades, an average nickel grain size of  $3-5 \mu\text{m}$  in composite grade was observed.

### 6.1.2.4 Microstructural Anisotropy

Microstructural anisotropy is observed in comparing transverse microstructures with axial microstructures. Figure 5.5 defines the nomenclature used to describe planar sections and directions in reference to specimen orientation. For purposes of discussion,

the 25% Ni and 25% TZ8Y composites are referred to as "minor phase morphology".

Tape casting may cause phase alignment as a result of shear stresses in the casting direction. Hot pressing facilitates uniaxial shrinkage while preventing radial shrinkage. Since the applied pressure promotes diffusion and slip mechanisms perpendicular to the applied stress, the relative phase separation distances become smaller in the pressing direction (through thickness). Since consolidation results in about 50% axial shrinkage, a first approximation would suggest that transverse phase dimensions would be about twice that of axial section phase morphology. In comparing the morphology in transverse sections with axial sections, it is clear that phase scale is larger in transverse planes. Minor phase morphology exhibits a transverse scale of about 1.3 times that of the axial scale. The 50:50 morphology exhibits a transverse scale of about 1.9 times larger than the axial scale.

Minor phase morphology was assessed by measuring an aspect ratio of second phase particles (i.e. phase length perpendicular to minimum width dimension divided by phase width). Average phase aspect ratios are about 1.7 for transverse sections (in the hot pressing plane) and 1.9 for axial sections. Again the larger aspect ratio in axial sections can be attributed to composite processing influences. In addition, the difference in aspect ratio for nickel is more significant than for zirconia. This may be a consequence of the different sintering and flow behaviours of metal and ceramic phases.

A useful measure of microstructural anisotropy (phase alignment within a planar section) can be achieved by measuring the second phase aspect ratio relative to a specific direction. For the axial section, the through thickness direction sets the phase width

dimension measure, with the length dimension measured perpendicular to the width. For transverse sections, a randomly selected direction was chosen for the length dimension.

Minor phase morphology reveals microstructural aspect ratios of 1.0 in the transverse plane and about 1.5 in the axial plane. Similar observations are apparent with phase intercept measures of 50:50 morphology. This suggests that microstructural homogeneity appears in transverse sections but inhomogeneity (alignment or texturing) appears in axial section morphology. Since tape casting should contribute to alignment in both transverse and axial orientations, while hot pressing should only affect axial, it seems that hot pressing contributes more significantly to the microstructural anisotropy.

## **6.2 Composite Processing Assessment**

Based on the characteristics of tapes, laminates and composites, the processing technique developed is evaluated. The effectiveness of the composite grade selections (i.e. 25% Ni, 50% Ni, and 75% Ni) to adequately represent the full range of structures and behaviour across an M/C FGM profile is addressed.

### **6.2.1 Evaluation of Material Processing**

A detailed description of material fabrication is provided in Chapter 4. The steps include tape casting, lamination, organic burnout, metal oxide reduction and hot pressing. An evaluation is provided for each of these steps.

Tapes have been produced with the necessary qualities of acceptable tapes: homogeneous, crack free, bubble free and agglomerate free. Upon removal of organic

matter, the composite tapes reveal good phase dispersion and fine pore scale (largest pores in composite tapes is approx  $\leq 2 \mu\text{m}$ ). The tape casting procedure implemented is thus adequate to produce quality composite nickel-zirconia tapes.

The organic burnout procedure established (see treatment #14 in Section 3.2.2) supports the pyrolysis and combustion of the tape casting polymers. This procedure ensures sample integrity during organic removal but causes the nickel to oxidize appreciably.

Nickel oxide reduction is effective in Ar-5% $\text{H}_2$ . Using a flow rate of 30 cc/min in a tube furnace (6 cm diameter by 1 m length), oxide reduction is complete after about 12 hours at 450°C. Further reduction time at 450°C results in relatively small further weight loss. Table 3.7 indicates that the oxygen content, in the form of oxide, in reduced green nickel bodies is about 0.25 wt%. Note that thermodynamics supports the oxidation of nickel in air under ambient conditions. At 450°C, there may be an equilibrium level of oxide in the nickel under  $\text{H}_2$  reducing conditions. Therefore it is possible that the nickel powder surface and interior will contain some nickel oxide prior to hot pressing.

Hot pressing of all samples is performed in boron nitride coated graphite dies. The boron nitride coating provides a sufficient barrier to carbon diffusion from the graphite die. Microstructural evidence suggests that the furnace's vacuum is insufficient for consolidating 100% Ni samples without oxide entrapment. Hence the atmosphere in the hot press does not provide a sufficiently low oxygen partial pressure to support the reduction of nickel oxide. The nickel phase in composites, however, does not retain a

nickel oxide structure. This observation is explained in Section 6.3.1 as an influence of improved reduction potential of nickel oxide in the presence of zirconia in vacuum. Therefore, while hot pressing of composites provides acceptable structures, an alternative treatment may be necessary to fabricate 100% metal samples for this study.

### **6.2.2 Composite Grade Selection**

The observation that all composites grades studied exhibit interconnected morphologies suggests a limitation of our composite selection to accurately represent discrete phase morphologies. The flow and fracture characteristics of dispersed and interconnected morphologies are expected to be different. The flexure behaviour of the composites, as compared in Figure 5.25b indicates little influence of nickel volume fraction until in excess of 75% Ni is present. This behaviour is addressed in Section 6.4.3. The exact nature of the composite mechanical response within the regime from 75% Ni to 100% Ni is not clear; however, it is expected that a change from ceramic interconnectivity to ceramic dispersion will result in a substantial reduction in composite strength with increased ductility. It is therefore considered necessary to add a particulate ceramic grade near 10 vol% ceramic to future studies.

### **6.3 Evaluation of Elemental Materials for Composite Development**

Nickel and cubic stabilized zirconia are the constituents selected for this "model system" study of M/C FGMs based on the requirements outlined in Section 3.1.1. This section examines Ni-TZ8Y interfaces, the quality of the elemental selections (ONF-Ni

and TZ8Y-zirconia) to accurately represent nickel and zirconia behaviour, and the compatibility of nickel and zirconia as a model system.

### 6.3.1 Nickel-TZ8Y Interfaces

Transmission Electron Microscopy (TEM) has been employed to investigate the nature of interphase bonding between nickel and TZ8Y following hot pressing. Conventional TEM imaging of nickel-TZ8Y interphase boundaries showed no evidence of an intermediate reaction product between phases. The bonding between nickel and TZ8Y was clean, without nickel oxide phases present. This supports a physical type bonding mechanism, concurrent with observations found in literature (Qin and Derby, 1992; Wagner et al., 1992). Due to the poor vacuum conditions supported by the hot press chamber, one may expect the surface of nickel grains to contain nickel oxide. As previously discussed, 100% Ni samples contain nickel oxide after hot pressing in vacuum. It is known that zirconia reduces its oxygen content on annealing in vacuum (Ruth and Garrett, 1967; Ackermann et al., 1978) which results in a darkening of the ceramic. Qin and Derby (1992) propose that nickel oxide reduction is driven by the absorption of oxygen into the sub-stoichiometric zirconia. It is probable that TZ8Y non-stoichiometry aids in the development of clean Ni/TZ8Y interfaces during hot pressing.

In thinned regions of TEM specimens, interphase cracks are common. Thicker regions show less tendency for interfacial decohesion. Phase separation in composites may result from residual stresses developed as a consequence of CTE mismatch of the constituent phases. Thin sections exhibit reduced constraint, hence debonding is enabled.

Nickel/zirconia interface strengths, measured from flexure bars of diffusion bonded nickel foils on zirconia substrates, have been reported (Qin). Average bond strengths of 150  $\mu\text{m}$  thick nickel foils were measured to be about 80 MPa. Thicker foils showed lower strengths. These tests indicate that failure is controlled by the constrained plastic deformation of the metal foil layer. A thinner foil exhibits higher constraint hence will experience a larger failure stress. The significance of this data is that the bonding strength between nickel and zirconia is low (about half the yield strength of commercially pure nickel). Therefore in the absence of microstructural tortuosity and interconnectivity, phase separation at low stress (applied or residual) is likely. In our composites, as discussed in Section 6.4.2, high residual stresses and appreciable metal phase hardening is observed which suggests, in contrast, that residual stresses are not relaxed by interfacial decohesion.

### 6.3.2 ONF Nickel Evaluation

To understand the properties and behaviour of composite materials it is first necessary to understand the behaviour of the elemental materials, from which the behaviour within the composites can be based. Literature sources have been reviewed pertaining to these issues (see Section 2.5). Unfortunately the nickel implemented in this study exhibits atypical properties and behaviour. A variety of processing and subsequent heat treatments have been conducted in attempts to understand the ONF-nickel behaviour. From these tests and microhardness evaluations nickel behaviour within the composites has been characterized. This section describes the results attained from nickel

investigation.

Pure annealed nickel (large grain size) should exhibit a yield strength  $\leq 140$  MPa, elongation of about 50% and a hardness of about 90 kg/mm<sup>2</sup>. There are a limited number of strengthening methods applicable to sintered nickel including contributions from: solid solution alloying, grain size refinement, and particle dispersions. For the impurity level in the as processed nickel specimens (see Table 3.2 for substitutional elements ( $>0.25$  wt%) and Table 3.7 for carbon in processed nickel (0.01 wt%)) very little contribution is expected from solid solution strengthening (be that substitutional like iron or interstitial like carbon). Using Hall-Petch data for nickel ( $k=0.1$  MPa m<sup>-1/2</sup>), an increase in yield strength of about 70 MPa is expected for grain sizes in the order of 2  $\mu\text{m}$ . As discussed previously, particle dispersions are present in all nickel specimens. Vacuum hot pressed samples exhibit nickel oxide particles while hydrogen sintered samples contain Ni<sub>3</sub>Al particles. Many of these particle lie along nickel grain boundaries. The interparticle spacing is estimated to be in the order of about 0.3  $\mu\text{m}$ . However, many grains viewed did not reveal particles. The Orowan contribution from such spacings is only about 50 MPa. Combining these sources of strengthening provide an upper bound for the nickel yield strength of  $\approx 250$  MPa.

Nickel processed at 950°C in this study exhibits very high yield strengths:  $\approx 600$  MPa and  $\approx 800$  MPa for pressureless sintered (PS-H<sub>2</sub>) and hot pressed (HP) nickel respectively. Subsequent heat treating at 950°C in argon gas (HT-Ar) reduces these strengths to levels of 180 MPa and 200 MPa respectively. Since the grain size in these materials is in the order of the initial powder size, the heat treated strengths are

acceptable for fine grained nickel. Reduced strengths (hardness), concurrent with increased grain size, are observed for the heat treated nickel as shown in Figure 5.22b. Translating the slope in this relationship into units of yield stress (via a calibration of hardness\*9.81/3) yields a  $k \approx 0.15 \text{ MPa m}^{-1/2}$ , which is comparable to that observed of typical nickel. HP nickel after HT-Ar at 950°C results in low ductility and intergranular fracture as shown in Figures 5.20b and 5.13b respectively. There are numerous particles along the grain boundaries in this material which possibly contributes to the higher yield strength via dislocation pinning events. Note that fracture occurs prior to true yielding in this material.

The cause of the high strength ONF-nickel, in the as processed condition, is yet unknown. It is possible that hydrogen may tie up impurities within the grains or within the grain boundaries resulting in the observed behaviour. Both the HP material and PS material are exposed to H<sub>2</sub> during reduction treatments. Since the vacuum in the hot press is poor, this hydrogen may remain trapped in the nickel at 950°C, as it is in the PS material. The higher strength in the HP material may be due to the oxide volume fraction which is in the order of 4%. The fracture surfaces for the as processed materials are very similar (see Fig. 5.12). Upon HT-Ar, hydrogen is removed from the specimens with a corresponding reduction in hardness. Much less twinning also results. If the material is then retreated in hydrogen, the strength remains at the reduced level. It is unknown why such differences in fracture behaviour occur between PS and HP nickel following HT-Ar at 950°C.

Nickel processed at  $\approx 1200^\circ\text{C}$  delivers hardness values approaching that of typical

nickel, although the PS-H<sub>2</sub> hardness remains rather high (see Fig. 5.23). This suggests that higher temperatures reduce the effects of hydrogen during HP, while PS-H<sub>2</sub> causes a retention of hydrogen effects. It is possible that the hydrogen infected material exhibits a much larger grain size dependence than typical nickel.

The HT nickel appears to exhibit a very high work hardening rate. PS nickel, after HT-Ar at 950°C had an initial hardness of 105 kg/mm<sup>2</sup> which was increased to 160 kg/mm<sup>2</sup> following ≈4% tensile flexural strain. Converting hardness to yield stress gives a hardening rate of ≈E/50, which is very high for any material. An average work hardening rate in commercial nickel is ≈E/300. It is unknown what causes this high observed hardening rate. This high hardening rate is consistent with the low ductility at fracture for all nickel samples.

From the results of the various heat treatments, the behaviour of the nickel in elemental form has been examined. The fundamental cause of the high strength behaviour is not understood. It is expected that impurities in the nickel, namely Al, Fe and possibly Ti and S contribute, along with interaction with hydrogen, to cause this behaviour. It is recommended that future work employ a high purity nickel with well characterized and consistent behaviour.

### 6.3.3 Cubic phase stability in TZ8Y

The zirconia powder selected for this study is expected to provide a solid solution of cubic stabilized zirconia when processed in the cubic phase field as shown in Figure 6.1. On cooling below 1000°C, a two phase regime exists in equilibrium. Since cation

volume diffusion is very slow in zirconia at these temperatures (i.e.  $D_{Zr} \leq 10^{-15} \text{ m}^2/\text{s}$ , Brook 1980) phase separation is not expected upon cooling. TEM observations of hot pressed 100% ceramic specimens clearly reveals single phase cubic zirconia (Fig. 5.8). However, observations of the ceramic component in a 50:50 composite indicates the presence of two ceramic phases (Fig. 5.9). Since the phases have approximately the same grain size, and diffusion upon cooling is unlikely, two cubic phases were likely stable while at 1250°C. Upon cooling, grains with less than the nominal yttria content transformed to tetragonal with stress accommodation through the formation of twins.

This difference in ceramic microstructure between composites and 100% ceramic samples is not fully understood. A possible explanation is that nickel or its impurities act to stabilize the yttria phase at 1250°C. Hence a driving force results in the diffusion of yttrium and zirconium ions to form separate grains.

#### 6.3.4 Nickel and TZ8Y as a Model System

The problems observed in the ONF nickel can be alleviated via its replacement with a high purity nickel powder. Interfaces are clean hence satisfying that requirement. The outstanding issue concerns the stability of TZ8Y in the presence of nickel. Future studies must examine this effect with high purity nickel. If destabilization still occurs, the choice of nickel-TZ8Y as a model system will require reconsideration.

#### 6.4 Composite Properties and Behaviour

Prior to characterization, the composites were heat treated to deliver nickel phase

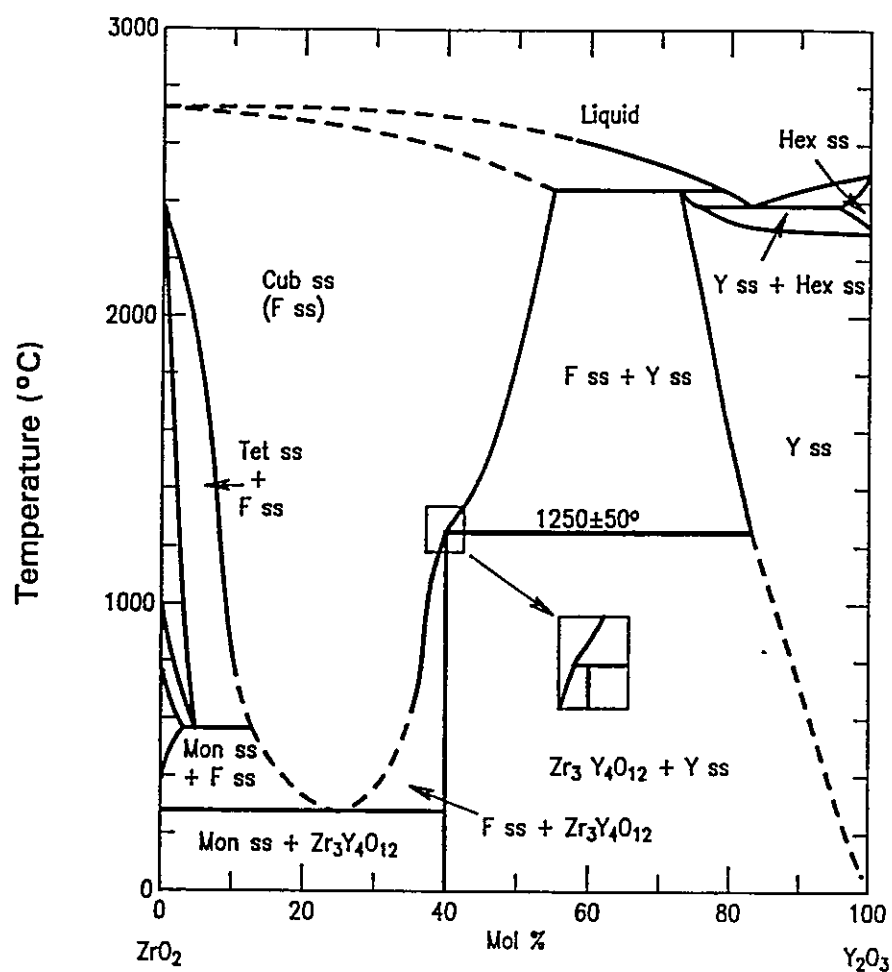


**Figure 6.1:**  $ZrO_2$ - $Y_2O_3$  phase diagram. F = fluorite type of  $ZrO_2$ ; Y =  $Y_2O_3$ ; Cub = cubic; Tet = tetragonal; Mon = monoclinic; Hex = hexagonal. (From Roth, Dennis and McMurdie, 1987).

characteristics similar to that of heat treated, pressureless sintered nickel. The thermal dilation dependence, elastic properties and mechanical behaviour is discussed for the composite materials. Thermal and elastic data are useful in describing the residual stress states within the composites. This account, along with composite mechanical response, aids in the understanding of composite flow and fracture. Continuum mechanics seems most appropriate for the modelling of M/C FGM mechanical behaviour.

#### 6.4.1 Thermal/Elastic Properties

Room temperature elastic properties were measured for all samples (Fig. 5.18). In agreement with published data (Table 3.3), the moduli for nickel and zirconia at room temperature are similar. As expected, the measured composite moduli are also comparable to the constituent materials. The composite moduli may be a bit low on average due to higher porosity levels.

The effect of temperature on elastic properties has not been assessed. However, it is expected that due to zirconia's high melting temperature, its modulus will change very little within the temperature range of 25-1250°C. Alternatively the modulus for nickel is expected to decrease markedly upon increasing temperature. For instance the modulus of Nickel 201 (low carbon grade) decreases approximately linearly from about 200 GPa at room temperature to 160 GPa at 700°C (Betteridge, 1984b).

The thermal expansion characteristics observed for ONF nickel and TZ8Y are typical of these materials. Figure 5.19b illustrates the CTE-temperature dependence for the composites. As expected, the pure nickel shows a large CTE-T dependence whereas

zirconia shows a smaller dependence over the temperature range of 25-1200°C. The dilation curves for composites range between those for zirconia and nickel (Fig. 5.19a). Composite dilation tends to be influenced more significantly by the presence of zirconia (i.e. all composite curves lie closer to the zirconia curve and CTE for the composites at high temperatures approach that of 100% TZ8Y). This is likely the result of nickel flow and stress relief within the composites at higher temperatures. Conversely the nickel phase appears to dominate the dilation at low temperatures.

#### 6.4.2 Composite Residual Strain/Stress Assessment

The thermal dilation compilations, along with the elastic moduli data, can be used to assess the residual stress levels as a function of composite grade. It will be shown that for the composite grades examined, the nickel phase has yielded during the course of composite thermal dilation. The residual elastic stress of the nickel phase within the composites therefore represents the metal phase flow stress (i.e. work hardened yield stress). The following analysis compares a continuum approach, based on thermal dilation data, with a micromechanics approach, using Humphreys' model, to describe the flow stress of the metal phase within a composite. Since the residual components of stress within a composite are necessarily balanced, the residual elastic strains in the metal ( $m$ ) and ceramic ( $c$ ) are related via:

$$\epsilon_m = \frac{f_m - 1}{f_m} \epsilon_c, \quad [6.1]$$

where  $f_m$  is the metal phase fraction.

A continuum approach can be developed based on the thermal-residual-elastic strains in the composite. Note that nickel annealing is accomplished during the 950°C heat treatment employed on the composites. Therefore at 950°C we start with zero strain in each phase. As a first approximation, we can assume that both phases behave elastically while under thermal strain. Since the composite grades exhibit interpenetrating phases, a simple slab model can be applied. To further simplify the analysis we can treat the modulus of the composites as a constant at a value of about 210 GPa since there is very little dependence on composition. The modulus of nickel does decrease with temperature; but for simplicity it is assumed constant. The elastic strain developed within the metal phase as a function of metal phase fraction, imposed temperature change ( $\Delta T$ ) and CTE mismatch is then:

$$\epsilon_m = (1 - f_m) \Delta T \Delta(CTE_{m-c}). \quad [6.2]$$

The stress corresponding to this elastic strain can be approximated by  $\sigma = \epsilon E$ .

Using the dilation data measured from nickel and TZ8Y under  $\Delta T = 925^\circ\text{C}$ , the elastic model for residual stress within the nickel phase as a function of composition is shown in Figure 6.2. This curve provides the upper bound to the residual stress developed with the nickel phase. Since fine grained nickel has a yield stress of about 200 MPa this analysis indicates that nickel phase yielding will begin in composites containing  $\geq 20\%$  ceramic. Therefore all the composite grades studied will exhibit nickel phase yielding.

Accounting for metal yielding in this model is rather trivial since the ceramic

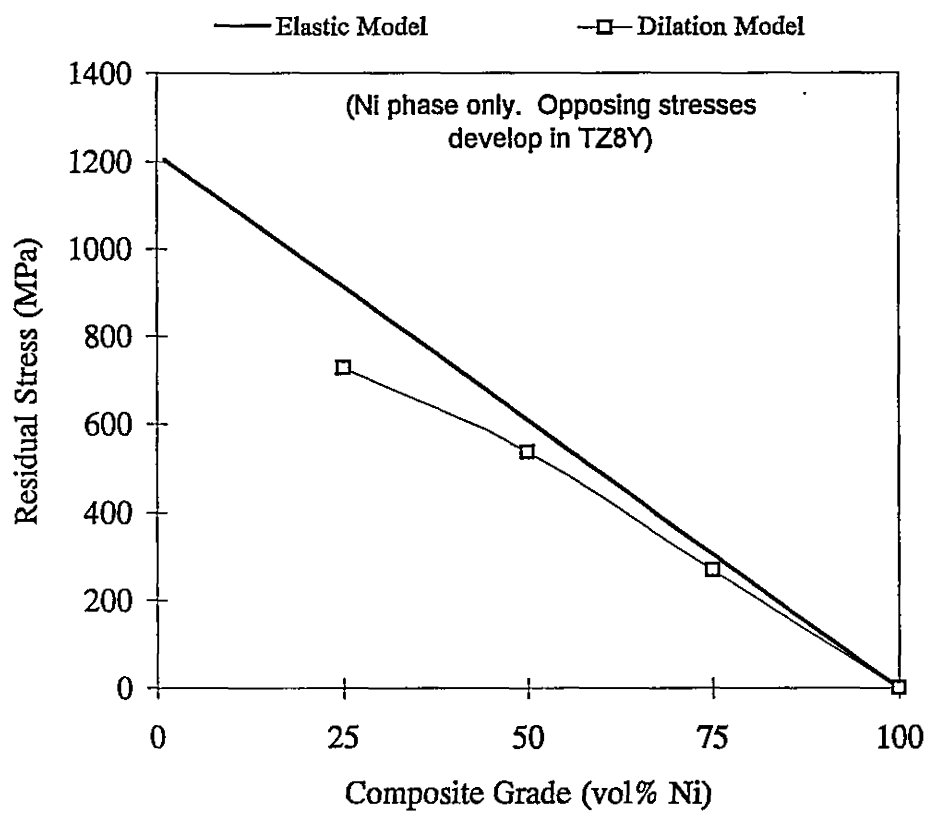


**Figure 6.2:** Residual stress dependence in Ni: TZ8Y composites calculated via continuum mechanics.

behaviour remains elastic. If the elastic strain of the ceramic phase within a composite can be measured, then the elastic strain within the metal phase may be inferred (from Eqn. 6.1) and hence the resulting residual stress components can be estimated. A consolidated body containing open porosity exhibits the same thermal dilation as a fully dense body, since gas has zero modulus. Therefore the difference in dilation between a composite and 100% TZ8Y yields the level of elastic strain within the ceramic as:

$$\epsilon_c = \Delta T \Delta (CTE_{c-comp}). \quad [6.3]$$

The corresponding nickel residual stress is represented by the dilation model in Figure 6.2. As expected, due to plastic flow of the nickel, this curve lies below that of the elastic model, yet still indicates very high values of nickel phase residual stress in composites containing  $\geq 25\%$  ceramic. This requires a high degree of nickel work hardening, in agreement with that observed for ONF-nickel (see Section 6.3.2).

Since the residual stresses exceed the annealed nickel yield strength ( $\approx 210$  MPa), the elastic model and the dilation model can be replotted in terms of  $\sigma_{flow}$  (Figure 6.3). Note that the flow stress behaviour in the nickel rich regime ( $> 75\%$  Ni) is approximately equal to that of annealed nickel. Representation in this way enables a direct comparison to Humphreys' model and hardness data.

For a micromechanics approach we can apply the yield stress model developed in Section 2.3.2 which incorporates the effects of dislocation generation due to CTE mismatch, via Humphreys' model and includes the Hall-Petch grain size dependence. Since particles are not observed within the nickel phase in the composites, the Orowan

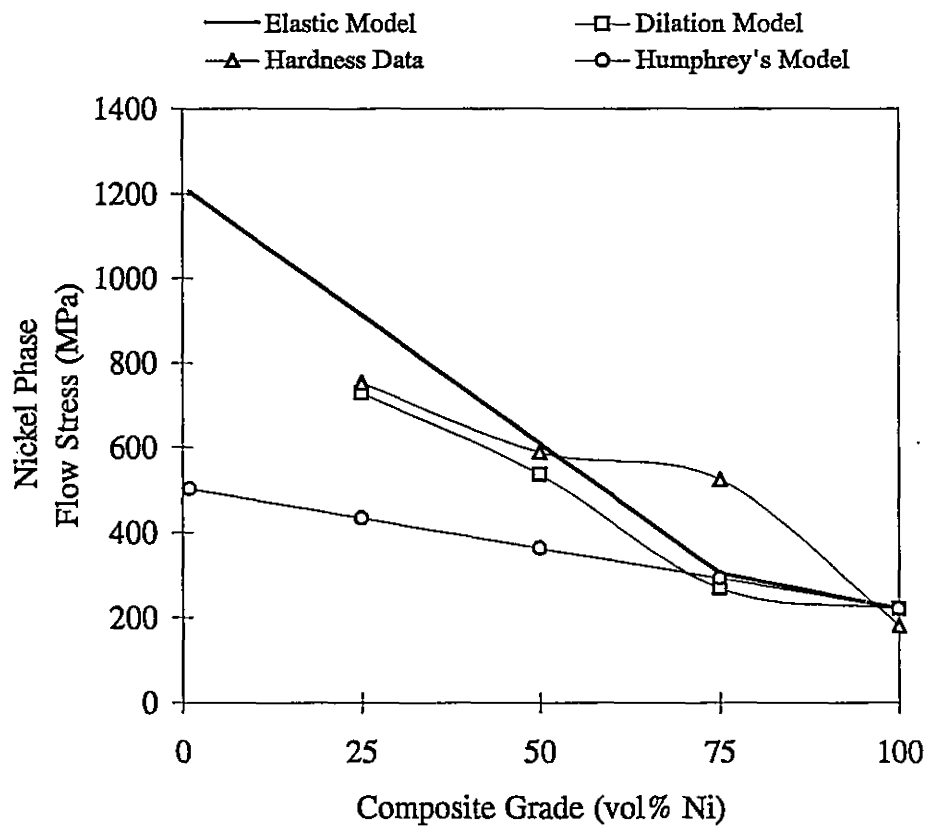


Figure 6.3: Comparison of various models to predict nickel phase flow stress within Ni:TZ8Y composites.

contribution is zero. Implementing typical parameters for nickel, with  $\alpha=1$ , the diameter of ceramic reinforcement equal to the phase intercept length ( $\approx 2 \mu\text{m}$ ) and the nickel grain size of about  $2 \mu\text{m}$ , equation 2.5 gives:  $\sigma_{ys}=210+275f_c$ . This equation is plotted as "Humphreys' model" in Figure 6.3. In comparison with the continuum models, Humphreys' model shows a very weak stress-phase fraction dependence. Note that Humphreys' model was developed for dispersed particulate composites with an inherent assumption that dislocation fields around particles do not interact. The model also involves a scale dependence which is not appropriate for interconnected systems. The model assumes a matrix material exhibiting low work hardening rates.

The microhardness of the nickel phase within the composites (see Figure 5.24), converted to an approximate yield stress using Figure 5.22a, provides the "hardness data" curve in Figure 6.3. These values are somewhat overestimated for the reason described in Section 5.2.4. Nevertheless, both the dilation model and the hardness data reveal dependencies approaching that of the elastic model.

Humphreys' model is analytically based and involves assumptions that are not appropriate for interconnected composite systems, whereas the continuum model is supported empirically by the dilation data. In addition the hardness data supports the results of the dilation model. It is therefore expected that continuum based modelling may best describe the residual/flow stress development within interconnected M/C composites.

### 6.4.3 Composite Mechanical Behaviour

Figure 5.24 shows that composite hardness is dependent on ceramic volume fraction, while Figure 5.25b indicates that flexure strength is insensitive for composites containing  $\geq 25$  vol% TZ8Y. The flexure behaviour for materials containing between 0% and 25% TZ8Y exhibit an increasing strength profile, which is likely linked to phase percolation as discussed in Section 6.1.1.

The composite hardness is expected to show the observed dependence, since hardness indentation is a compressive technique. Due to the compressive load bearing characteristics of ceramics, it is expected that compressive yield will be a strong function of ceramic fraction, especially for interconnected ceramic morphologies. This dependence of compressive behaviour indicates that a stress partitioning model, supported within the framework of continuum mechanics, may be suitable for this modelling.

Although composite hardness can be used to define composite yielding, it is not appropriate to describe composite tensile performance. Ceramics exceed their fracture strength prior to yielding in tension. The tensile response of a M/C composite is dominated by the ceramic fracture strength (provided that the ceramic phase is interconnected). Upon fracture of the ceramic phase, metal phase rupture immediately follows.

Evaluation of fracture surfaces aids in the understanding of composite behaviour under tensile related failure. Fracture surfaces for the composite grades are contained in Figures 5.15-5.17. The 25% Ni grade exhibits nickel phase pull-out, decohesion and microscale ductility. The ceramic phase is certainly brittle and appears transgranular.

The 50% Ni composite indicates decohesion and nickel ductility along with brittle zirconia behaviour. The 75% Ni surface shows features which are difficult to identify. It is expected that decohesion of the interconnected phases contributes significantly to the fracture appearance. Fracture of the nickel phase within the composites does not indicate a microvoidal coalescence mode. Ductile rupture of the nickel indicates that the ceramic phase fractures first followed by the rupture and decohesion of the nickel phase.

Modelling composite flexure behaviour is complicated by triaxiality of residual stresses, metal yielding and specimen loading geometry. Composite flexure curves are linear to failure suggesting the absence of significant damage accumulation during loading. Therefore the evaluation can be focused toward the tensile surface where catastrophic failure initiates. Prior to composite flexure testing, the nickel phase is highly work hardened and exhibits a flow stress equal to its residual stress. Since very little macroscopic strain is induced at failure in flexure ( $\approx 0.2\%$ ), nickel deformation must occur with little increase in nickel flow stress. Therefore nickel plasticity occurs upon initial loading, while the ceramic begins to relax its elastic compressive stress. The nickel maintains the same loading capacity while the ceramic releases its compressive load and gradually attains tensile load. Failure ensures once the stress in the ceramic reaches a critical value. This idea is illustrated in the schematic of Figure 6.4. Using this analysis, the composite fracture strength may be written in the form of a stress partitioning model as:

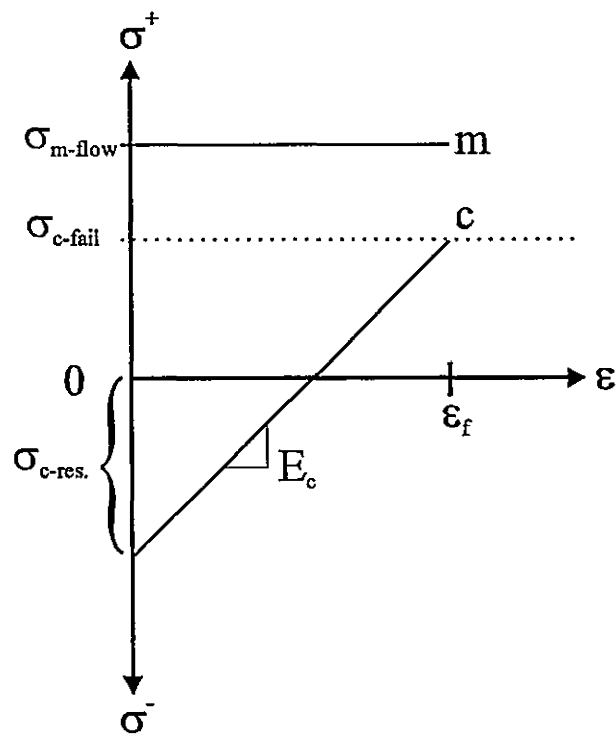


Figure 6.4: Schematic of proposed flow and fracture response of Ni:TZ8Y composites.

$$\sigma_{fracture} = (1-f_c)\sigma_{m-flow} + f_c\sigma_{c-fail} \quad [6.4]$$

where  $\sigma_{m-flow}$  (metal phase flow stress) is a function of the residual stress conditions imposed upon it due to thermal dilation (as illustrated in Figure 6.3) and  $\sigma_{c-fail}$  (ceramic phase failure stress) is dependent on the tensile strength of the ceramic phase.

This model assumes phase fraction partitioning of stress to provide composite strength. The fracture data in Figure 5.25b indicates little dependence of phase fraction on composite strength. Assuming the ceramic phase strength is independent of metal phase fraction requires the metal phase flow stress to be independent of phase fraction and similar to the strength of the ceramic. This implies lower metal phase flow stresses than those predicted in Section 6.4.2.

Note however that this model is largely simplified in that it ignores effects of stress concentrators and microstructural damage such as M/C decohesion prior to composite fracture. Also the existence of dual phase zirconia within the composites further complicates the evaluation of ceramic failure criteria. Nevertheless, by using the above assumptions, the strength of the interpenetrating composites seems to obey continuum mechanics.

## CHAPTER 7

### SUMMARY AND CONCLUSIONS

This study provides a preliminary investigation into the development, microstructural characterization, properties and behaviour of solid state powder processed M/C composites. Nickel and cubic stabilized zirconia (containing 8 mol%  $Y_2O_3$ ) were selected model system candidates for this investigation. The results of this work will be fundamental to future development, characterization, and modelling of M/C FGMs. The conclusions resulting from this study are outlined below.

A processing technique has been developed which includes tape casting, lamination, binder burnout, metal oxide reduction, and hot press consolidation steps. The technique provides well dispersed, homogeneous, dense composites. The hot pressing environment is insufficient in consolidating 100% nickel without nickel oxide entrapment.

Processing characteristics produce metal and ceramic phase scales dependent on the size of the larger constituent (i.e. the fine ceramic powder clusters to interstitial and vacancy regions in nickel packing, resulting in similar phase sizes). Characterization of composite microstructures (e.g. 25% Ni, 50% Ni, and 75% Ni) identified all composites as interpenetrating structures. Phase percolation in this system is expected to conform

to the range established for approximately equal size phase mixtures ( $\approx 15$  vol% second phase). It is recommended, in future studies, to add a composite grade within the particulate M/C composite regime (i.e.  $\approx 5-10$  vol% ceramic) to enable a full characterization of the structure and properties of M/C FGMs.

An evaluation of the elemental materials implemented in this study showed that the nickel used is inadequate for this study. A high purity nickel should be considered as a replacement for the ONF grade used. Since reasonably understood nickel behaviour results following a heat treatment in argon gas at  $950^{\circ}\text{C}$ , all composite grades evaluated were too treated under these conditions. This enabled mechanical characterization of the composites.

Transmission electron microscopy was used to examine the atomistic interactions between nickel and zirconia in the composites. The resulting metal/ceramic interfaces are atomically clean (i.e. without a reaction product). There is concern regarding the stability of the cubic zirconia phase when processed along with nickel. Hot pressing 100% TZ8Y produces cubic stabilized zirconia while hot pressing nickel-TZ8Y composites yields two ceramic phases (tetragonal zirconia and cubic yttria). It is therefore necessary to re-evaluate model system selection for the M/C FGM study.

The thermal dilation and elastic properties as a function of composite grade were examined. Since nickel and zirconia exhibit similar elastic properties, a very weak dependence on composite grade results. Thermal dilation data was used to determine the coefficient of thermal expansion versus temperature and composite grade. Thermal dilation data and elastic properties enable a quantification of composite thermal-residual

stresses.

In light of the residual stress state within the composites, the tensile behaviour (from flexure evaluation) of the composites was characterized. Flexure strength shows a very weak dependence with metal volume fraction between 0% and 75% Ni. The nickel phase, being highly work hardened prior to flexure testing, bears little additional load during flexure testing. The ceramic phase thus bears the flexure load and controls the onset of composite fracture. In contrast to flexure response, composite hardness shows a strong dependence on ceramic phase fraction due to a ceramic's high compressive strength.

Based on the results attained and the analyses performed in this study, it is expected that continuum mechanics will provide the fundamental basis for the mechanical modelling of M/C FGMs.

## REFERENCES

- Ackermann, R., Garg, S., and Rauh, E., *J. Am. Ceram. Soc.*, **61**, p.275, 1978.
- Adamson, A., "Physical Chemistry of Surfaces", New York, *Interscience*, 1960.
- Arsenault, R., *Scripta metall. mater.*, **25**, p.2617, 1991.
- Ashby, M., "Strengthening Methods in Crystals", eds. A. Kelly, and R. Nicholson, Applied Science Publishing Ltd, 1971.
- Betteridge, W., "Nickel and its Alloys", Ellis Horwood Ltd. p.16, 1984a.
- Betteridge, W., "Nickel and its Alloys", Ellis Horwood Ltd. p.66, 1984b.
- Boch, P. Chartier, T., and Huttepain, M., "Tape Casting of Al<sub>2</sub>O<sub>3</sub>/ZrO<sub>2</sub> Laminated Composites Loaded at various Mechanical Arrangements", *Science of Ceramics*, **14**, p.638-44, 1988.
- Braun, L., Morris, J., and Cannon, W., *Am. Ceram. Soc. Bull.*, **64**, p.727-29, 1985.
- Brook, R.J. "Preparation and Electrical Behaviour of Zirconia Ceramics", *Science and Technology of Zirconia*, **3**, p.273-85, 1980.
- Burkin, A., "The Chemistry of Hydrometallurgical Processes", E. & F.N. Spon Ltd., p.1-5, 1966.
- Cannon, W.R., Becker, R., and Mikeska, K.R., "Interactions Among Additives Used for Tape Casting", *Advances in Ceramics*, **26**, p.525-41, 1989.
- Chartier, T., Streicher, E., and Bock, P., "Phosphate Esters as Dispersants for the tape casting of Alumina", *ACS Bulletin*, **66**, [11], p.1653-55, 1987.
- Chen, I. and Argon, A., *Acta metall.*, **27**, p.785, 1979.
- Cima, M.J. and Lewis, J.A., "Firing Atmosphere Effects on Char Content from Alumina Poly(Vinyl Butyral) Films", *Ceramic Transactions*, **1**: Ceramic Powder

Science II, p.567-74, 1988.

Cobel, R.L. and Ellis, S., *J. Am. Ceram. Soc.*, **46**, p.438, 1963.

Coble, R.L., in "Sintering and Related Phenomena", eds. G.C. Kuczynski, N.A. Hooten and C.F. Gibbon, p.329, 1967.

Cox, H., "The Elasticity and Strength of Paper and other Fibrous Materials", *Brit. J. Appl. Phys.*, p.73-9, 1952.

*CRC Handbook of Materials Science, II: Materials, Composites, and Refractory Materials*, p.358, 1985.

Eshelby, J., "The Determination of the Elastic Field of an Ellipsoidal Inclusion and Related Problems", *Proc. Roy. Soc.*, **A241**, p.376-96, 1957.

Fan, Z., Tsakiropoulos, P., and Miodownik, A., "A Generalized Law of Mixtures", *J. Mat. Sci.*, **29**, p.141-50, 1994.

FGM Forum, "Survey for Application of FGM's", *The Society of non-Traditional Technology*, Tokyo, 1991.

Finnis, M., Stoneham, A., and Tasker, P., in "Metal-Ceramic Interfaces," eds. M. Ruhle, A. Evans, M. Ashby, and J Hirth, p.35, 1990.

Finnis, M., *Acta metall. mater.* **40**, p.525, 1992.

Fukuda, H. and Chou, T., "An Advanced Shear Lag Model Applicable to Discontinuous Fibre Composites", *J. Comp. Mat.*, **15**, p.79-91, 1981.

Gilchrist, J., "Extraction Metallurgy", 3rd edit. Pergamon Press, p.276-85, 1989.

Holt, J.B., Koizumi, M., Hivai, T., and Muniv, Z, *Ceramic Transactions*, **34**: Functionally Gradient Materials, Preface, 1993.

Howatt, G., Breckenridge, J., and Brownlow, J., *J. Am. Ceram. Soc.*, p.237-42, 1947.

Howe, J., "Bonding, Structure, and Properties of Metal/Ceramic Interfaces", *Int. mat. rev.*, **38**, [5], p.234-36, 1993.

Humphreys, F., *Proc. of the 9th Riso Inter. Sym.*, eds. S.I. Andersen, H. Lilholt, and O. Pedersen, p.51-74, 1988.

- Humphreys, F., Basu, A., and Djazeb, M., *Proc. of 12th Riso Inter. Sym.*, eds. N. Hansen, D. Jensen, T. Leffers, H. Lilhelt, T. Lorentzen, A. Pedersen, O. Pedersen, and B. Ralph., p.51-66, 1991.
- Johnson, K. and Pepper, S., *J. Appl. Phys.*, **53**, p.6634, 1982.
- Kaysser, W. and Ilchner, B., "FGM Research Activities in Europe", Functionally Graded Materials, *MRS Bulletin*, **XX**, [1], p.22-5, 1995.
- Kim, D. and Tien, T., "Phase Stability and Physical Properties of Cubic and Tetragonal  $ZrO_2$  in the System  $ZrO_2$ - $Y_2O_3$ - $Ta_2O_5$ ", *J. Am. Ceram. Soc.*, **74**, [12] p.3061-65, 1991.
- Koizumi, M., "Recent Progress of Functionally Graded Materials in Japan", *Ceramic Engineering and Science Proceedings*, p.333-347, 1992.
- Koizumi, "The FGM Concept", *Ceramic Transactions*, **34: Functionally Gradient Materials**, p.3-20, 1993.
- Kuroda, Y., Kusaka, K., Moro, A., and Jogawa, M., "Evaluation Tests of  $ZrO_2$ /Ni Functionally Gradient Materials for Regeneratively Cooled Thrust Engine Applications", *Ceramic Transactions*, **34: Functionally Gradient Materials**, p.289-96, 1993.
- Lenel, F.V. and Ansell G., in "Sintering and Related Phenomena" eds. G.C. Kuczynski, N.A. Hooten and C.F. Gibbon, p.351, 1967.
- Markworth, A. and Saunders, J., "A Model of Structure Optimization for a Functionally Graded Material", *Materials letters*, **22**, p.103-7, 1995.
- Markworth, A., Ramesh, K., and Parks, W., "Modelling Studies Applied to Functionally Graded Materials", *J. Mat Sci.* **30**, p.2183-93, 1995.
- Meyers, M. and Chawla, K., "Mechanical Metallurgy: Principles and Applications", Prentice-Hall, p.360, 1984.
- Mikeska, K. and Cannon, W.R., "Dispersants for Tape Casting pure Barium Titanate", Forming of Ceramics, *Advances in Ceramics*, **9**, p.164-83, 1964.
- Miller, W., and Humphreys, F., "Strengthening Mechanisms in Metal Matrix Composites", in *Fundamental Relationships between Microstructure and Mechanical Properties of Metal-Matrix Composites*, ed. Liaw and Gunger, TMS, p.517-41, 1990.

Mistler, R.E., Shanefield, D.J., and Runk, R.B., "Tape Casting of Ceramics", *Ceramics Before Firing*, p.411-88, 1978.

Moreno, R., "The Role of Slip Additives in Tape Casting Technology: Part 1 - Solvents and Dispersants", *ACS Bulletin*, **71**, [10], p.1521-31, 1992.

Morris, J.R., "Organic Component Interactions in Tape Casting Slips of Barium Titanate", Ph.D. dissertation, Rutgers University, Piscataway, NY, Oct. 1986.

Morris, J.R. and Cannon, W.R., "Rheology and Component Interactions in Tape Casting Slurries", *Mater. Res. Soc. Symp. Proc.*, **60**, p.135-42, 1986.

Murr, L., "Interfacial Phenomena in Metals and Alloys", p.34, 1975.

Nan, C., Yuan, R., and Zhang, L., "The Physics of Metal/Ceramic Functionally Graded Materials", *Ceramic Transactions*, **34**: Functionally Gradient Materials, p.75-82, 1993.

Nan, C., "Physics of Inhomogenous Inorganic Materials", *Prog. Mater. Sci.*, **37**, p.1-116, 1993.

Niino, M. and Maeda, S., "Recent Development Status of Functionally Graded Materials", *ISIJ International*, **30** [9] 699-703, 1990.

Plucknett, K.P., Caceres, C.H., and Wilkinson, D.S., "Tape Casting of Fine Alumina/Zirconia Powders for Composite Fabrication", *J. Am. Ceram. Soc.*, **77**, [8] p.2137-44, 1994.

Qin, C. and Derby, B., "Diffusion Bonding of Nickel and Zirconia: Mechanical Properties and Interfacial Microstructures", *J. Mater. Res.*, **7** [6], p.1480-89, 1992.

Rabin, B.H. and Heaps, R.J., "Powder Processing of Ni-AL<sub>2</sub>O<sub>3</sub> FGM", *Ceramic Transactions*, **34**: Functionally Gradient Materials, p.173-80, 1993.

Richerson, D.W., "Modern Ceramic Engineering: Properties, Processing and Use in Design", 2nd. edit., p.519-45, 1992.

Roosen, A., "Basic Requirements for Tape Casting of Ceramic Powders", *Ceramic Transactions*, **1**: Ceramic Powder Science II, p.675-92, 1988.

Rossi, R.C. and Fulrath, R.M., *Ibid.*, **49**, p.558, 1965.

Roth, R., Dennis, J. and McMurdie, H., "Phase Diagrams for Ceramists", **6**, 1987.

- Ruhle, M. and Evans, A., "High Toughness Ceramics and Ceramic Composites", *Prog. Mat. Sci.*, **33**, p.85-167, 1989.
- Ruth, R. and Garrett, H., *J. Am. Ceram. Soc.*, **50**, p.257, 1967.
- Sasaki, M., and Hirai, T., "Fabrication and Properties of Functionally Gradient Materials", *J. Ceram. Soc. Jpn.*, **99**, [10] p.1002-13, 1991.
- Schonberger, U., Andersen, O., and Fessel, M., "Bonding of Metal-Ceramic Interfaces; AB INITIO Density-functional Calculations for Ti and Ag on MgO", *Acta metall. mater.*, **40**, p.51-510, 1992.
- Sher, H., and Zallen, R., *J. Chem. Phys.*, **53**, p.37-59, 1970.
- Smith, J.T. and Vasilos, T., *J. Appl. Phys.*, **35**, p.215, 1964.
- Spriggs, R.M. and Dutta, S.K., *Mat. Sci. Res.*, **6**, p.369, 1973.
- Stoneham, A. and Tasker, P., in "Surface and Near-Surface Chemistry of Oxide Materials", eds. J. Nowotny and Dufour, p.1, 1988.
- Struijts, A.J. in "Ceramic Microstructures", eds. R.M. Fulrath and J.A. Pask, p.76, 1973.
- Takemura, M., Hyakubu, A., Yoshitake, M. Tamura, "Evaluation of Thermal and Mechanical Properties of Functionally Gradient Materials of ZrO<sub>2</sub>-Ni System", *Ceramic Transactions*, **34: Functionally Gradient Materials**, p.271-78, 1993.
- Vasilos, T. and Spriggs, R.M., *J. Am. Ceram. Soc.*, **46**, p.493, 1963.
- Wagner, T., Kirchheim, R., and Ruhle, M., "Electrochemically-Induced Reactions at N:/ZrO<sub>2</sub> Interfaces", *Acta metall. mater.*, **40**, p.585-93, 1992.
- Williams, J. C., "Treatise on Materials Science and Technology", ed. F.F. Wong, Academic Press, NY, p.173-98, 1976.
- Wu, S. "Sintering Additives for Zirconia Ceramics", *Series 1: Research Reports in Materials Science*, p.6-38, 1986.